Materials Today Chemistry 36 (2024) 101928

Contents lists available at ScienceDirect

Materials Today Chemistry

journal homepage: www.journals.elsevier.com/materials-today-chemistry/

# Spinel type $MCo_2O_4$ (M = Mn, Mg, Ni, Cu, Fe and Zn) for chemoresistance gas sensors

Zichen Zheng [a], Kewei Liu [a,b], Yiwen Zhou [a], Zicong Zhang [a], Hongyuan Su [a], Xudong Nie [a], Marc Debliquy [b], Zexin Yu [c], Chao Zhang [a,*]

[a] College of Mechanical Engineering, Yangzhou University, Yangzhou, 225127, PR China
[b] Service de Science des Matériaux, Faculté Polytechnique, Université de Mons, Mons, 7000, Belgium
[c] Institute for Manufacturing Technologies of Ceramic Components and Composites, University of Stuttgart, Stuttgart, 70569, Germany

ARTICLE INFO

*Keywords:*
Gas sensor
Semiconductor metal oxide
Nanostructure
Morphology regulation
Sensing mechanism

ABSTRACT

Gas sensors present significant research value and broad applicability for environmental monitoring, medical diagnosis and agricultural production. As a p-type spinel ternary semiconductor metal oxide (SMOX), $MCo_2O_4$ (M = Mn, Mg, Ni, Cu, Fe and Zn) chemoresistance gas sensors possess a satisfactory sensing performance to diverse hazardous gases. Owning to the superior potential and widespread applications, this work provides a critical review of the current development for $MCo_2O_4$ chemoresistance gas sensors. Basic information of $MCo_2O_4$ and evaluation criteria of corresponding gas sensors were described primarily. Then the synthesis, morphology, characterization and sensing properties of $MCo_2O_4$ gas sensors were elaborated on the basis of different microtopography dimensions under zero dimension (0D), one dimension (1D), two dimension (2D) and three dimension (3D). Various efficient tactics for improving sensing performance and relevant transducing mechanism were demonstrated as well. Finally, perspectives on developing $MCo_2O_4$ synthesis and applications in gas sensors were elaborated.

## 1. Introduction

In modern society, toxic, flammable and explosive gases are serious sources of air pollution all along, which have done great harm to environment, human and other living creatures. Thus, the gas sensor technology which possesses lower detection limits than human respiratory system has been attracted great attention in scientific, agricultural, industrial and medical fields [1–9]. Specifically, gas sensor, which is constitutive of a transducer and an active layer can be generally categorized under chemical detector branch, while the desired experimental data of which can be acquired by converting adequate chemical reaction messages into measurable electronic signals, including variation in resistance, frequency, current or voltage [10,11]. Moreover, the capacity of gas sensors can be assessed by diverse indexes, e.g. sensitivity, limit of detection (LOD), selectivity, repeatability, operating temperature, humidity resistance, recovery and response time [12,13]. In order to optimize gas sensor performance, a series of strategies have been widely used such as heterojunction construction [14], morphological regulation [15], catalyst doping and decorating [16], pH regulation [17] and utilization of metal-organic frameworks (MOF) [18]. Among diverse materials, the ternary semiconductor metal oxide (SMOX), including $CoFe_2O_4$ [19], $ZnSnO_3$ [20], $ZnWO_4$ [21] and $NiFe_2O_4$ [22] provided a strategy to detect different gases in a rapid, economical, convenient and reliable way compared with some large scale equipment such as gas chromatography (GC) and ion mobility spectrometry (IMS), which have been received great attention [23–25]. Due to the prominent sensing properties, SMOX gas sensors have been extensively utilized in health care [26–28], industrial design [29,30], agricultural engineering [31], daily life [32] and so forth [25]. The sensitivity of SMOX gas sensors is desirable, as poor cross-selectivity and high working temperature are still two major problems under practical application scenarios. However, spinel metal oxides which own special chemical component and structure gradually entered into researchers' field of vision. The transition metal or post-transition metal cations hold the two diverse cation sites while the cations with different chemical properties and charge states are arranged between the cations and the ambient lattice oxygen at disparate bonding energies. The combination of abundant transition metals and post-transition metal cations in spinel metal oxides opens up

* Corresponding author. College of Mechanical Engineering Yangzhou University Huayang West Road 196 Yangzhou 225127, Jiangsu Province PR China.
*E-mail address:* zhangc@yzu.edu.cn (C. Zhang).

https://doi.org/10.1016/j.mtchem.2024.101928
Received 20 November 2023; Received in revised form 1 January 2024; Accepted 14 January 2024
Available online 24 January 2024

new opportunities for enhancing many features of sensitivity, selectivity and reproducibility [33,34]. Particularly, $MCo_2O_4$ (M = Mn, Mg, Ni, Cu, Fe and Zn) (The following non-essential are referred to as $MCo_2O_4$ commonly) with molecular formula $AB_2O_4$ of two transition metals is a p-type spinel metal oxides transformed from $Co_3O_4$, where $M^{2+}$ are located in one-eighth of the tetrahedral position while $Co^{3+}$ occupied in a half of the octahedral position of the face-centered cubic oxygen lattice, which possesses the merits of high conductivity, excellent electrochemical properties, robust structural stability and low synthesis cost [35,36], is extensively applied in gas sensor [37], lithium battery [38], electrocatalyst [39] and supercapacitor [40], as shown in Fig. 1a and listed in Table 1. As a result, many researchers have published reviews based on $MCo_2O_4$ materials. Cheng et al. summarized the latest researches of core-shell structured $NiCo_2O_4$ based electrochemical capacitors, and substantiated that 1D $NiCo_2O_4$ prepared by electrospinning could be used as the matrix to construct diverse novel materials to improve the performance of capacitors [41]. Because of the rapid development of supercapacitor devices and batteries, Goncalves et al. reviewed the application of low-budget and vast multi-functional $MnCo_2O_4$ materials [42].

Furthermore, as a typical spinel oxide and p-type semiconductor which owns suitable chemical structure and composition, $MCo_2O_4$ based gas sensors has strong response and excellent selectivity at low operating temperature for massive gases [63,64]. When detecting the same gas, the response value of p-type SMOX gas sensor is equivalent to the square root of which to common n-type SMOX gas sensor under the same testing circumstances, thus the n-type SMOX are preferred as gas sensor materials chiefly [65–67]. However, chemoresistance p-type $MCo_2O_4$ gas sensors with excellent property are still effective in monitoring diverse target gas and applying in many other fields, which has great prospects for fabricating high performance gas sensors which is displayed in Fig. 1b.

Despite there are abundant reviews about diverse SMOX based gas sensors, reviews on the chemoresistance $MCo_2O_4$ gas sensors are still lacking. Therefore, this review demonstrates the status of $MCo_2O_4$ and their expandable materials oriented towards the development of SMOX gas sensors with exquisite gas sensitive mechanism analysis. In detail, we focused on the morphology control of $MCo_2O_4$ microscopic

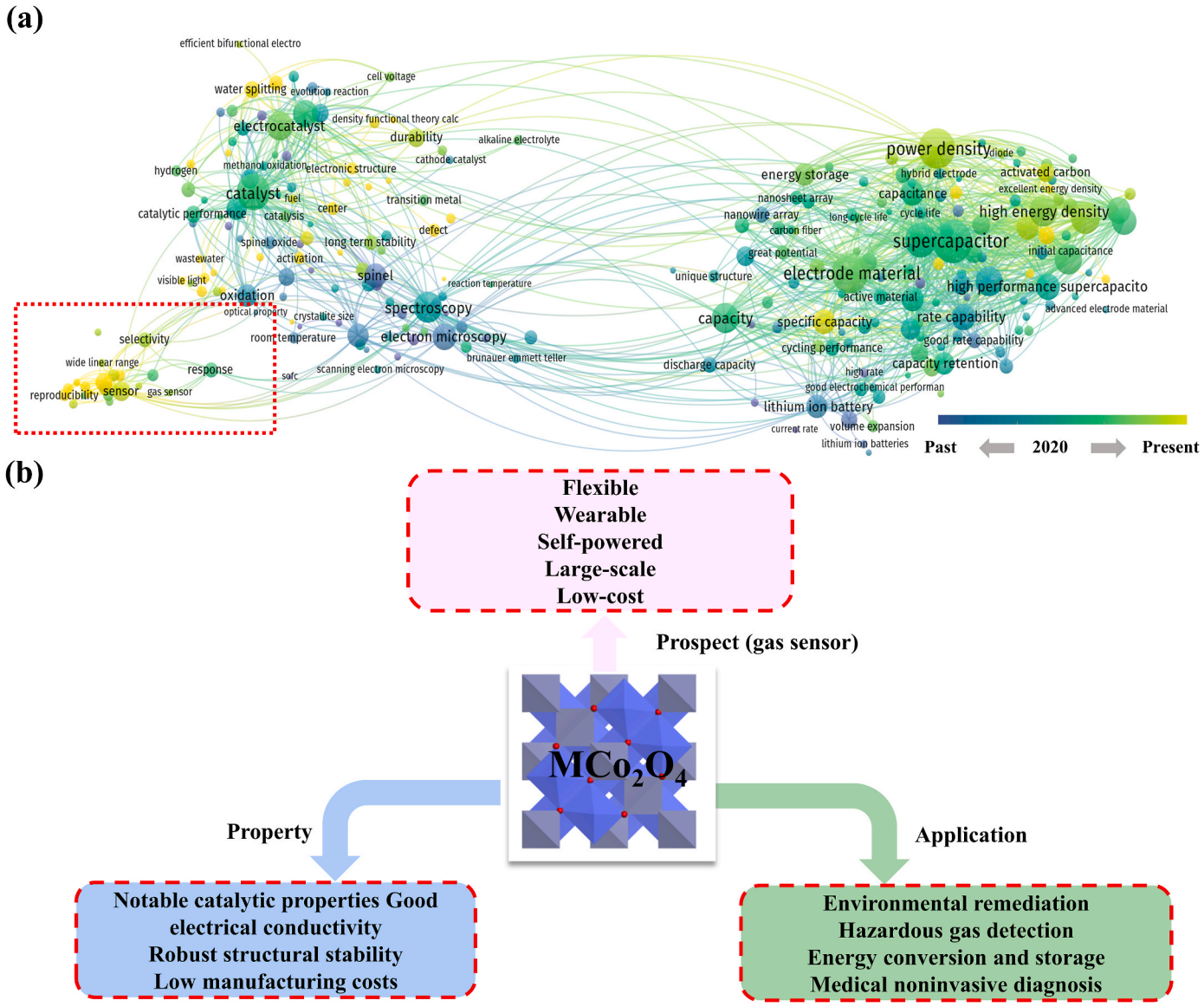


**Fig. 1.** (a) Visualization of current trends in research on $MCo_2O_4$, along with co-occurring keywords. Lines connecting two keywords, size of circle of each keyword, and color of circle indicate the relevance of the keywords, the frequency of keywords appearance, and average publication date, respectively. Data were collected from web of science. (b) The property, application and prospect of gas sensor based on $MCo_2O_4$.

**Table 1**
The application in other fields based on $MCo_2O_4$.

| Dimension | Composites | Microstructures | Growth reagents | Synthesis method | Application | Ref. |
|---|---|---|---|---|---|---|
| 3D | $CeO_2/MnCo_2O_4$ | Microspheres | $MnC_4H_6O_4{\cdot}4H_2O$, $C_4H_6CoO_4{\cdot}4H_2O$, $KMnO_4$, $Ce(NO_3)_3{\cdot}4H_2O$ | Hydrothermal and gas bubble | Chemical looping combustion | [43] |
| 0D | $MgCo_2O_4$ | Nanoparticles | $Co(NO_3)_2{\cdot}6H_2O$, $Mg(NO_3)_2{\cdot}6H_2O$, NaOH | Hydrothermal | Catalytic degradation | [44] |
| 3D | O–$NiCo_2O_4$ | Octahedral nanoblocks | Ethanol, ammonium hydroxide, $Na_2CO_3$, $Co(NO_3)_2{\bullet}6H_2O$, $Ni(NO_3)_2{\bullet}6H_2O$, ethylene glycol, NaOH | Solvothermal | Catalytic degradation | [45] |
| 1D | $NiCo_2O_4$/NC | Nanowires | $Co(NO_3)_2{\bullet}6H_2O$, $Ni(NO_3)_2{\bullet}6H_2O$, DMF, PTA, NaOH, Ni foam | Hydrothermal/In-situ growth | Energy storage and conversion | [46] |
| 1D | $NiCo_2O_4$@CC | Nanowires | $Co(NO_3)_2{\bullet}6H_2O$, $Ni(NO_3)_2{\bullet}6H_2O$, 68 % wt. $HNO_3$, CC | Hydrothermal | Energy storage and catalytic degradation | [47] |
| 3D | $NiCo_2O_4$@$RuO_2$ | Nanocones | $RuCl_3{\cdot}xH_2O$, $CoCl_2{\cdot}6H_2O$, $NiCl_2{\cdot}6H_2O$, HMT, SDS, PSS, ethanol, KOH | Hydrothermal | Overall water splitting. | [48] |
| 1D | In@$NiCo_2O_4$ | Nanoneedles | $Co(NO_3)_2{\bullet}6H_2O$, $Ni(NO_3)_2{\bullet}6H_2O$, $In(NO_3)_3{\cdot}4H_2O$, Carbon fiber | Pulsed laser ablation | Energy storage and conversion | [49] |
| 2D | $Co_3O_4/FeCo_2O_4$ | Hierarchical nanosheets | Foamed nickel, HCl, $NH_4F$, $Co(NO_3)_2{\cdot}6H_2O$, $CON_2H_4$, $Fe(NO_3)_2{\cdot}6H_2O$, $FeCl_2{\cdot}4H_2O$, $CoCl_2{\cdot}6H_2O$ | Hydrothermal | Energy storage and conversion | [50] |
| 2D | $FeCo_2O_4$ | Macaroon-liked structure | Glucose, KOH, $FeSO_4{\cdot}7H_2O$, $Co(NO_3)_2{\cdot}6H_2O$, $NH_4F$, PTFE hexamethylenetetramine, AC powder (YEC-8A) | Solvothermal | Energy storage and catalytic degradation | [51] |
| 3D | Ce@$ZnCo_2O_4$ | Nanospheres | $Zn(NO_3)_2{\cdot}6H_2O$, $Co(NO_3)_2{\cdot}6H_2O$, $Ce(NO_3)_3{\cdot}6H_2O$, glycerol, isopropanol | Solvothermal | Glutathione detection | [52] |
| 2D | $ZnCo_2O_4$ | Sheet-shaped | $Zn(NO_3)_2{\cdot}6H_2O$, $Co(NO_3)_2{\cdot}6H_2O$, isopropanol, ethanol | Solvothermal | Electromagnetic wave absorption | [53] |
| 3D | Ce@$ZnCo_2O_4$ | Core-shell microspheres | $Zn(CH_3COO)_2{\cdot}2H_2O$, $Co(CH_3COO)_2{\cdot}4H_2O$, ethylene Glycol, $Ce(NO_3)_3{\cdot}6H_2O$, hexamethylenetetramine | Reflux | Catalytic propane decomposition | [54] |
| 3D | ZnO/$ZnCo_2O_4$ | Spherical particles | $Zn(CH_3COO)_2{\cdot}2H_2O$, $Co(CH_3COO)_2{\cdot}4H_2O$, glycyrrhiza glabra extract aqueous solution | Hydrothermal | Bisphenol A decomposition | [55] |
| 1D | $ZnCo_2O_4$ | Nanowire arrays | $Zn(NO_3)_2{\cdot}6H_2O$, $Co(NO_3)_2{\cdot}6H_2O$, $CO(NH_2)_2$, nickel foam | Hydrothermal | Non-enzymatic glucose detection | [56] |
| 3D | $ZnCo_2O_4$/C | Micro-hydrangeas | $ZnCl_2$, $Zn(NO_3)_2{\cdot}6H_2O$, $Co(NO_3)_2{\cdot}6H_2O$, PVP, $Na_3C_6H_5O_7$, ethanol, ethylene glycol | Solvothermal | Lithium ions batteries | [57] |
| 3D | $ZnM_xCo_{2-x}O_4$ (M = Mn) | Agglomerated nanoblocks | $Zn(NO_3)_2{\cdot}6H_2O$, $Co(NO_3)_2{\cdot}6H_2O$, $Mn(NO_3)_2{\cdot}4H_2O$ | Sol-gel combustion | $H_2O_2$ determination | [58] |
| 3D | Pt@$ZnCo_2O_4$ | Nanoparticles decorated on the microflowers | $H_2PtCl_6$, $NaBH_4$, PVP, phthalic acid, $Zn(NO_3)_2{\cdot}6H_2O$, $Co(NO_3)_2{\cdot}6H_2O$, acetone, DMF | Hydrothermal | Electrochemical Caffeine detection | [59] |
| 2D | $ZnCo_2O_4$ | Nanoplate arrays | $Zn(NO_3)_2{\cdot}6H_2O$, $Co(NO_3)_2{\cdot}6H_2O$, 2-methylimidazole | Static synthesis | Dihydroxy benzene isomers detection | [60] |
| 3D | $ZnCo_2O_4$ | Spherical shape-liked microparticles | $Zn(NO_3)_2{\cdot}6H_2O$, $Co(NO_3)_2{\cdot}6H_2O$, citric acid, KOH | Sol-gel method | Energy storage and conversion | [61] |
| 3D | ZnO/$ZnCo_2O_4$ | Microflowers | $Zn(NO_3)_2{\cdot}6H_2O$, $Co(NO_3)_2{\cdot}6H_2O$, isopropanol, ethanol, D(+)-Glucose | Hydrothermal/ Solvothermal | Electromagnetic wave absorption | [62] |
| 2D | $ZnCo_2O_4$ | Wrinkled-paper-like nanoflakes | $Zn(NO_3)_2{\cdot}6H_2O$, $Co(NO_3)_2{\cdot}6H_2O$, PVP, HMT | Hydrothermal | Energy storage and conversion | [38] |

Abbreviation: O–$NiCo_2O_4$: Octahedral $NiCo_2O_4$; NC: Porous Ni/C substrate; CC: carbon cloth; SDS: sodium dodecyl sulfate; PSS: polystyrene sulfonic acid sodium salt; Triblock copolymer pluronic F127: $(HO(CH_2CH_2O)_{106}(CH_2CH(CH_3)O)_{70}(CH_2CH_2O)_{106}H)$; PTFE: polytetrafluoroethylene; PrGO: porous reduced graphene oxide; PTA: Terephthalic acid; NC-CNT: nitrogen-rich carbon nanotube; PVP: polyvinyl pyrrolidone; DMF: N,N-Dimethylformamide; HMT: hexamethylene-tetramine.

materials, reviewed the performance of related gas sensors and summarized the related preparation process, gas-sensitive enhancement mechanism and important parameters of gas sensors based on the literature of the last five years as shown in Scheme 1. Furthermore, the test system and sensing parameters of gas sensors are introduced in section 2. Different synthesis strategies were used to fabricate $MCo_2O_4$ with various morphologies in diverse dimensions (0D, 1D, 2D, and 3D), which is summarized in Tables 2 and 3. Diverse effective tactics have been adopted to strengthen sensing performance and the concrete sensing results is displayed in Table 4. This is expected to set up a framework of $MCo_2O_4$ spinel oxide gas sensors and emphasize the significance of morphology control in novel material synthesis, further improving the logic and rationality of resistive gas sensor design.

## 2. Test system and basic gas sensing performance parameters

### 2.1. Test system

Generally, $MCo_2O_4$ based SMOX gas sensor system belongs to static system, comprising the valve system, flow control device, gas sensors and chamber, power supply and signal processing system [96,144]. In a typical testing process, the synthetic sample with an appropriate amount of deionized water will be ground evenly in a grinding bowl. Then the as-prepared slurry is uniformly applied to the sensor substrate. The corresponding sensor is obtained by aging under the specific condition. Next, the sensor will be installed in a test chamber in preparation for test. Under specific operating conditions, high-purity air is introduced to obtain a steady resistance value and the tested gas is injected for gas sensing test to obtain experimental data. After the resistance value has stabilized, high purity air is introduced again to restore the resistance value to its initial state. Above all, the entire testing circumstance is an uncontaminated chamber with consistent relative humidity (RH) and operating temperature while the raw sensing data can be acquired and the crucial sensing parameters can be evaluated. In addition, the sensor can be designed as a ceramic on-tube structure or be fabricated on an aluminum oxide substrate.

### 2.2. Basic gas sensing performance parameters

In most instances, optimum working temperature, gas response, response and recovery time, selectivity, LOD, long-term stability, reproducibility and moisture resistance properties can be applied to evaluate sensing performance of $MCo_2O_4$ based gas sensors [143,145].

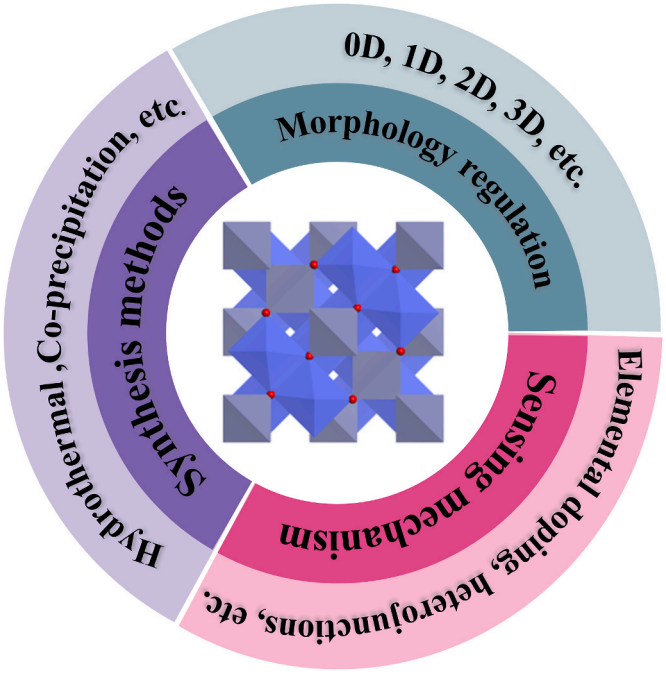


**Scheme 1.** Diagram of the synthesis strategies and sensing mechanism of $MCo_2O_4$ sensors.

**Table 2**
Summary of the design and synthesis approaches.

| Synthesis approaches | Advantages | Disadvantages | Ref. |
|---|---|---|---|
| Hydrothermal and solvothermal methods | Facile preparation, broad resource of raw materials, high crystallinity of the samples, excellent morphology control | High temperature and high pressure, high equipment requirements, long reaction time | [68–70] |
| Co-precipitation | Low energy consumption, low temperature of synthesis, control over particle composition, facile and rapid synthesis process, uniform chemical composition, easy access to small particle size products | Reproducibility issues, difference in precipitation rate for certain reactants, precipitation of impurities | [71–73] |
| Self-sacrificing template | Excellent and precise morphology and size control, obtained products without agglomeration | High cost, relatively complex synthesis process, difficult to prepare products at large scale | [74–76] |

### 2.2.1. Optimum operating temperature

Operating temperature served as a significant role in sensing mechanism whereas it controls chemical interactions between target gas molecules and the $MCo_2O_4$ junction [146]. As high working temperature leads to excessive energy consumption, hindering the development of flexible semiconductor gas sensor, sensor miniaturization and IC integration, lowering the long-term stability and safety feature, room temperature or subzero temperature operated gas sensors are the focus of massive researchers [147,148].

### 2.2.2. Gas response

Gas response, also known as sensitivity, is the ratio of gas sensor signal output to target gas concentration, reflecting the intensity of the physical and chemical reaction between the target gas molecules and sensing material, which can be illustrated by several patterns as discussed below [149,150].

In detail, the resistance value of SMOX sensor reaches steady state in the target gas and in high purity air circumstances can be abbreviated as Rg and Ra respectively. Thus, the response is defined as Ra/Rg under oxidized gas detection circumstances and Rg/Ra can be used to calculated for reducing gas detection circumstances. Furthermore, the response is also demonstrated as the rate of resistance variation during sensing process which can be defined as $\triangle R/Ra$. The superior sensing performance is usually accompanied by a high response value [151].

### 2.2.3. Response and recovery time

Response time is when electrode resistance changed 90 % during target gas adsorption possess while the recovery time represents which changed 90 % during target gas desorption possess, through which the adsorption and desorption rate of target gas molecules onto the surface of sensing material could be reflected [152,153].

### 2.2.4. Selectivity

The selectivity demonstrates the ability of sensors to resist the influence of interfered gas while the strong sensitivity to target gas and obviously weak sensitivity to other interfered gas (including water molecules) are what we pursue. Based on the working principle of chemically resistive SMOX gas sensor, cross-selectivity is inevitable. Thus, electronic nose based on SMOX gas sensors combined with pattern recognition algorithm and Eley-Rideal model on account of kinetic parameters during gas sensing can effectively improve the selectivity under the situation of multi-gas detection [31,154,155].

### 2.2.5. Limit of detection

LOD refers to lowest detectable concentration of the target gas which can be monitored in the background signal that is three times to noise. The optimization of the lower detection limit is highly essential in some special areas such as microenvironmental monitoring and medical diagnosis. The minimum detection limit is expressly crucial to expand application of gas sensors while the ppb and ppt level gas sensors are still lacking [156].

### 2.2.6. Stability

The stability of gas sensor can be divided into two parts: reproductivity and long-term stability. In specific, the excellent reproductivity of sensor represents small fluctuations in response of several common dynamic response-recovery cycles. The long-term stability is an index for evaluating sensor sensitivity fluctuation for a relative long period of $\geq$15 days. Stability affects the reliability of gas sensing data and the service life of sensor, which plays a decisive role in the practical application [157].

### 2.2.7. Moisture resistance

In general, water molecules in the environment are similar to other gas molecules which will adsorb on the sensing material and undergo physical and chemical reactions with oxygen species, leading to changes of reference resistance and gas response [158]. In particular, water molecules will contest adsorption site with target gas molecules and thus reducing sensitivity in most instances in the process of gas sensing. Therefore, excellent moisture resistance is the main performance of high-quality SMOX gas sensors at present.

### 2.2.8. Gas flow rate

Imprecise gas flow regulation will greatly affect the response value of the gas sensor. On the one hand, in the process of gas dynamic detection, the relationship between sensitivity and target gas concentration can be revealed through statistical analysis to eliminate the impact of gas flow error on detection results [159]. On the other hand, by constructing a more stable gas sensitive matrix and sensing film, the influence of large

**Table 3**
$MCo_2O_4$ microstructures: morphologies, methods of preparation and other growth parameters.

| Dimension | Composites | Microstructures | Growth reagents | Synthesis method | Anneal temperature (°C) | Anneal time | Ref. |
|---|---|---|---|---|---|---|---|
| 0D | $MnCo_2O_4$/Polypyrrole | Nanoparticles | $Mn(NO_3)_2{\cdot}4H_2O$, $CoCl_2{\cdot}6H_2O$, NaOH, DMF | In situ chemical polymerization | 500 °C | 6 h | [77] |
| | $MnCo_2O_4$ | Spherical shape nanoparticles | $Mn(NO_3)_2{\cdot}4H_2O$, $Co(NO_3)_2{\cdot}6H_2O$, ammonium hydroxide, urea | Hydrothermal | – | – | [78] |
| | $MgCo_2O_4$ | Nanoparticles | $Co(NO_3)_2{\cdot}6H_2O$, $Mg(NO_3)_2{\cdot}6H_2O$, AOT, ethylene glycol | Microwave-assisted colloidal | 400, 500, 600, 700, 800 °C | 5 h | [79] |
| | $MoS_2/NiCo_2O_4$ | Nanoparticles | $Ni(NO_3)_2{\cdot}6H_2O$, $Co(NO_3)_2{\cdot}6H_2O$, $MoS_2$, NaOH | Hydrothermal | – | – | [37] |
| | $Ni_xCo_{3-x}O_4$ | Nanoparticles | Co(II) and Ni(II) oxalates, ammonium oxalate, $H_2C_2O_4$ | Co-precipitation/ Thermal decomposition | 300 °C | 24 h | [80] |
| | g-$C_3N_4/NiCo_2O_4$ | Spherical nanoparticles | Melamine, $Ni(NO_3)_2{\cdot}6H_2O$, $Co(NO_3)_2{\cdot}6H_2O$, NaOH | Hydrothermal | – | – | [81] |
| | $In_2O_3$/YSZ/$NiCo_2O_4$ | Nanoparticles | $In(NO_3)_3$, glycine, $NiCo_2O_4$, ethyl cellulose, ethanol, α-terpineol | Self-propagating high-temperature | 900 °C | 3 h | [82] |
| | $NiCo_2O_4$ | Nanoparticles | $Ni(NO_3)_2{\cdot}6H_2O$, $Co(NO_3)_2{\cdot}6H_2O$, urea, ammonium hydroxide | Hydrothermal | – | – | [83] |
| | $FeCo_2O_4$/graphene | Nanoparticles | $Co(NO_3)_2{\cdot}6H_2O$, $Fe(NO_3)_2{\cdot}6H_2O$, urea, NaOH | Hydrothermal | – | – | [84] |
| | $WO_3/FeCo_2O_4$ | Nanoparticles | $Na_2WO_4{\cdot}2H_2O$, NaCl, HCl, $FeSO_4{\cdot}7H_2O$, $Co(NO_3)_2{\cdot}6H_2O$, carbamide, ethylene glycol | Hydrothermal | 350 °C | 2 h | [85] |
| | $ZnO/ZnCo_2O_4$ | Nanodots | $Zn(NO_3)_2{\cdot}6H_2O$, $Co(NO_3)_2{\cdot}6H_2O$, NaCl, ZnO | Hydrothermal/Co-precipitation | 600 °C | 2 h | [86] |
| | $ZnO/ZnCo_2O_4$ | Nanoparticles | $Zn(NO_3)_2{\cdot}6H_2O$, $Co(NO_3)_2{\cdot}6H_2O$, PVP, DMF | Hydrothermal | 450 °C | 3 h | [87] |
| | $ZnCo_2O_4$ | Nanoparticles | $Zn(NO_3)_2{\cdot}6H_2O$, $Co(NO_3)_2{\cdot}6H_2O$, $K_2CO_3$ | Co-precipitation/ digestion | 600 °C | 5 h | [88] |
| | $ZnCo_2O_4$/Polypyrrole | Nanoparticles | $Zn(NO_3)_2{\cdot}H_2O$,$CoCl_2{\cdot}6H_2O$, NaOH, DMF | In situ chemical polymerization | 100 °C | 5 h | [77] |
| 1D | $Co_3O_4/NiCo_2O_4$/CC | Nanowires | CC, HCl, acetone, CTAB, $Ni(NO_3)_2{\cdot}6H_2O$, $Co(NO_3)_2{\cdot}6H_2O$, urea, 2-methylimidazole | Hydrothermal | 350 °C | 2 h | [89] |
| | $NiCo_2O_4$/rGO | Nanowires | $Ni(NO_3)_2{\cdot}6H_2O$, $Co(NO_3)_2{\cdot}6H_2O$, urea, ethanol, GO | Hydrothermal | 300 °C | 2 h | [90] |
| | $Pd/NiCo_2O_4$ | Nanoneedles | $Ni(NO_3)_2{\cdot}6H_2O$, $Co(NO_3)_2{\cdot}6H_2O$, urea, Pd thin film | Thin film deposition/ Hydrothermal | 350 °C | 2 h | [91] |
| | $NiCo_2O_4$/rGO | Nanorods | $CoCl_2{\cdot}6H_2O$, $NiCl_2{\cdot}6H_2O$, CTAB | Hydrothermal | 350 °C | 3 h | [92] |
| | $NiCo_2O_4$ | Nanorods | $CoCl_2{\cdot}6H_2O$, $NiCl_2{\cdot}6H_2O$, ammonium fluoride, urea | Hydrothermal | 600 °C | 5 h | [93] |
| | $NiCo_2O_4$ | Hierarchical hollow microtubules | $Na_2WO_4{\cdot}H_2O$, $AgNO_3$, $Ni(NO_3)_2{\cdot}6H_2O$, $Co(NO_3)_2{\cdot}6H_2O$, PVP, urea, $HNO_3$, ammonium hydroxide | Template-assisted process/Etching treatment | 300 °C | 2 h | [94] |
| | $NiCo_2O_4/SnO_2$ | Nanofiber | $Ni(NO_3)_2{\cdot}6H_2O$, $Co(NO_3)_2{\cdot}6H_2O$, ethanol, DMF, PVP, $SnCl_2{\cdot}2H_2O$, NaOH | Electrospinning/ Hydrothermal | 400 °C | 3 h | [95] |
| | $Zn@NiCo_2O_4$ | Mesoporous rods | $Ni(SO_4)_2{\cdot}7H_2O$, $Zn(SO_4)_2{\cdot}7H_2O$, $CoSO_4{\cdot}7H_2O$, oxalic acid, ethylene glycol | Hydrothermal | 450 °C | 2 h | [96] |
| | $CuO/CuCo_2O_4$ | Nanotubes | $Co(NO_3)_2{\cdot}6H_2O$, $CuCl_2{\cdot}2H_2O$, PVP, DMF, ethanol | Electrospinning | 350 °C | 3 h | [97] |
| | $TiO_2/ZnCo_2O_4$ | Porous nanorods | $Zn(NO_3)_2{\cdot}6H_2O$, $Co(NO_3)_2{\cdot}6H_2O$, ammonium acid carbonate, Titanium (IV) oxyacety lacetonate | Dual-oxalate sacrificial template | 500 °C | 2 h | [98] |
| | $ZnCo_2O_4$ | Porous nanorods<br>Single-layer nanochain | $Zn(NO_3)_2{\cdot}6H_2O$, $Co(CH_3COO)_2{\cdot}4H_2O$, ethanol, oxalic acid | Co-precipitation | 350 °C<br>500 °C | 2 h<br>2 h | [99] |
| | $ZnCo_2O_4$ | Microtubes | $Zn(NO_3)_2{\cdot}6H_2O$, $Co(NO_3)_2{\cdot}6H_2O$, absorbent cotton | Biomorphic template | 500, 600, 700 °C | 2 h | [100] |
| | $ZnO/ZnCo_2O_4$ | Nanotubes | $Zn(NO_3)_2{\cdot}6H_2O$, $Co(NO_3)_2{\cdot}6H_2O$, DMF, ethanol, PVP | Capillary electrospinning | 450 °C | 100 min | [101] |
| | $ZnO/ZnCo_2O_4$ | Tube in tube nanostructure | $Zn(NO_3)_2{\cdot}6H_2O$, $Co(NO_3)_2{\cdot}6H_2O$, DMF, ethanol, PVP | Capillary electrospinning | 450 °C | 100 min | [102] |
| | $Zn_xCo_{2-x}O_4$ | Nanorods | $Zn(NO_3)_2{\cdot}6H_2O$, $Co(NO_3)_2{\cdot}6H_2O$, $K_2CO_3$ | Co-precipitation | 500 °C | 2 h | [103] |
| 2D | $MgCo_2O_4$ | Nanosheets | $Co(NO_3)_2{\cdot}6H_2O$, $Mg(NO_3)_2{\cdot}6H_2O$, urea, $NH_4OH$ | Hydrothermal | – | – | [104] |
| | $NiCo_2O_4/WO_3$ | Nanosheets | $Na_2WO_4{\cdot}2H_2O$, HCl, NaCl, Ni $(NO_3)_2{\cdot}6H_2O$, $Co(NO_3)_2{\cdot}6H_2O$, urea | Hydrothermal/Co-precipitation | 350 °C | 2 h | [105] |
| | $ZnO/NiCo_2O_4$ | Nanosheets with nanofibers | $Zn(NO_3)_2{\cdot}6H_2O$, $Na_2CO_3$, SDSN, Ni $(NO_3)_2{\cdot}6H_2O$, $Co(NO_3)_2{\cdot}6H_2O$, urea | Hydrothermal | 350 °C | 2 h | [106] |
| | $NiCo_2O_4$/MWCNTs | Nanoflakes | $Ni(NO_3)_2{\cdot}6H_2O$, $Co(NO_3)_2{\cdot}6H_2O$, MWCNTs, $HNO_3$ | Hydrothermal | 450 °C | 3 h | [107] |
| | $NiCo_2O_4$ | Nanoflakes | $Ni(NO_3)_2{\cdot}6H_2O$, $Co(NO_3)_2{\cdot}6H_2O$, ammonium hydroxide | Co-precipitation | 450 °C | 4 h | [108] |

(*continued on next page*)

**Table 3** (*continued*)

| Dimension | Composites | Microstructures | Growth reagents | Synthesis method | Anneal temperature (°C) | Anneal time | Ref. |
|---|---|---|---|---|---|---|---|
| | $NiCo_2O_4$ | Nanoplates | Poly ethylene glycol-6000, Ni$(NO_3)_2{\cdot}6H_2O$, Co$(NO_3)_2{\cdot}6H_2O$ | Hydrothermal | 300, 500, 700 °C | 3 h | [109] |
| | $NiCo_2O_4$/α-$MoO_3$ | Porous nanosheets | Mo powder, $H_2O_2$, Ni$(NO_3)_2{\cdot}6H_2O$, Co$(NO_3)_2{\cdot}6H_2O$, urea | Hydrothermal/Co-precipitation | 350 °C | 2 h | [110] |
| | $NiCo_2O_4$ | Nanosheets | Ni$(NO_3)_2{\cdot}6H_2O$, Co$(NO_3)_2{\cdot}6H_2O$, Sodium dodecyl sulfate, NaOH | Hydrothermal | – | – | [111] |
| | $NiCo_2O_4$/rGO | Nanoplates | $CoCl_2{\cdot}6H_2O$, $NiCl_2{\cdot}6H_2O$, CTAB | Hydrothermal | 400 °C | 2 h | [112] |
| | $CuCo_2O_4$ | Nanosheets | Cu$(NO_3)_2{\cdot}3H_2O$, Co$(NO_3)_2{\cdot}6H_2O$, citric acid | Solution combustion method | – | – | [113] |
| | $CuCo_2O_4$ | Nanoplatelets | Cu$(NO_3)_2{\cdot}3H_2O$, Co$(NO_3)_2{\cdot}6H_2O$, urea | Hydrothermal | 350 °C | 2 h | [114] |
| | $MoS_2$–$ZnCo_2O_4$–$ZnCo_2O_4$/CC | Nanosheets | Zn$(NO_3)_2{\cdot}6H_2O$, Co$(NO_3)_2{\cdot}6H_2O$, CO$(NH_2)_2$, $(NH_4)F$, $Na_2MoO_4{\cdot}6H_2O$, $CH_4N_2S$ | Hydrothermal | 200 °C | 5 h | [115] |
| | $ZnCo_2O_4$ | Porous nanosheets | Graphene sheets, ethanol, ammonia solution, Co$(CH_3COO)_2{\cdot}4H_2O$, Zn$(CH_3COO)_2{\cdot}2H_2O$ | Hydrothermal | 450 °C | 3 h | [116] |
| | $ZnCo_2O_4$ | Nanosheet arrays | Zn$(NO_3)_2{\cdot}6H_2O$, Co$(NO_3)_2{\cdot}6H_2O$, CO$(NH_2)_2$, $(NH_4)F$ | Hydrothermal | 400 °C | 2 h | [117] |
| 3D | $Co_3O_4$/$NiCo_2O_4$ | Nanocages | Ni$(NO_3)_2{\cdot}6H_2O$, Co$(NO_3)_2{\cdot}6H_2O$, 2-Methylimidazole, methanol | Hydrothermal/Co-precipitation | 550 °C | 2 h | [118] |
| | NiO/$NiCo_2O_4$ | Hierarchical microspheres | $CoCl_2{\cdot}6H_2O$, $NiCl_2{\cdot}6H_2O$, ethanol | Hydrothermal | 500 °C | 3 h | [119] |
| | $NiCo_2O_4$ | Nanospheres | $CoCl_2{\cdot}6H_2O$, $NiCl_2{\cdot}6H_2O$, urea | Hydrothermal | 350 °C | 2 h | [120] |
| | PdO–NiO/$NiCo_2O_4$ | Truncated Nanocages | Ni$(NO_3)_2{\cdot}6H_2O$, $Na_3C_6H_5O_7{\cdot}2H_2O$, $K_3[Co(CN)_6]$, $PdCl_2$, methanol, ammonia solution | Co-precipitation/etching/wet impregnation | 350 °C | 2 h | [121] |
| | NiO/$NiCo_2O_4$ | Hollow microspheres | Ni$(NO_3)_2{\cdot}6H_2O$, Co$(NO_3)_2{\cdot}6H_2O$, $H_3BTC$, PVP, DMF | Self-sacrificing template | 450 °C | 2 h | [76] |
| | $Co_3O_4$/$NiCo_2O_4$ | Nanocages | Ni$(NO_3)_2{\cdot}6H_2O$, Co$(NO_3)_2{\cdot}6H_2O$, 2-Methylimidazole, methanol | Co-precipitation | 450 °C | 2 h | [122] |
| | $NiCo_2O_4$/$WO_3$ | Nanoflowers | $CoCl_2{\cdot}6H_2O$, $NiCl_2{\cdot}6H_2O$, HCl, $Na_2WO_4{\cdot}2H_2O$ | Hydrothermal | 350 °C | 2 h | [123] |
| | $NiCo_2O_4$ | Hollow microspheres | $CoCl_2{\cdot}6H_2O$, $NiCl_2{\cdot}6H_2O$, urea | Hydrothermal | 300, 400, 500 °C | 3 h | [124] |
| | $NiCo_2O_4$ | Hierarchical microflowers | Ni$(NO_3)_2{\cdot}6H_2O$, Co$(NO_3)_2{\cdot}6H_2O$, 2-Methylimidazole, ethanol | Hydrothermal | 400 °C | 2 h | [125] |
| | $NiCo_2O_4$ | Double-shelled hollow spheres | Ni$(NO_3)_2{\cdot}6H_2O$, Co$(NO_3)_2{\cdot}6H_2O$, xylose, isopropanol | Self-template | 450 °C | 2 h | [126] |
| | PANI/$NiCo_2O_4$ | Nanospheres | Polyimide film, Co$(CH_3COO)_2{\cdot}6H_2O$, gelatin granules, Ni$(CH_3COO)_2{\cdot}4H_2O$), $NH_4HCO_3$, ethylene glycol, ammonium persulphate, aniline, HCl | Hydrothermal | 350 °C | 3 h | [127] |
| | $Cu_{0.3}Co_{2.7}O_4$ | Hollow microspheres | Co$(CH_3COO)_2{\cdot}6H_2O$, $CuSO_4{\cdot}5H_2O$, $NH_3{\cdot}H_2O$, n-propanol | Hydrothermal | – | – | [128] |
| | ZnO/$ZnCo_2O_4$ | Hexahedral-structure | Zn$(NO_3)_2{\cdot}6H_2O$, Co$(NO_3)_2{\cdot}6H_2O$, PVP; K30 | Hydrothermal | 600 °C | 4 h | [129] |
| | $ZnCo_2O_4$ | Hierarchical porous architectures | Co$(CH_3COO)_2{\cdot}4H_2O$, Zn$(CH_3COO)_2{\cdot}2H_2O$, $CO(NH_2)_2$, ethanol | Hydrothermal | 300 °C | 10 min | [130] |
| | $Co_3O_4$/$ZnCo_2O_4$ | Hollow nanostructures | 2-methylimidazole, methanol, Co$(NO_3)_2{\cdot}6H_2O$, ethanol, Zn$(NO_3)_2{\cdot}6H_2O$ | Self-sacrificing template | 450 °C | 2 h | [131] |
| | Ag–$ZnCo_2O_4$ | Hollow microspheres | Zn$(CH_3COO)_2{\cdot}2H_2O$, Co$(CH_3COO)_2{\cdot}4H_2O$, $AgNO_3$, NaOH, polyethylene glycol 1000, ethanol | Solvent-thermal | 500 °C | 3 h | [132] |
| | $ZnCo_2O_4$ | Hierarchical microflowers | 2-methylimidazole, methanol, Co$(NO_3)_2{\cdot}6H_2O$, Zn$(NO_3)_2{\cdot}6H_2O$ | Solvothermal | 405 °C | 55 min | [133] |
| | $ZnCo_2O_4$ | Yolk-shell spheres | Zn$(NO_3)_2{\cdot}6H_2O$, Co$(NO_3)_2{\cdot}6H_2O$, D-Glucose, DMF, $CO(NH_2)_2$, PVP | Hydrothermal | 450 °C | 2 h | [134] |
| | Ag@$ZnCo_2O_4$ | Hollow spheres | 2-methylimidazole, methanol, Co$(NO_3)_2{\cdot}6H_2O$, ethanol, Zn$(NO_3)_2{\cdot}6H_2O$, glucose, $NaBH_4$, $AgNO_3$ | Self-sacrificing template | 400 °C | 1 h | [135] |
| | $ZnCo_2O_4$ | Yolk-shell microspheres | Zn$(CH_3COO)_2{\cdot}2H_2O$, Co$(CH_3COO)_2{\cdot}4H_2O$, ethylene glycol | Co-precipitation | 350 °C | 5 h | [136] |
| | ZnO/$ZnCo_2O_4$ | Hierarchical structure | $NH_4HCO_3$, Zn$(CH_3COO)_2{\cdot}2H_2O$, Co$(CH_3COO)_2{\cdot}4H_2O$ | Hydrothermal | 500 °C | 2 h | [137] |
| | Pd–ZnO/$ZnCo_2O_4$ | Hollow spheres | $K_2PdCl_4$, Zn$(NO_3)_2{\cdot}6H_2O$, Co$(NO_3)_2{\cdot}6H_2O$, methanol, ethanol, 2-methylimidazole, PS latex microspheres (1 μm) | MOF templated synthesis | 450 °C | 1 h | [138] |
| | PdO–ZnO/$ZnCo_2O_4$ | Microspheres | $K_3[Co(CN)_6]$, Zn$(NO_3)_2{\cdot}6H_2O$, HCl, PVP, $PdCl_2$, ethanol | Co-precipitation | 700 °C | 2 h | [139] |
| | $ZnCo_2O_4$ | Hollow polyhedral superstructure | 2-methylimidazole, methanol, Co$(NO_3)_2{\cdot}6H_2O$, Zn$(NO_3)_2{\cdot}6H_2O$, ethanol | Co-precipitation | 500 °C | 2 h | [140] |
| | $ZnCo_2O_4$ | Multishelled Hollow Twin Spheres | Co$(NO_3)_2{\cdot}6H_2O$, Zn$(NO_3)_2{\cdot}6H_2O$, xylose | Solvothermal | 450 °C | 7 h | [36] |

(*continued on next page*)

**Table 3** (*continued*)

| Dimension | Composites | Microstructures | Growth reagents | Synthesis method | Anneal temperature (°C) | Anneal time | Ref. |
|---|---|---|---|---|---|---|---|
| | $ZnO/ZnCo_2O_4$ | Hierarchical macroporous honeycomb-like | $Co(NO_3)_2{\cdot}6H_2O$, $Zn(NO_3)_2{\cdot}6H_2O$, glycerol, 2-propanol, ethanol | Self-template | 350 °C | 2 h | [141] |
| | $Zn_xCo_{3-x}O_4$ | Nanocages | 2-methylimidazole, $Co(NO_3)_2{\cdot}6H_2O$, CTAB, $Zn(NO_3)_2{\cdot}6H_2O$ | Co-precipitation | 350 °C | 2 h | [142] |
| | $ZnCo_2O_4$ | Cabbage-shaped | $Co(NO_3)_2{\cdot}6H_2O$, $Zn(NO_3)_2{\cdot}6H_2O$, *m*-phthalic acid, acetone, DMF | Co-precipitation | 500 °C | 10 min | [143] |

Abbreviation: AOT: Dioctyl sulfosuccinate sodium salt; YSZ: Yttria stabilized zirconia; rGO: Reduced graphene oxide; GO: Graphene oxide; CTAB: Cetyl trimethyl ammonium bromide; MWCNTs: multi-walled carbon nanotubes; CC: Carbon cloth.

or small gas flow rate on the response value can be eliminated from the root.

## 3. $MCo_2O_4$ based gas sensors: synthesis, growth, structure and characterization

In an upcoming section, we summarized the common synthesis strategies and controllable methods to fulfill featured morphologies on the basis of dimensionality of $MCo_2O_4$ gas sensors in Tables 2 and 3. Yet, for further enhance the sensing properties of $MCo_2O_4$ for practical applications, studies on sensing materials with unique morphologies and microstructures are still in progress.

### 3.1. Synthesis of $MCo_2O_4$ semiconductor metal oxides

At present, there are many methods for the synthesis of $MCo_2O_4$ SMOX, which can be divided into two categories: gas phase method and liquid phase method on the basis of the preparation system, of which the latter accounts for a larger proportion. In addition, liquid phase methods can be divided into hydrothermal/solvothermal method, co-precipitation method and self-sacrificing template method.

#### 3.1.1. Hydrothermal and solvothermal methods

Hydrothermal and solvothermal methods are typical wet chemistry methods which mainly study the chemical behavior and law of substances in solution under relatively high pressure and high temperature [160]. By means of simply changing the hydrothermal/solvothermal reaction parameters, such as temperature, concentration, pH value, solvent and surfactant, the degree of crystallization, size, morphology and substance equality of the product can be controlled [161,162]. Collectively, our previous summary had shown that the primary wet chemical methods used to prepare $MCo_2O_4$ are hydrothermal and solvothermal methods.

#### 3.1.2. Co-precipitation

Co-precipitation method can be adopted to prepare solid products by means of the action of precipitating agent and more than two kinds of metal salt solution in the form of hydroxide, carbonate, citrate or oxalate. The final powder is obtained after a heat treatment of calcination if required [71].

#### 3.1.3. Self-sacrificing template

Sacrificial template method is a method to convert template materials into corresponding compounds through displacement reaction or redox reaction by using the vacancy formation principle of mutual diffusion [74,75], which provides a practical method to prepare hollow $MCo_2O_4$ materials.

### 3.2. Morphology regulation for $MCo_2O_4$ preparation

In this section, we will discuss the enhancement for detecting specific gases concentrating on the morphology regulation of $MCo_2O_4$ materials in different dimensions (0D, 1D, 2D and 3D). In particular, X dimensional material can be defined as 3-X dimensional scales of which in space was at nanoscale, for example, one dimensional material is identify with that there are two dimensions in space at nanoscale, such as nanofibers and nanowires.

#### 3.2.1. 0-dimensional (0D) $MCo_2O_4$

Currently, most of the researches of 0D $MCo_2O_4$ gas sensors are focus on nanoparticles. Tiny nanoparticles usually possess large surface area, which is more beneficial for adsorbing abundant oxygen molecules and frequently contacting with the target gas. However, small nanoparticles are more likely to form giant and dense second-ordered particles as the van der Waals' force is inversely proportion to the size of particles. Therefore, the macro-aggregates will prevent target gas from diffusing to the entire material surface, which will decrease the gas response [163]. Furthermore, undersized nanoparticles will bring out the severe aggregation and sintering at high operating temperatures (250–450 °C) in solid-state gas devices [164], leading to the aging of sensors. Nevertheless, some typical 0D $MCo_2O_4$ nanomaterials are successfully applied for gas detection. In general, hydrothermal method is the most frequently-used way to obtain the corresponding nanoparticles. For distance, 0D $ZnO/ZnCo_2O_4$ and pure $ZnCo_2O_4$ nanoparticles synthesized via a facile hydrothermal way was performed by Liu et al. as shown in Fig. 2a and b. The sensitivity of $ZnO/ZnCo_2O_4$ sensor (15.6) is around four times than that of pure $ZnCo_2O_4$ gas sensor (3.7) in 100 ppm ethylene glycol vapor (Fig. 2c–e) while the better anti-interference property of $ZnO/ZnCo_2O_4$ sensor was achieved as shown in Fig. 2f. The high chemisorbed oxygen content (55 %) on the surface and formation of p-n heterojunction are two primary avails for ethylene glycol sensing [87]. Spherical shaped $MnCo_2O_4$ nanoparticles which possessed a mean grain size of 35–55 nm with large BET surface area (65.3 $m^2{\cdot}g^{-1}$) was obtained via urea-assited hydrothermal method without post-calcination process by Vadivel's group and the as-preapred $MnCo_2O_4$ gas sensor exhibited superior sensing performance towards ethanol and acetone [78]. Akhtar et al. employed one-step hydrothermal method for synthesizing the $NiCo_2O_4/MoS_2$ nanocomposites. Using sodium hydroxide as acid-base regulator, the round and biscuit-shaped $NiCo_2O_4$ nanoparticles with a size of around 270–280 nm were modified onto the $MoS_2$ lamellar structure [37]. Meanwhile, Balaji and co-workers reported that the extremely small size $NiCo_2O_4$ particles were fabricated via hydrothermal and post-annealing possess. The uniform spherical nanoparticles increased the number of chemisorbed oxygen molecules while adequate BET surface area and rich oxygen vacanies enhanced the sensitivty synergistically [83]. Akhtar et al. applied hydrothermal method to decorate g-$C_3N_4$ on $NiCo_2O_4$ spherical nanoparticles for ethanol sensing. In this report, the enhanced sensing response (19.2 @ 100 ppm) and extremely low experimental LOD (10 ppb) are derived from enlarged BET surface area and incremental oxygen species absorbed onto the $NiCo_2O_4$/g-$C_3N_4$ surface [81]. As an appropriate substrate for different structured-composites, g-$C_3N_4$ occupies a homogeneous nitrogen group of the structure, which supplyies more coordination sites and increases the quantity of adsorbed

**Table 4**
Sensing performances of gas sensors based on $MCo_2O_4$.

| Dimension | Composites | Microstructures | Synthesis method | Target gas | Concentration (ppm) | T (°C) | Response | Response/ Recovery time | LOD | Ref. |
|---|---|---|---|---|---|---|---|---|---|---|
| 0D | $MnCo_2O_4$/Polypyrrole | Nanoparticles | In situ chemical polymerization | Acetone | 2.5 | RT | [b]1.06 | 47/100 s | – | [77] |
| | $MnCo_2O_4$ | Spherical shape nanoparticles | Hydrothermal | Ethanol | 500 | RT | [e]55 | 65/45 min | – | [78] |
| | | | | Acetone | 500 | RT | [e]34 | 70/55 min | – | |
| | $MgCo_2O_4$ | Nanoparticles | Microwave-assisted colloidal | Acetone | 50 | 250 | [a]17.4 | 20.1/97.3 s | 0.5 ppm | [79] |
| | $MoS_2/NiCo_2O_4$ | Nanoparticles | Hydrothermal | Ethanol | 100 | 170 | [a]9 | 21/10 s | 0.1 ppm | [37] |
| | $Ni_xCo_{3-x}O_4$ | Nanoparticles | Co-precipitation/ Thermal decomposition | CO | 20 | 120 | [b]2.5 | – | 0.66 ppm | [80] |
| | g-$C_3N_4/NiCo_2O_4$ | Spherical nanoparticles | Hydrothermal | Ethanol | 100 | 110 | [a]19.2 | 21/11 s | 10 ppb | [81] |
| | $In_2O_3$/YSZ/$NiCo_2O_4$ | Nanoparticles | Self-propagating high-temperature | Ammonia | 50 | 500 | [e]87.19 | – | – | [82] |
| | $NiCo_2O_4$ | Nanoparticles | Hydrothermal | Acetone | 500 | RT | [f]72 × $10^{-3}$ | 20/26 s | – | [83] |
| | $FeCo_2O_4$/graphene | Nanoparticles | Hydrothermal | Acetone | 500 | RT | [e]46 | 31/19 s | – | [84] |
| | $WO_3/FeCo_2O_4$ | Nanoparticles | Hydrothermal | Ammonia | 100 | 300 | [a]33.4 | 32.5/20.2 s | – | [85] |
| | ZnO/$ZnCo_2O_4$ | Nanodots | Hydrothermal/ Co-precipitation | Acetone | 10 | 240 | [a]15.3 | 7.7/10.3 s | 5 ppm | [86] |
| | ZnO/$ZnCo_2O_4$ | Nanoparticles | Hydrothermal | Ethylene glycol | 100 | 160 | [a]15.5 | 90/45 s | 1.59 ppm | [87] |
| | $ZnCo_2O_4$ | Nanoparticles | Co-precipitation/ digestion | Liquefied petroleum gas | 50 | 350 | [a]72 | 90/80 s | – | [88] |
| | $ZnCo_2O_4$/Polypyrrole | Nanoparticles | In situ chemical polymerization | Acetone | 0.7 | RT | [b]0.39 | 85/34 s | – | [77] |
| 1D | $Co_3O_4/NiCo_2O_4$/CC | Nanowires | Hydrothermal | Ethanol | 200 | 180 | [a]35 | 7/10 s | – | [89] |
| | $NiCo_2O_4$/rGO | Nanowires | Hydrothermal | $H_2S$ | 100 | R | [a]3.51 | 2/449 s | – | [90] |
| | Pd/$NiCo_2O_4$ | Nanoneedles | Thin film deposition/ Hydrothermal | $H_2$ | 300 | 300 | [b]533 % | 26/23 s | 131 ppb | [91] |
| | $NiCo_2O_4$/rGO | Nanorods | Hydrothermal | Ammonia | 100 | RT | [a]1.068 | 57/185 s | – | [92] |
| | $NiCo_2O_4$ | Nanorods | Hydrothermal | Ammonia | 25 | RT | [a]3.4 | 33/249 s | – | [93] |
| | $NiCo_2O_4$ | Hierarchical hollow microtubules | Template-assisted process/Etching treatment | Xylene | 100 | 220 | [a]9.25 | 20/9 s | 1 ppm | [94] |
| | $NiCo_2O_4/SnO_2$ | Nanofiber | Electrospinning/ Hydrothermal | Ethanol | 100 | 160 | [a]8.87 | 114/115 s | 5 ppm | [95] |
| | Zn@$NiCo_2O_4$ | Mesoporous rods | Hydrothermal | $NO_x$ | 10 | 200 | [b]7.4 | 28/30 s | – | [96] |
| | CuO/$CuCo_2O_4$ | Nanotubes | Electrospinning | n-Propanol | 10 | RT | [a]14 | 6.3/4.1 s | – | [97] |
| | $TiO_2/ZnCo_2O_4$ | Porous nanorods | Dual-oxalate sacrificial template | HCHO | 100 | 130 | [a]4.1 | 120/200 | 1.04 ppm | [98] |
| | | | | TEA | 100 | 220 | [a]15 | 9/77 s | 1.12 ppm | |
| | $ZnCo_2O_4$ | Porous nanorods Single-layer nanochain | Co-precipitation | TEA | 100 | 200 | [a]2.7 [a]14 | 10/120 s 7/57 s | – – | [99] |
| | $ZnCo_2O_4$ | Microtubes | Biomorphic template | $H_2S$ | 10 | 90 | [a]6.37 | 100/104 s | 50 ppb | [100] |
| | ZnO/$ZnCo_2O_4$ | Nanotubes | Capillary electrospinning | Acetone | 100 | 175 | [a]34 | 3.2/3.4 s | – | [101] |
| | ZnO/$ZnCo_2O_4$ | Tube in tube nanostructure | Capillary electrospinning | Ethanol | 100 | 150 | [a]58 | 5.6/4.8 s | – | [102] |
| | | | | Acetone | 100 | 150 | [a]38 | 6.4/8.2 s | – | |
| | | | | $NH_3$ | 100 | 150 | [a]21 | 9.3/11.7 s | – | |
| | | | | Methanol | 100 | 175 | [a]25 | 6.7/9.5 s | – | |
| | $Zn_xCo_{2-x}O_4$ | Nanorods | Co-precipitation | Liquefied petroleum gas | 10 | 250 | [a]77.5 | 80/65 s | – | [103] |
| 2D | $MgCo_2O_4$ | Nanosheets | Hydrothermal | Ethanol | 500 | RT | [f]81 × $10^{-3}$ | 15/19 s | – | [104] |
| | $NiCo_2O_4/WO_3$ | Nanosheets | Hydrothermal/ Co-precipitation | Xylene | 100 | 300 | [a]15.69 | – | 5 ppm | [105] |
| | ZnO/$NiCo_2O_4$ | Nanosheets with nanofibers | Hydrothermal | Methanol | 100 | 250 | [a]6.77 | 37/175 s | – | [106] |
| | $NiCo_2O_4$/MWCNTs | Nanoflakes | Hydrothermal | Ammonia | 100 | RT | [g]25.7 | – | – | [107] |
| | $NiCo_2O_4$ | Nanoflakes | Co-precipitation | Ammonia | 10 | RT | [b]109 % | 44/18 s | – | [108] |
| | $NiCo_2O_4$ | Nanoplates | Hydrothermal | Triethylamine | 10 | 220 | [a]2.53 | 33/42 s | 500 ppb | [109] |
| | $NiCo_2O_4/\alpha$-$MoO_3$ | Porous nanosheets | Co-precipitation | Ethanol | 1 | 350 | [a]20 | – | 50 ppb | [110] |
| | $NiCo_2O_4$ | Nanosheets | Hydrothermal | Formaldehyde | 100 | 225 | [a]70 | 22/34 s | – | [111] |

(continued on next page)

**Table 4** (*continued*)

| Dimension | Composites | Microstructures | Synthesis method | Target gas | Concentration (ppm) | T (°C) | Response | Response/ Recovery time | LOD | Ref. |
|---|---|---|---|---|---|---|---|---|---|---|
| | $NiCo_2O_4$/rGO | Nanoplates | | Alcohol | – | 280 | – | – | – | [112] |
| | $CuCo_2O_4$ | Nanosheets | Solution combustion method | Ozone | 1 | 90 | [a]27 | – | 3.9 ppb | [113] |
| | $CuCo_2O_4$ | Nanoplatelets | Hydrothermal | Ammonia | 400 | RT | [b]7.9 % | – | – | [114] |
| | $MoS_2$–$ZnCo_2O_4$–$ZnCo_2O_4$/CC | Nanosheets | Hydrothermal | $H_2S$ | 1 mM | 37 | 3.8 mA | – | 5 nM | [115] |
| | $ZnCo_2O_4$ | Porous nanosheets | Hydrothermal | $H_2S$ | 5 | 120 | [a]6.27 | 35/- s | 100 ppb | [116] |
| | $ZnCo_2O_4$ | Nanosheet arrays | Hydrothermal | Methanol | 100 | 400 | [a]9 | 2/23 s | – | [117] |
| 3D | $Co_3O_4$/$NiCo_2O_4$ | Nanocages | Hydrothermal/ Co-precipitation | $H_2S$ | 100 | 250 | [a]57 | 153/40 s | – | [118] |
| | NiO/$NiCo_2O_4$ | Hierarchical microspheres | Hydrothermal | Xylene | 50 | RT | [a]4 | 8/4 s | 0.5 ppm | [119] |
| | $NiCo_2O_4$ | Nanospheres | Hydrothermal | Xylene | 100 | 260 | [a]16.4 | 26/27 s | – | [120] |
| | PdO–NiO/$NiCo_2O_4$ | Truncated Nanocages | Coprecipitation/ etching/wet impregnation | Acetone | 100 | 210 | [a]6.7 | 19/28 s | – | [121] |
| | NiO/$NiCo_2O_4$ | Hollow microspheres | Co-precipitation | Acetone | 100 | 160 | [a]17.86 | 11/13 s | 25 ppb | [76] |
| | $Co_3O_4$/$NiCo_2O_4$ | Nanocages | Co-precipitation | Acetone | 100 | 238.9 | [a]3.1 | 8/20 s | – | [122] |
| | $NiCo_2O_4$/$WO_3$ | Nanoflowers | Hydrothermal | $NO_2$ | 20 | 150 | [a]116.9 | 13/16 s | 52 ppb | [123] |
| | $NiCo_2O_4$ | Hollow microspheres | Hydrothermal | Triethylamine | 500 | 180 | [a]2.26 | 30/37 s | 145 ppb | [124] |
| | $NiCo_2O_4$ | Hierarchical microflowers | Hydrothermal | n-butanol | 100 | 165 | [b]240 % | 68/107 s | – | [125] |
| | $NiCo_2O_4$ | Double-shelled hollow spheres | Self-template | Xylene | 100 | 240 | [a]23.3 | 15.4/30.5 s | 0.5 ppm | [126] |
| | PANI/$NiCo_2O_4$ | Nanospheres | Hydrothermal | Ammonia | 20 | RT | [a]4.67 | 22/62 s | 216 ppb | [127] |
| | $Cu_{0.3}Co_{2.7}O_4$ | Hollow microspheres | Hydrothermal | Ethanol | 50 | 190 | [a]2.09 | – | – | [128] |
| | ZnO/$ZnCo_2O_4$ | Hexahedral-structure | Hydrothermal | Formaldehyde | 20 | 200 | [a]17 | 390/174 s | – | [129] |
| | $ZnCo_2O_4$ | Hierarchical porous architectures | Hydrothermal | Xylene | 200 | 260 | [a]50 | 1/12 s | 1 ppm | [130] |
| | $Co_3O_4$/$ZnCo_2O_4$ | Hollow nanostructures | Self-sacrificing template | Acetone | 100 | 255 | [a]16.3 | 41/47 s | 0.51 ppm | [131] |
| | Ag–$ZnCo_2O_4$ | Hollow microspheres | Solvent-thermal | Formaldehyde | 100 | 99.3 | [a]11.18 | 76/127 s | – | [132] |
| | $ZnCo_2O_4$ | Hierarchical microflowers | Solvothermal | Acetone | 100 | 200 | [a]32.32 | 2.6/8.8 s | 50 ppb | [133] |
| | $ZnCo_2O_4$ | Yolk-shell spheres | Hydrothermal | Acetone | 500 | 200 | [a]38.2 | 19.72/500 s | 0.5 ppm | [134] |
| | Ag@$ZnCo_2O_4$ | Hollow spheres | Self-sacrificing template | Acetone | 20 | 220 | [a]12 | 12/54 s | 0.25 ppm | [135] |
| | $ZnCo_2O_4$ | Yolk-shell microspheres | Co-precipitation | Ozone | 890 ppb | 200 | [b]71 % | 37.4/1260 s | 80 ppb | [136] |
| | ZnO/$ZnCo_2O_4$ | Hierarchical structure | Hydrothermal | TEA | 100 | 220 | [a]5.12 | 8/65 s | 800 ppb | [137] |
| | Pd–ZnO/$ZnCo_2O_4$ | Hollow spheres | MOF templated synthesis | Acetone | 5 | 250 | [b]69 % | – | – | [138] |
| | PdO–ZnO/$ZnCo_2O_4$ | Microspheres | Co-precipitation | Formaldehyde | 100 | 139 | [a]26.9 | 9/14 s | 0.2 ppm | [139] |
| | $ZnCo_2O_4$ | Hollow polyhedral superstructure | Co-precipitation | Ethanol | 20 | 200 | [b]14.2 | 22/62 s | 1 ppm | [140] |
| | $ZnCo_2O_4$ | Multishelled | Solvothermal | Formaldehyde | 0.6 | 170 | [b]12 | 15/266 s | – | [36] |
| | | Hollow Twin Spheres | | Propanal | 0.6 | 190 | [b]16 | 3/100 s | – | |
| | ZnO/$ZnCo_2O_4$ | Hierarchical macroporous honeycomb-like | Self-template | CO | 10 | 300 | [a]17.3 | 300/50 s | – | [141] |
| | $Zn_xCo_{3-x}O_4$ | Nanocages | Co-precipitation | Acetone | 200 | 170 | [a]35.6 | 43/51 s | 0.5 ppm | [142] |
| | $ZnCo_2O_4$ | Cabbage-shaped | Co-precipitation | Formaldehyde | 100 | 180 | [a]7.4 ± 0.5 | 9/12 s | – | [143] |

RT: Room temperature.
CC: Carbon cloth.
[a]Gas response S=$R_g/R_a$.
[b]Gas response S=$(R_a-R_g)/R_a$.
[c]Gas response S = $\triangle V_a$-$\triangle V_b$ ($\triangle$V is the electric potential difference of the sensor).

[d]Gas response S = peak current.
[e]Gas response S = counts/ppm.
[f]Gas response S = output voltage/gas concentration.
[g]Gas response S= $C_{gas}/C_{air}$ ($C_{air}$ represents the capacitance of the sensor in the air and $C_{gas}$ is the capacitance in testing gas.

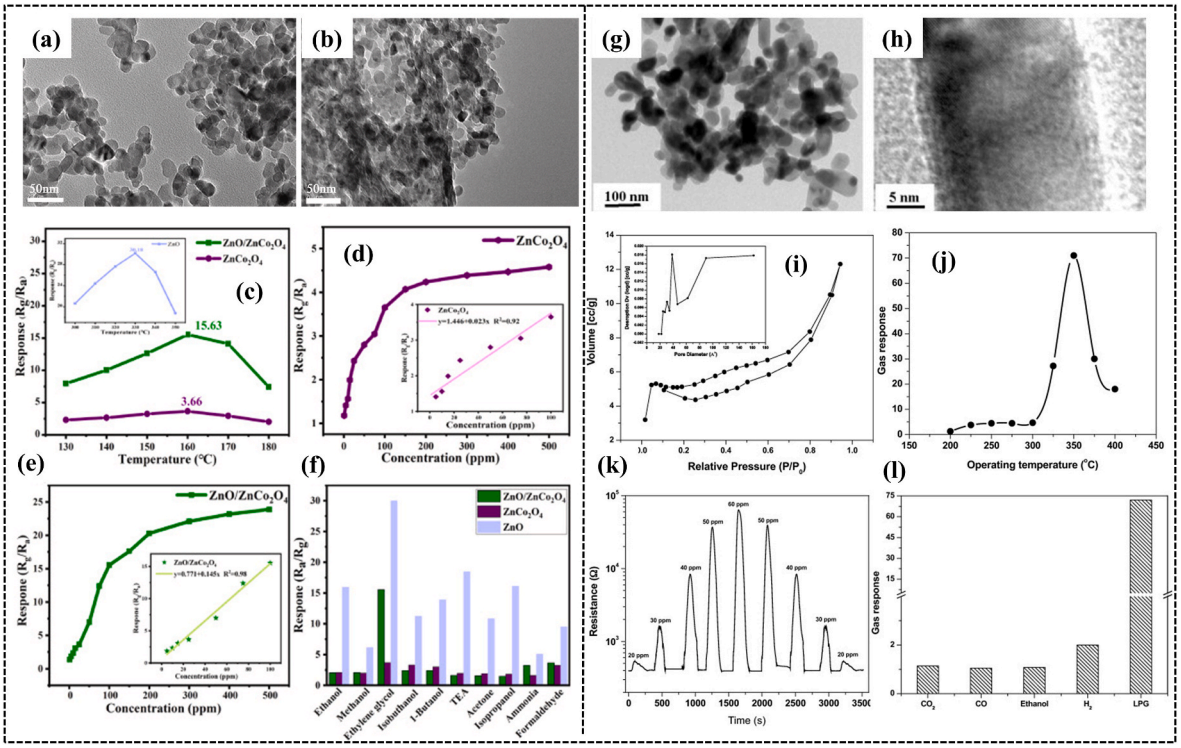


**Fig. 2.** TEM images of (a) $ZnCo_2O_4$ and (b) $ZnO/ZnCo_2O_4$. (c) The responses to 100 ppm ethylene glycol at different operating temperatures from 130 to 180 °C, (d and e) the responses to different concentrations of ethylene glycol ranging from 5 to 500 ppm at 160 °C, (f) the response values of the sensors to 100 ppm different gases at the optimum operating temperature. (Reproduced with permission from Ref. [87], Copyright© 2022, Elsevier). TEM (g) and HRTEM (h) images of nanostructured $ZnCo_2O_4$. (i) Nitrogen adsorption–desorption isotherm of nanostructured spinel $ZnCo_2O_4$. Inset shows the BJH pore size distribution obtained from the desorption branch of isotherm. (j) Effect of operating temperature on the gas response of nanostructured spinel $ZnCo_2O_4$ to 50 ppm LPG. (k) Response of nanostructured spinel $ZnCo_2O_4$ upon sequential exposure to LPG with concentrations varying from 20 to 60 ppm at 350 °C. (i) Bar chart showing the gas response of nanostructured spinel $ZnCo_2O_4$ for different gases. The gas concentration and operating temperature in all cases were 50 ppm and 350 °C, respectively. (Reproduced with permission from Ref. [88], Copyright© 2011, Elsevier).

molecules [165]. Polymer polypyrrole (PPy) has shown the potential gas sensor application for its tunable electrical and nonlinear optical properties [166,167]. By constructing $ZnCo_2O_4$/PPy and $MnCo_2O_4$/PPy heterojunction nanocomposites via a hydrothermal method, a highly sensitive acetone gas sensor was obtained as the ternary spinel SMOX served on effective catalysts for gas molecules oxidation due to the combination of couples $M^{3+}/M^{2+}$ (Zn and Mn) and $Co^{3+}/Co^{2+}$ [36,77]. Yuan et al. reported that they loaded $FeCo_2O_4$ nanoparticles on the $WO_3$ nanosheets to form the p-n heterogenous junction for constructing the $NH_3$ gas sensors with superior performance. $WO_3$ oxide nanosheets coated with $FeCo_2O_4$ nanoparticles were synthesized via regluating the content of HCl in precursor solution. The corresponding gas sensor synthesized by adding 2 mL HCl diplayed highest response (34 @ 100 ppm), which is primarily due to the special binding form of $Co^{2+}$, $Co^{3+}$ and $NH_3$. Meanwhile, the extra nanostructure and p-n heterojunction benefits the sensing performance as well [85].

On the other hand, in addition to the traditional hydrothermal method, other methods, including co-precipitation [80], microwave-assisted colloidal [79], self-propagating high-temperature synthesis [82], soultion combustion [168] et al. are employed to fabricating 0D $MCo_2O_4$ gas sensors. The nanostructured $ZnCo_2O_4$ were obtained utilizing the co-precipitation and digestion methods while the $ZnCo_2O_4$ nanoparticles with the size of 30–40 nm and the BET surface area of 16.2 $m^2/g$ were obtained as shown in Fig. 2a-c. As evident in Fig. 2d-f, the as-fabricated sensor demonstrated the outstanding sensitivity of 72 towards 50 ppm LPG at the optimal operating temperature, excellent dynamic response conditon and superior selectivity, which shed some light on combustible and explosive energy gas detection [88]. Via regulating the Ni/Co content in nanocrystalline $NiCo_2O_4$, Vladimirova et al. obtained the $Ni_xCo_{3-x}O_4$ product by co-precipitation strategy for exploring the impact of cationic distribution on sensing performance of carbon monoxide. The $Ni_xCo_{3-x}O_4$ samples were formed from aggregated nanoparticles with the wide size distribution interval from 20 nm to 100 nm). In detail, the nanoparticles own a cellular nanostructure with the average pore diameter of about 8–15 nm, which is due to the gas emmission (CO, $CO_2$) in time of oxalate precursor decomposition. With the increase in Ni proportion, the gas sensitivity of CO decreases, owing to the decline of adsorbed oxygen concentration on $Ni_xCo_{3-x}O_4$ surface [80]. Morán-Lázaro et al. reported a microwave-assisted colloidal techique to obtain $MgCo_2O_4$ nanoparticles and the size of nanoparticles are 6–33 nm while their average size is around 16 nm, which aggregate to form the irregular porous microstructure. Dioctyl sulfosuccinate sodium salt (AOT), an effective surfactant, made the porous structure synthesized successfully. Exploring on the acetone sensing performance revealed that the response can reach 17.4 under 100 ppm target gas at 250 °C under low-humidity conditions. Nevertheless, on the account of competition of water molecules on the $MgCo_2O_4$, response drops below 2 when the ambient RH is 50 % [79].

Due to the high RH environment, some hydroxyl groups are prone to absorb on the surface of sensing material. Because of the existence of hydroxyl groups, the highly stable adsorption states can be formed. Thus, the hydroxyl groups interferes with the regular sensing process by preventing it from reacting with the reaction sites on the surface [169, 170]. It can be seen that the sample synthesized by microwave hydrothermal method possessed high purity and reaction conditions is mild, which should be widely used in the synthesis of 0D $MCo_2O_4$. Furthermore, co-deposition and hydrothermal method were combined to successfully modify ZnO nanorods with $ZnCo_2O_4$ nanodots. The $ZnCo_2O_4$/ZnO precursor was obtained appropriately by adding certain amount of NaCl for inhibiting deposition of crystallites. Furthermore, based on the thermogravimetric (TG) curve, the 600 °C was selected as the optimal calcination temperature to obtain the best substance. Thus, the gas sensor exhibited intensive response of 15.3 and rapid response process of 7.7 s at 240 °C towards 10 ppm acetone, which was attributed to the ZnO nanorods surface modifications by adding $ZnCo_2O_4$ nanodots [86]. As stated above, 0D $MCo_2O_4$ synthesized by most researchers typically are nanoparticles or clusters, which have established the basis for subsequent assembly into 3D $MCo_2O_4$ materials.

### 3.2.2. 1-dimensional (1D) $MCo_2O_4$

Up to now, a wide variety of 1D $MCo_2O_4$, containing nanorods, nanofibers, nanowires, nanotubes, nanoneedles and nanochains are explored for improving sensing performance. Due to inherent quantum confinement properties of 1D material, they have unique shapes and size dependent features, considered as an exciting class of materials for many nano-technology related sensors [171]. Among the developed synthesis methods, hydrothermal and solvothermal methods are extensively used because of high yield, facile control and operation simplicity [70]. For example, a $Co_3O_4$/$NiCo_2O_4$/Carbon cloth (CC) mutli-layered nanostructure was prepared for ethanol sensing application. Specifically, CC is applied for rock-bottom template while cobaltate, nickelate and cetyltrimethyl ammonium bromide (CTAB) were added during hydrothermal reaction to form ZIF-67/$NiCo_2O_4$/CC. Finally, $Co_3O_4$/-$NiCo_2O_4$/CC was successfully obtained by calcination at 350 °C during 1 h with the heating rate of 1 °C per minute. By this ordered synthesis route as demonstrated in Fig. 3a, uniform $Co_3O_4$ nanocubes grown on the $NiCo_2O_4$ nanowires of around 80 nm in diameter based on the CC substrate (Fig. 3b and c). Surprisingly, the as-developed sensors demonstrated the excellent sensing performance (35 @ 200 ppm ethanol) at 180 °C as depicted in Fig. 3d and e. The strengthened sensing performance is derived from the porous nanostructure and facilitated carrier transportation between CC and $Co_3O_4$ nanocube group [89]. In Ref. [90], $H_2S$ sensing with $NiCo_2O_4$/reduced graphene oxide (rGO) nanocomposites electronic devices was firstly reported by Wu et al. From SEM results, $NiCo_2O_4$ nanowires with the diameter of 5–7 μm tightly fixed on the rGO layered structure, coming into being a great number of active sites. Furthermore, the excellent response (3.51) and ultrafast response process (2 s) towards 100 ppm $H_2S$ were achieved which was attributed to the catalytic action of sensing layer. The group of Marimuthu et al. employed rGO catalyst for functionalizing of $NiCo_2O_4$. The composites are made up of rGO nanosheets and $NiCo_2O_4$ nanorods which are attached to a certain center forming a bunch-like nanostructure. The sensors exhibited high sensitivity, excellent reproducibility of ten days period and fast response/recovery reaction to $NH_3$ [92]. Furthermore, the $Co_3O_4$ nanoparticles and $NiCo_2O_4$ nanorods were prepared respectively to fabricate the ammonia sensor by Marimuthu et al. while the sensing performance at room temperature of the latter one was better [93]. Kumar et al. adopted a facile hydrothermal strategy for mesoporous Zn doped $NiCo_2O_4$ rods preparation. The length of log-liked $Ni_{0.8}Zn_{0.2}Co_2O_4$ rod is 5–10 μm while the BET surface area of which is as high as 76 $m^2$/g. Compared to the pure $NiCo_2O_4$ and $ZnCo_2O_4$ nanorods, the $Ni_{0.8}Zn_{0.2}Co_2O_4$ sensor exhibited higher response (7.4 @ 10 ppm) and short response time towards $NO_x$ [96].

The $MCo_2O_4$ sensor owns better performance by combining the traditional hydrothermal method with different deposition methods. For fabricate an more effective hydrogen sensor, the $NiCo_2O_4$ nanoneedle

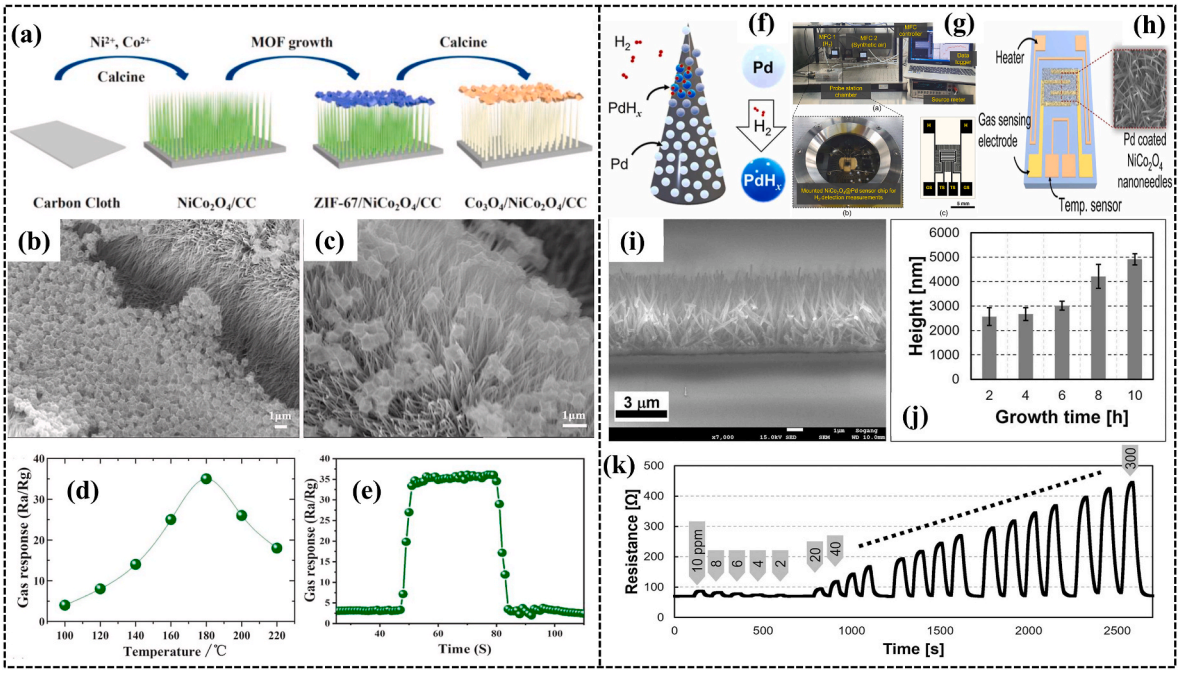


**Fig. 3.** (a) Growth mechanism diagram of synthesis process of $Co_3O_4$/$NiCo_2O_4$/CC. (b–c) SEM images of $Co_3O_4$/$NiCo_2O_4$/CC under different magnification. (d) Gas response of $Co_3O_4$/$NiCo_2O_4$ exposed to 200 ppm ethanol at different temperature. (e) Response and recovery curves under 200 ppm of ethanol at 180 °C. (Reproduced with permission from Ref. [89], Copyright© 2021, Elsevier). (f) The process of $H_2$ adsorption by Pd coated on the surface of $NiCo_2O_4$ NNF. (h) Experimental setup for target gas sensing measurements. (g) Schematic illustration of proposed $H_2$ sensor. (i–j) SEM images of cross-sections of structure with 10 h for NNF and comparison graph of structure layer height according to growth time. (k) Comparison of responses of the fabricated device to various $H_2$ concentrations (Reproduced with permission from Ref. [91], Copyright© 2023, Elsevier).

forest which deposed on Pd thin film was applied as shown in Fig. 3f–h. Through field emission scanning electron microscope (FESEM) results, the height of nanoneedle forest is proprotional to the synthesis time and which can reach 4.9 μm after 10 h heating as illustrated in Fig. 3i and j. Meanwhile, the diameter of the single nanoneedle also becomes larger after prolonging the hydrothermal time. By depositing an ultrathin Pd film on the sensors, the intricated reaction between $H_2$ molecules and sensing material surface can be motivated while the fabrication costs can be reduced. Furthermore, the high BET surface area and appropriate porosity also improve the sensitivity a lot (Fig. 3k) [91].

Furthermore, Wang et al. combined electronspinning and hydrothermal methods to synthesize the $NiCo_2O_4/SnO_2$ heterostructure. The $SnO_2$ nanosheets were adhered unifromly to the $NiCo_2O_4$ nanofibers, leading to the loose and polyporous structure and increased exposed active sites as shown in Fig. 4a-g, which improved the response values 8 times than that of pure $NiCo_2O_4$ towards 100 ppm ethanol at optimum working temperature of 160 °C (Fig. 4h). Interestingly, a typical logarithmic relationship between response and ethanol concentration was discerned in Fig. 4i [95].

Besides adopting traditional hydrothermal method, electrospinning, coprecipitation and template method were also commonly used for the synthesis of 1D $MCo_2O_4$. For example, Alali et al. established CuO/$CuCo_2O_4$ p-p heterojunction employing electronspinning strategy for n-propanol detection at room temperature. The CuO/$CuCo_2O_4$ nanotubes with hollow and uniform features were obtained and the diameter of which was calculated to be 60–70 nm [97].

Meanwhile, a p-n ZnO/$ZnCo_2O_4$ heterojunction was reported by the preparation of single capillary electrospinning technology and post-annealing possess. Obviously, the diameter of hollow ZnO/$ZnCo_2O_4$ nanotubes cross profile is about 100–150 nm and the wall thichness is about 20 nm. The excellent gas sensitivity (34 @ 100 ppm) and ultra-short response/recovery time (3.2/3.4 s) towards acetone are acquired which is derived from the distinct morphology and p-n heterostrucure [101]. Interestingly, $TiO_2$ can replace ZnO totally to form heterojunction with 1D $MCo_2O_4$. A p-n $TiO_2/ZnCo_2O_4$ heterojunction was constructed by sacrificial template method and acquired the best relevant gas sensor through changing the amount of $TiO_2$. The $TiO_2/ZnCo_2O_4$ nanorods consisting of abundant irregular nanoparticles (5–20 nm) are discerned and the adding of $TiO_2$ exerts no distinct impact on morphology. Specifically, the $ZnCo_2O_4$ nanorods with the optimum $TiO_2$ content (4 wt%) discriminate HCHO and triethylamine (TEA) effectively. The developed gas sensor has the high response (15 @ 100 ppm) towards TEA at 220 °C and the response time is decreased to 9 s [98]. Meanwhile, TEA detection was also carried out using $ZnCo_2O_4$ by Luo et al. By adjusting the calcination time (350 °C and 500 °C), porous $ZnCo_2O_4$ nanorod and single-layer $ZnCo_2O_4$ nanochain can be obtained, respectively. The $ZnCo_2O_4$ calcined at 500 °C exhibited better TEA sensing performance and the larger available surface area should be the primary reason [99]. The $ZnCo_2O_4$ microtubes as shown in Fig. 4j and k adopting absorbent cotton as template was synthesized by Xu et al. The immersion tactic in metal salt solution and calcination treatment in ambient atmosphere were combined to target material. By regulating calcination temperature (500 °C, 600 °C and 700 °C), the percentage of chemisorbed oxygen in ZCO600 declined from 37.81 % to 31.77 % and the oxygen vacancy increased after the $H_2S$ molecules adsorption, indicating $H_2O$ and $SO_2$ were generated after $H_2S$ reacted with $O_2$ as shown in Fig. 4l. Furthermore, the gas sensor fabricated under 600 °C annealing temperature demonstrated rapid recovery process of 104 s to $H_2S$ (5 @ 10 ppm) and the lowest LOD of 50 ppb at 90 °C as shown in Fig. 4m and n. In particular, XPS analysis were employed to evaluate the valence state of element on the surface of $ZnCo_2O_4$ when the as-prepared sensor contacted with $H_2S$ at 90 °C [100]. The research provided us a more

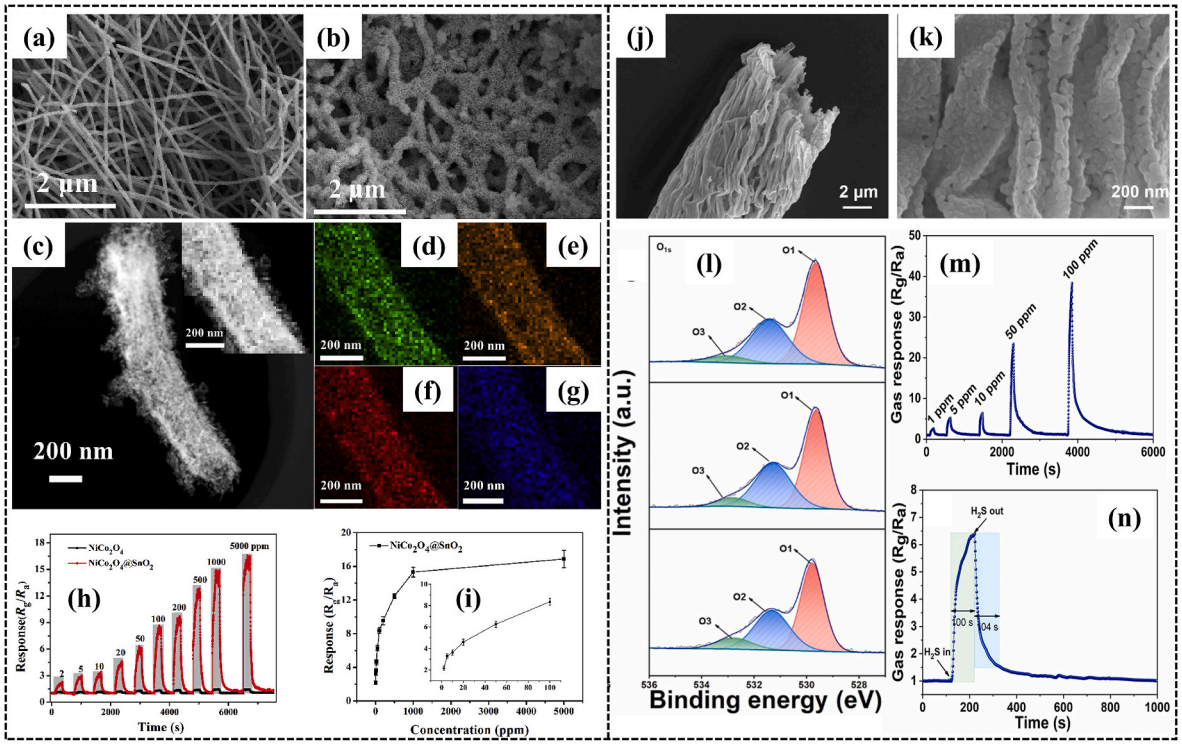


**Fig. 4.** SEM images of (a) $NiCo_2O_4$ and (b) $NiCo_2O_4@SnO_2$. (c) HAADF-STEM image of $NiCo_2O_4@SnO_2$ composites. (d–g) EDX elemental mappings of Ni, Co, O and Sn, respectively. (h) Dynamic transient for response of $NiCo_2O_4$ nanowires and $NiCo_2O_4@SnO_2$ composites to 2–5000 ppm ethanol at optimal working temperature of 160 °C. (i) $NiCo_2O_4@SnO_2$ sensor response vs. ethanol concentration (2–5000 ppm) at 160 °C, inset is the corresponding responses at low ethanol concentrations. (Reproduced with permission from Ref. [95], Copyright© 2019, Elsevier). (j, k) SEM images of ZCO-600. (l) O 1s XPS spectrum of ZCO-500, ZCO-600 and ZCO-700. (m) Dynamic sensing response to different concentrations of $H_2S$ at 90 °C. (n) Dynamic response-recovery curve to 10 ppm $H_2S$. (Reproduced with permission from Ref. [100], Copyright© 2022, Elsevier).

effective strategy to verify the physicochemical change before and after the adsorption process. Furthermore, the calcination temperature has displayed a crucial impact on the surface activity of the $MCo_2O_4$, while the high surface activity will increase the active site and surface adsorption capacity, thus improving the adsorption performance.

By modifying the elemental ratio of zinc to cobalt from 1 : 1 to 1 : 2.5 in $ZnCo_2O_4$ nanorods synthesized via co-precipitation/digestion strategy, Gawande et al. fabracated the gas sensor with optimum zinc-cobalt ratio (1 : 2.5) for liquefied petroleum gas (LPG) detection. The $ZnCo_{2.5}O_4$ nanorods were observed with diameter of 6–8 nm and length of 30–50 nm. Towards the LPG gas (10–80 ppm), the developed sensors exhibited high response, good selectivity and repeatability for 40 cycles [103]. Du et al. successfully synthesized a hierarchical tubular $NiCo_2O_4$ nanostructures which assembled by nanosheets via template method and etching treatment for xylene detection. In detail, the Ni–Co precursor was anchored on $Ag_8W_4O_{16}$ templates firstly and the $Ag_8W_4O_{16}/NiCo_2O_4$ composites can be obtained after annealing possess. Then nitric acid and ammonia are used for the removal of $Ag_8W_4O_{16}$ templates and the thickness of $NiCo_2O_4$ nanosheets obtained is around 5 nm and the average length of assembled microtubes is 1.1 μm [94]. As described above, large specific surface area, fast carrier diffusion rate and strong structural stability compared with other dimensional materials, the three leading advantages which 1D $MCo_2O_4$ owns, endow them excellent gas sensing performance. However, due to the characteristics of the synthesis method, the reagent needs extremely high purity to ensure the quality of the product, therefore the large-scale production and widespread practical application of 1D $MCo_2O_4$ materials still need a lot of attempts and efforts.

### 3.2.3. 2-dimensional (2D) $MCo_2O_4$

At present, many researchers have been motivated to find more 2D $MCo_2O_4$ materials which possess special thickness tied properties in both chemistry and physics [4]. However, there is the tendency of abundant low dimensional nanomaterials taking shape in dense stacked nanostructure in time of establishment of the 2D conductive network, which is not beneficial to support sufficient contact between the lamellae inside the network and target gas, resulting in the decrease of sensitivity and response rate [172]. Therefore, some 2D materials with extremely ordered morphology can be obtained by synthesizing on some hard templates like Ni foam which possesses 3D grid microstructure and its large porosity can provide more location for the orderly growth of materials. The research group of Yin has fabricated special hexagonal $ZnCo_2O_4$ nanosheets arrays of single crystalline developed on nickel foam by a two-step synthesis method including hydrothermal and air calcination possess, which own high specific area (94.1 $m^2/g$) and mesoporous structure properties contributing to the enhancing sensing performance. From FESEM results, the prepared hexagonal $ZnCo_2O_4$ nanosheets with the thickness of 84 nm attached to Ni foam densely. The response value of $ZnCo_2O_4$ sensor was 9 towards 100 ppm methanol at 400 °C. As the gas concentration increased from 100 to 1000 ppm, the sensor displayed the outstanding sensitivity, good linearity and adequate selectivity to target gas over interfering gas [117]. $MgCo_2O_4$ nanosheets were firstly obtained with the thickness of 10–15 nm while the diameter of 200–250 nm employing a hydrothermal strategy. The as-prepared sample owned the high BET surface area of 98.5 $m^2/g$ and the according sensor displayed high response to ethanol [104]. Xu et al. reported a novel $NiCo_2O_4/WO_3$ gas sensor for xyene detection. In detail, the 2D $NiCo_2O_4$ nanosheets are observed to stick to every single 1D $WO_3$ nanofiber uniformly. Residual $NiCo_2O_4$ nanoparticles still adhere on $WO_3$ nanofivers, which indicated low crystallinity of $NiCo_2O_4$ nanosheets. By exploring the xyene sensing performance, $NiCo_2O_4/WO_3$ gas sensors exhibited high response (Rg/Ra = 15.69), excellent selectivity and magnificent stability toward 100 ppm xyene at 300 °C on account of the unique and exquisite morphology and p-n heterojunction [105]. Liang et al. synthesized a novel ZnO-core/$NiCo_2O_4$-shell nanocomposite chemical bath deposition for methanol detection. Porous $NiCo_2O_4$ nanosheets anchored on the ZnO nanofiber. Apparently, the ZnO/$NiCo_2O_4$ sensor exhibited better sensing performance than both prisine ZnO and $NiCo_2O_4$. It should be noted that the complex and porous surface is of great benefit to sensing performance owing to the swift and adequate gas diffusion inclosing the material. The ZnO/$NiCo_2O_4$ gas sensor owned outstanding response of 6.77 towards 100 ppm methanol at 250 °C [106]. Marimuthu et al. synthesized an exquisite $NiCo_2O_4$/multi-walled carbon nanotubes (MWCNTs) nanocomposite for fabricating ammonia gas sensor via a hydrothermal method. The $NiCo_2O_4$ 2D nanoflakes wrap together with MWCNTs were observed and the pure $NiCo_2O_4$ exhibited the outstanding repeatability to ammonia whereas the $NiCo_2O_4$/MWCNTs nanocomposites do not achieve the same expectation, which may attribute to the loose combination of the composition [107]. As shown in Fig. 5a-d, a novel tortoise shell-like $NiCo_2O_4$ nanoplates for TEA detection was reported by the group of Zhao et al. The porous $NiCo_2O_4$ nanoplates which possessed large BET surface area (102.6 $m^2/g$) can be synthesized by annealing at the optimal temperature of 500 °C whereas the nanoplates are damaged and the larger pores can be observed when annealed at 700 °C. The developed gas sensors owned the high response towards TEA (2.58 @ 10 ppm) at the optimal temperature of 220 °C as shown in Fig. 5e and f. The Ni (II)/Ni (III) ratio of $NiCo_2O_4$ can be estimated to be 0.25 whereas the value is 0.32 for $NiCo_2O_4$ after TEA contact. The augment of Ni (II) contents in TEA sensing demonstrated reduction reaction occurred at Ni site [109]. Xu et al. reported a $NiCo_2O_4/\alpha$-$MoO_3$ nanostructure based gas sensor for highly sensitive ethanol detection. Abundant porous 2D $NiCo_2O_4$ nanosheets with the width of 500 nm anchoring uniformly on the α-$MoO_3$ 1D nanorods. The as-prepared gas sensors possessed the ultralow LOD (50 ppb) and the excellent response (20 @ 1 ppm) towards ethanol [110]. Jain et al. synthesized the $CuCo_2O_4$ nanoplatelets with mixed-valent by a hydrothermal strategy for $NH_3$ detection at room temperature. The size of porous $CuCo_2O_4$ nanoplatelets assembled by massive uniform nanoparticles is 10–15 nm. Furthermore, the gas sensing performance of $CuCo_2O_4$ sample which added 10 at.% Co revealed that the high response (7.9 % @ 400 ppm) was obtained in 57 % RH at room temperature [114]. Mani et al. reported a novel $MoS_2/ZnCo_2O_4/ZnCo_2O_4$/CC gas sensor for real-time $H_2S$ detection in live cells. The $MoS_2$ nanosheets grew and evenly distributed on the double-layered $ZnCo_2O_4$ nanosheets. Owing to the excellent surface properties, porous nanostructure, roughened catalytic sites generated by $MoS_2$, the $MoS_2/ZnCo_2O_4/ZnCo_2O_4$/CC sensor exhibited outstanding sensitivity, good selectivity, wide detection range and low LOD [115]. Combinations of heterojunctions may affect sensing performance, and more research is needed to optimize the assembly. Meanwhile, there are a number of studies on the detection of specific gases, such as methanol, ethanol, ammonia, and hydrogen sulfide, suggesting that these 2D $MCo_2O_4$ materials have potential applications in gas sensors.

At present, in addition to the traditional hydrothermal method, only solution combustion method and co-precipitation strategy were used separately for the synthesis of 2D $MCo_2O_4$ sensors. Sharma et al. applied co-precipitation method for $NiCo_2(OH)_6$ and $NiCo_2O_4$ gas sensor fabrication. Mesoporous $NiCo_2(OH)_6$ gas sensor displayed extraordinary response, fast response/recovery process to 2 ppm ammonia. Interestingly, the p-type $NiCo_2O_4$ gas sensor displayed the abnormal n-type sensing behavior after annealing possess which may due to the reducing of charge depletion width and incremental chemisorbed oxygen species, resulting in restoring the dominant charge carriers of $NiCo_2O_4$ [108]. Zhao et al. synthesized $CuCo_2O_4$ nanosheets as shown in Fig. 5g and h with regulable oxygen vacancy contents by controlling the amounts of citric acid in precursor employing solution combustion method. The as-prepared $CuCo_2O_4$ sample, with appropriate oxygen vacancy contents and high specific surface area of 53.7 $m^2/g$, which will supply sufficient adsorption sites and applicable passages for gas moleclues absorption and transportation. As shown in Fig. 5i–l, the developed gas sensors operated at a relative low temperature of 90 °C demonstrated high response (27 @ 1 ppm) towards ozone at 70 % RH, Computable

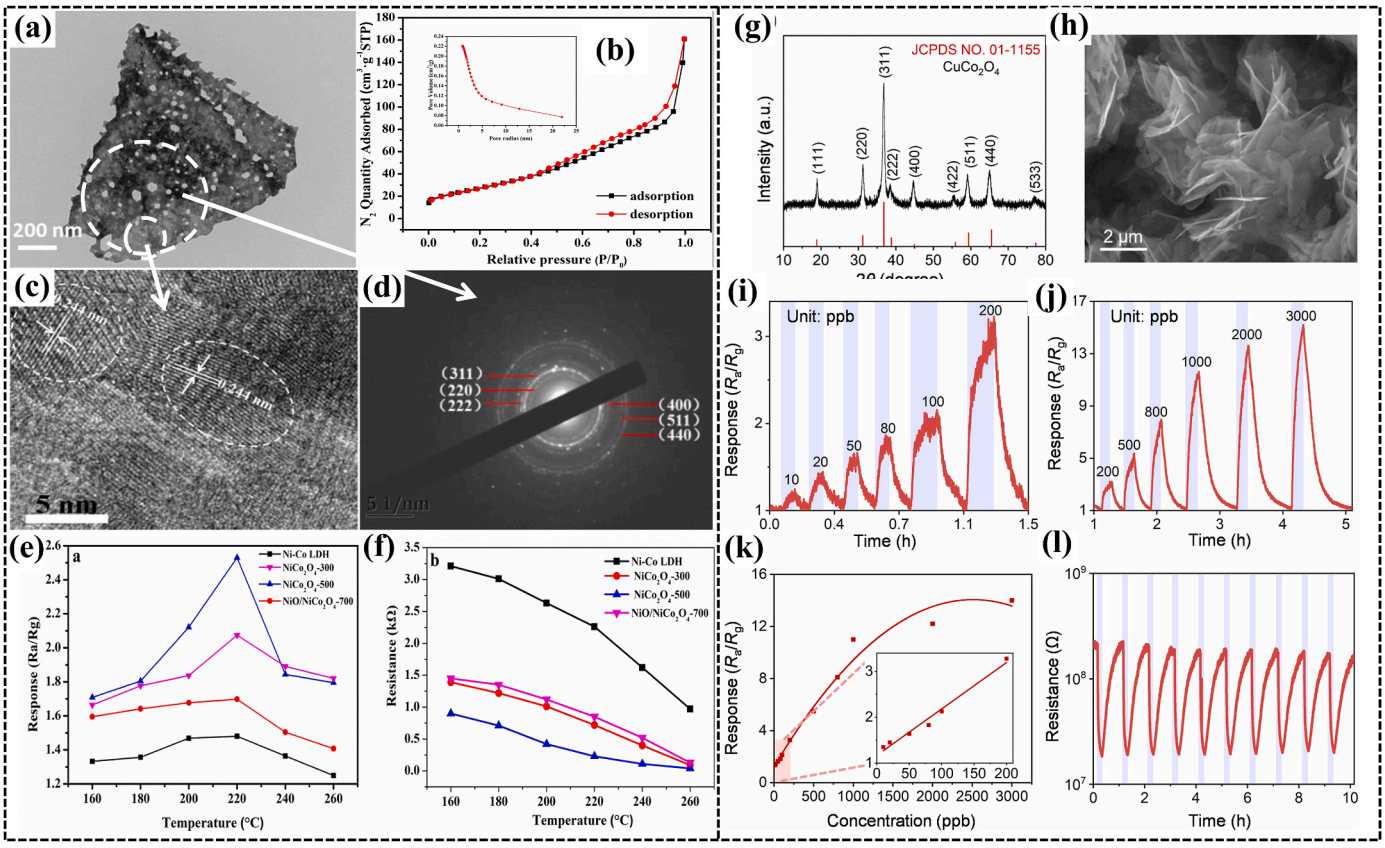


**Fig. 5.** (a) The TEM images of $NiCo_2O_4$ samples calcined at 500 °C. (b) Typical $N_2$ adsorptiondesorption isotherm of $NiCo_2O_4$-500. Inset is pore-size distribution curve. (c) HRTEM and (d) SAED images of $NiCo_2O_4$-500. (e) The response of as-prepared samples at different temperature to 10 ppm TEA, (f) the change in Ra with operating temperature. (Reproduced with permission from Ref. [109], Copyright© 2020, Elsevier). (g) XRD pattern and (h) SEM image of the as-synthesized $CuCo_2O_4$. Dynamic response-recovery curves of $CuCo_2O_4$ sensor to (i) 10–200 ppb $O_3$ and (j) 200–3000 ppb $O_3$. (k) The relationship of response versus $O_3$ concentration in the range of 10–3000 ppb and the inset: enlarged view of 10–200 ppb. (l) The continuous response to cyclic 1 ppm $O_3$. (Reproduced with permission from Ref. [113], Copyright© 2023, Elsevier).

response to concentration relationship, stable dynamic loop and superior reproducibility. In surprise, the response and the baseline resistance of $CuCo_2O_4$ gas sensor are positively correlated with the ambient humidity, contrary to the common situation [113]. When the developed sensors are placed at humidity environment, the absorption and dissociation of water molecule will generate electrons to $CuCo_2O_4$ while the recombination of hole carriers can be discerned, which is illustrated by Eq. (1) [173]:

$$O_2^- + 2H_2O \rightarrow 4OH^- + e^- \quad (1)$$

This reaction possessed a donor feature and reduced hole concentration, the baseline resistance thus rising with the increase of RH. There are two opposite effects on gas sensing application of p-type sensors as shown in Eq. (1). On the one hand, the active oxygen species $O_2^-$ can be reduced which is indicated in Eq. (2). However, the $O_3$ response mostly depends on Eq. (3), which results negative influence of humidity negligible. On the other hand, the hole carriers can be reduced as well which benefits the sensitivity [174].

$$O_3 + 2OH^- + 2e^- \rightarrow O_2 + 2O^- + H_2O \quad (2)$$

$$O_3 + e^- \rightarrow O^- + O_2 \quad (3)$$

### 3.2.4. 3-dimensional (3D) $MCo_2O_4$

$MCo_2O_4$ nanoparticles, nanowires and other low dimensional nanostructures are prone to spontaneously take shape in 3D $MCo_2O_4$ collective structures with periodic holes, named hierarchical nanostructures, which can maximize gas accessibility instead of sacrificing the hole accumulation layer onto the nanostructured block. In this way, excellent gas sensitivity and fast response are achieved simultaneously, which have made the 3D $MCo_2O_4$ sensors been reported the most.

Specifically, during the self-assembly process, the polymeric part will take shape in the center while the inorganic part will form on the outer surface. Then the 3D $MCo_2O_4$ nanostructures with hollow feature can be obtained by thermal decomposition of the core [175]. In several physicochemical methods, solvothermal and hydrothermal reactions are the most widely applied chemical routes for the preparation of highly crystalline grade and hollow 3D $MCo_2O_4$ nanostructures with periodic and well-defined pores. For instance, the hollow $Cu_{1-x}Co_{2+x}O_4$ (x = 0.7) microspheres were synthesized by employing a template-free hydrothermal strategy. The diameter of the microspheres is 3.6–4.0 μm while a detailed explanation of the time-dependent crystallization process indicated that the formation mechanism of $Cu_{0.3}Co_{2.7}O_4$ microspheres was mostly based on the Ostwald ripening mechanism [176]. Using this material for gas sensing testing, the response to ethanol can reach 2.09 at 190 °C [128]. Except 3D hollow $MCo_2O_4$ structure, the group of Ma find that an additional amount of sodium citrate (0.75 mmol) in the hydrothermal reaction processing of $ZnCo_2O_4$ with 3D hexahedral morphology can generate some ZnO phase, which presents better formaldehyde sensing properties compared with pure $ZnCo_2O_4$ [129]. To effectively test for TEA, ZnO/$ZnCo_2O_4$ microflowers with the diameter of 4 μm that comprised of abundant nanosheets with the average thickness of 15 nm were obtained. By adjusting the loading amount of zinc oxide, the overall carrier properties (p type/n type) of the ZnO/$ZnCo_2O_4$ SMOX and the content of adsorbed oxygen can be

changed while the better TEA gas sensor can be acquired. Under 220 °C, the ZnO/$ZnCo_2O_4$ gas sensor with 5%wt ZnO additive amount exhibited the repsonse of 5.12 with the response/recovery time of 8/65 s to 100 ppm TEA [137]. Three diverse hydrothermal paths were adopted to synthesize the $ZnCo_2O_4$ nanotubes, nanosheets and yolk-shell spheres for acetone sensing. Among them, 3D $ZnCo_2O_4$ yolk-shell spheres with multi-shelled characteristics displayed outstanding response owing to the promoted gas molecule accessibility, multi-shell morphology, decreased crystalline size and large specific surface area [134]. Li et al. reported hollow porous tube assembled $ZnCo_2O_4$ porous architectures (Fig. 6a and b) combined solvothermal strategy and post-annealing treatment. The end of the $ZnCo_2O_4$ hollow tube joined together to form a concentric micro-flower with a diameter of 10–20 μm while the cross-section diameter of the hollow tube is around 500–600 nm confirmed by FESEM and transmission electron microscopy (TEM), which contributes the high surface area (35.6 $m^2$/g). Thus the extremely stable sensing sensitivity and ultrafast response and recovery process were achieved as shown in Fig. 6c and d [130]. A porous hierarchical $ZnCo_2O_4$ microstructure which has a feature of micro-flower composed of abundant nanosheets (Fig. 6e and f) was performed by Li et al. The micro-flower $ZnCo_2O_4$ sensor exhibited prominently excellent ppm-level acetone response (32.32), low LOD (2.51 @ 50 ppb), ultrafast response and recovery time (2.6/8.8 s) and excellent long-term stability towards 100 ppm acetone at 200 °C as shown in Fig. 6g and h. The superior acetone sensing properties was based on the abundant transport gas channels, more active sites derived from higher specific surface area of 95.04 $m^2 \cdot g^{-1}$, massive triangular and polygonal cone hollow spaces in $ZnCo_2O_4$ micro-flower [133].

As its low cost and high efficiency, template synthesis method based on precursor pyrolysis is considered to be the most appropriate one for obtainting 3D hollow nanostructure and microstructure [177,178]. Thus, the self-sacrificing template method was applied to prepare $Co_3O_4$/$ZnCo_2O_4$ hollow nanostructure derived from MOF. Specifically, ZIF-67 was fabricated through aging processing of $Co(NO_3)_2$ and methanol solutiuon of 2-MeIM. As a template, ZIF-67 was added to obtain Co/Zn-ZIF@Co–Zn LDH while annealing is the last procedure to obtain $Co_3O_4$/$ZnCo_2O_4$ hollow nanostructure. The FESEM results displayed the $Co_3O_4$/$ZnCo_2O_4$ nanostructure owned the irregular rhombus decahedron morphology while the surface was kind of rough owing to the degradation of organic ligands. The excellent surface properties entitled $Co_3O_4$/$ZnCo_2O_4$ with an amplified target-receptor interface was attributed to the large BET surface area (83.9 $m^2$/g), rendering it a

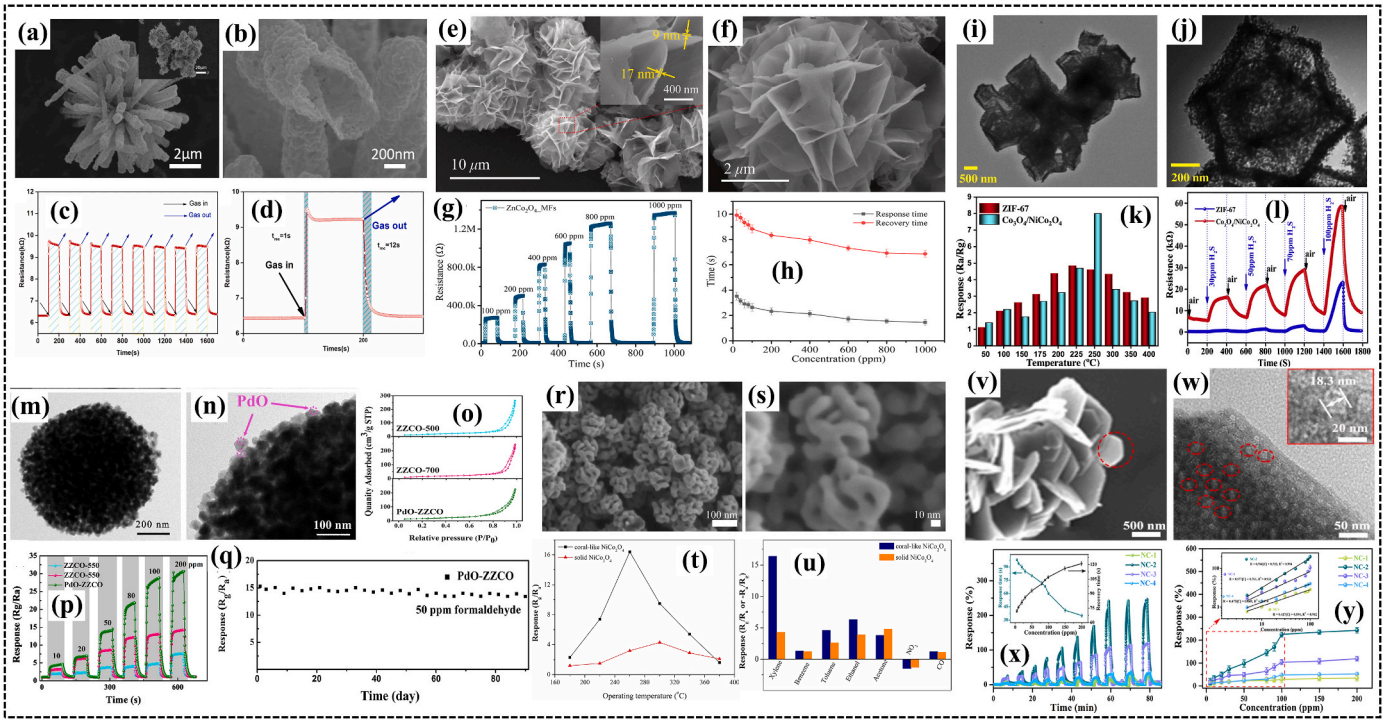


**Fig. 6.** (a) A typical FESEM image and (b) enlarged FESEM image of $ZnCo_2O_4$ hierarchical porous architectures (HPA). The inset is a low-magnification FESEM image of $ZnCo_2O_4$ HPA. (c) The $ZnCo_2O_4$ HPA sensor switches in the air and xylene atmosphere for eight cycles; (d) typical response and recovery behavior of $ZnCo_2O_4$ HPA to 200 ppm xylene at 260 °C. (Reproduced with permission from Ref. [130], Copyright© 2022, Elsevier). SEM images of (e) and (f): $ZnCo_2O_4$ microflowers (MFs). (g) Sensing curvess of the sensor based on $ZnCo_2O_4$ MFs to 100–1000 ppm acetone gas at 200 °C. (h) Response/recovery time of $ZnCo_2O_4$ MFs based sensor to acetone gas at concentration range of 20–1000 ppm. (Reproduced with permission from Ref. [133], Copyright© 2021, Elsevier). (i, j) TEM images of $Co_3O_4$/$NiCo_2O_4$ composite. Gas-sensing measurements: (k) Responses of ZIF-67 and $Co_3O_4$/$NiCo_2O_4$ to 50 ppm $H_2S$ at different operating temperatures, (l) response curves at 100 ppm for $H_2S$ at 30–100 ppm. (Reproduced with permission from Ref. [118], Copyright© 2020, Elsevier). TEM images (m, n) of PdO–ZnO/$ZnCo_2O_4$ microsperes. (o) $N_2$ adsorption-desorption isotherms of ZnO/$ZnCo_2O_4$-500 microsphere, ZnO/$ZnCo_2O_4$-700 microsphere and PdO–ZnO/$ZnCo_2O_4$ microsphere. (p) Dynamic response–recovery curves of the ZnO/$ZnCo_2O_4$-500, ZnO/$ZnCo_2O_4$-700 and PdO–ZnO/$ZnCo_2O_4$ MSs sensors to formaldehyde in the ranges of 10–200 ppm under 139 °C. (q) Long-term stability of the PdO–ZnO/$ZnCo_2O_4$ microsphere sensor to 50 ppm formaldehyde at 139 °C. (Reproduced with permission from Ref. [139], Copyright© 2020, Elsevier). (r) Low-magnification SEM image of the as-prepared, porous coral-like $NiCo_2O_4$ nanospheres, and (s) a representative SEM image of two samples of $NiCo_2O_4$ nanospheres. (t) Response of the sensors based on porous coral-like $NiCo_2O_4$ nanospheres and solid $NiCo_2O_4$ nanospheres to 100 ppm xylene. The response is plotted as a function of the operating temperature. (u) Response of the sensors based on porous coral-like $NiCo_2O_4$ nanospheres and solid $NiCo_2O_4$ nanospheres to 100 ppm of various gases at 260 °C, and 300 °C, respectively. (Reproduced with permission from Ref. [120], Copyright© 2018, Elsevier). (v) SEM and (w) TEM image of NC-2 (adding in 18 mmol 2-mIM). (x) Dynamic sensing transient curves under different concentrations (5, 10, 20, 30, 50, 80, 90, 100, 150, 200 ppm) n-butanol, inset is the response and recovery times of NC-2 sensors at different n-butanol concentrations. (y) Dot-line graph of concentration-dependent (5–200 ppm) response curves and the linear curves of concentration-dependent (5–100 ppm) response. (Reproduced with permission from Ref. [125], Copyright© 2020, Elsevier).

promising candidate material for gas detection [131]. The Ag/$ZnCo_2O_4$ microspheres combining self-template with annealing methods displayed superb formaldehyde sensing performance. The diameter of porous Ag/$ZnCo_2O_4$ microspheres assembled by massive nanoparticles ranged from 300 nm to 1 μm. The as-developed Ag/$ZnCo_2O_4$ sensors exhibited outstanding reponse of 11.18 which was better than pure $ZnCo_2O_4$ sensors towards 100 ppm formaldehyde at 99.3 °C. The enhanced sensing properties are derived from chemical sensitization and spillover effect. In detail, the reaction activation energy is reduced while oxygen species are prone to absorb on Ag nanoparticles which improved the formaldehyde sensitivity [132,179]. A novel double-shelled $Co_3O_4$/$NiCo_2O_4$ nanocage was synthesized by employing a template strategy. The as-developed products had a laminate nestlike shell which consists of massive nanosheets and the thickness of $NiCo_2O_4$ shell is about 100 nm while the thickness of internal $Co_3O_4$ shell is incommensurate as shown in Fig. 6i and j. The contrast experiment of sensing performance between ZIF-67 and $Co_3O_4$/$NiCo_2O_4$ was carried out. Owing to the hollow, penetrating and polyhedral nanostructure, high BET surface aera (103 $m^2$/g), low dissociation energy and high gas molecule entropy, the developed $Co_3O_4$/$NiCo_2O_4$ sensors have a better repsonse towards 30–100 ppm $H_2S$ as shown in Fig. 6k and l [118]. Koo et al. prepared Pd@ZnO/$ZnCo_2O_4$ hollow spheres on the basis of polystyrene sphere template and MOF mold methods. The Pd nanoparticles (2–3 nm) were loaded on the ZnO/$ZnCo_2O_4$ spheres with the diameter of 400 nm successfully. Outstanding response (69 % @ 5 ppm) towards acetone at 250 °C is revealed [138], which demonstrates that MOF-derived nanosized catalyst functionalized semiconductor oxide is a novel candidcate for fabricating superior performance chemoresistance gas sensor. A novel $ZnCo_2O_4$ superstructure with hollow polyhedral characteristic was obtained via a ZIF-67/ZIF-8 sacrificial template route. The as-developed $ZnCo_2O_4$ sensor possessed a response of 14.2–20 ppm ethanol with a rapid response/recovery process (22/62 s) at 200 °C while the LOD can reach 1 ppm. Furthermore, the $ZnCo_2O_4$ sensor still had a high response of 17.6 with good repeatability to 200 ppm ethanol at 95%RH condition [140]. Based on the same research idea, Zhang et al. synthesized solid PdO/ZnO/$ZnCo_2O_4$ microspheres (Fig. 6m and n) for formaldehyde detection. Based on the catalytic impact of PdO, large BET surface area (Fig. 6o) and massive active adsorption sites, the PdO/ZnO/$ZnCo_2O_4$ possessed the excellent response (26.9 @ 100 ppm), fast response/recovery time (9/14 s), prime selectivity and low LOD (0.2 ppm) at 139 °C as shown in Fig. 6p and q [139]. Kaneti et al. repoted a ZnO/$ZnCo_2O_4$ CO gas sensor with highly sensitivity and selectivity by template method. The hierarchical macroporous ZnO/$ZnCo_2O_4$ honeycomb shaped composites can be discerned. Unique macroporous structure constructed, high surface area, rapid electron transfer and stable p-n heterostructure synergistically improved the CO sensing properties [141].

Due to the high temperature stability, high electrical conductivity and excellent electrochemical properties, three-dimensional structure of $NiCo_2O_4$ is widely used in the preparation of high-performance gas sensors. For example, novel coral-like $NiCo_2O_4$ nanospheres with porous properties were synthesized by the group of Zhang et al. as shown in Fig. 6r and s. The coral-liked $NiCo_2O_4$ nanospheres with the diameter of 60–80 nm owns the BET surface area of 83.8 $m^2$/g. Towards 100 ppm xylene, the coral-liked $NiCo_2O_4$ nanospheres displayed better response (4 times) than solid $NiCo_2O_4$ samples at 260°C–300 °C while more superior selectivity property were shown in Fig. 6t and u [120]. Zhou et al. adopted PdO as a catalyst for synthesizing hollow NiO/$NiCo_2O_4$ nanocages with truncated feature by co-precipitation and etching-wet impregnation methods. The PdO–NiO/$NiCo_2O_4$ are hollow nanocubes with their interior expanding diagonally and 0D PdO nanoparticles are uniformly dispersed on their surface. With the deoppilant and porous nanostructure and catalytic action of PdO, PdO–NiO/$NiCo_2O_4$ truncated nanocage sensors exhibited the higher reponse of 6.7 towards 100 ppm acetone at 220 °C than NiO/$NiCo_2O_4$ solid nanocubes sensors [121]. The group of Hu et al. fabricated a highly sensitive nitrogen dioxide sensor employing $NiCo_2O_4$/$WO_3$ p-n heterostructure. From the SEM results, rectangular-shaped $WO_3$ nanoflake and flower-shaped $NiCo_2O_4$ microspheres stick tightly to each other [123]. Meanwhile, a novel hierarchical $NiCo_2O_4$ microsphere was obtained by regulating the calcination temperature (300 °C, 400 °C and 500 °C) through a facile hydrothermal strategy and the $NiCo_2O_4$ microspheres were assembled by massive nanorods [124]. In addition to the $NiCo_2O_4$ microsphere, Dang et al. synthesized $NiCo_2O_4$ microflower with hierarchical feature applying for n-butanol detection as shown in Fig. 6v-y. By regulating the amount of 2-methylimidazole in synthesis, the $NiCo_2O_4$ microflower with the optimal morphology (adding 18 mmol 2-methylimidazole) have possessed high BET surface area (62.465 $m^2$/g) and the numerous chemisorbed oxygen species of 58.78 %, while the corresponding gas sensor exhibited the high response of 240 %, fast response/recovery reaction (68/107 s) and brilliant long term stability [125]. The group of Zheng et al. reported a self-sacrificial template method to prepare $NiCo_2O_4$ spheres with different morphology by regulating the heating rate of calcination. The $NiCo_2O_4$ sample with a calcination rate of 10 °C/min had a double-shell hollow sphere structure while the diameter is 800–900 nm. Meanwhile, the gas sensor exhibited high sensitivity (23.3), fast response/recovery time (15.4/30.5 s) and excellent long-term stability towards 100 ppm xylene at the optimum operating temperature (240 °C). Compared with the single-shell hollow $NiCo_2O_4$ sphere and solid $NiCo_2O_4$ sphere, the better sensing performance is discerned. The higher specific surface area (93.5 $m^2$/g) and unique nanostructure are beneficial to gas molecule transportation and diffusion [126]. Zhang et al. reported a $NiCo_2O_4$/PANI self-powered sensor for $NH_3$ detection. The $NiCo_2O_4$ solid microspheres with smooth surface are coated with PANI nanorods. The $NiCo_2O_4$/PANI sensor configured with eco-friendly triboelectric nanogenerator had the better response of 4.67 towards 20 ppm $NH_3$ than previous sensors conducted by self-powered voltage, which is due to the p-p heterojunction predominantly modified the sensor resistance as a hole pump, thus improving the sensitivity [127,180].

A novel hollow $MCo_2O_4$ (M = Mn, Ni, and Zn) multishelled twin nanospheres for formaldehyde and acetone detection was repored recently. The morphology of all products is formed by the adhesion of two multishelled spheres with the diameter of 400–500 nm to each other. Compared with the $MnCo_2O_4$ and $NiCo_2O_4$ gas sensors, $ZnCo_2O_4$ gas sensor have better response towards formaldehyde (203 @ 50 ppm) and acetone (318 @ 50 ppm) at 170 °C and 190 °C, respectively, which is attributed to the higher $Co^{3+}$/$Co^{2+}$ ratio and larger chemisorbed oxygen content [36]. Above all, the current research trend is applying MOF as template or precursors to synthesize 3D $MCo_2O_4$ based material on the account of its large surface area and easily tuned morphology by choosing various organic bridging ligands and metal ions [181–184], which provides effective technology for constructing exquisite structure like porous carbon, SMOX and SMOX/MOFs composites [185]. Meanwhile, as two efficient surfactants, PVP and DMF can be assembled into aggregates in the bulk precursor solution, which is conducive to the formation of 3D $MCo_2O_4$ based materials. By thermally decomposing the core during the self-assembly process, where the polymer part is located at the center and the inorganic part is developed onto the external surface, diverse 3D hollow nanostructures $MCo_2O_4$ based materials can be obtained. It is worth noting that solvothermal, hydrothermal reaction and template strategy are the most efficient strategies for producing the products possessing the high crystallinity, well-defined pores and large specific area. In detail, sensitivity of $MCo_2O_4$ gas sensor can be further improved by modifying crystal shapes by changing the preparation parameters, including reaction temperature and duration, pH value, solvent type, precursor concentration and the utilizing of catalysts. The specific gas sensitivity enhancement mechanism will be discussed in the next section.

## 4. Enhanced sensing properties and mechanism of $MCo_2O_4$ based gas sensor

While the synthetic material controls its morphology, the gas-sensing material can be suitably optimized to further enhance its response performance. Under the circumstance of impedance gas sensors and the specific detection process, the signal of the $MCo_2O_4$ gas sensor is mostly shown by the resistance value, while the analysis of gas sensing mechanism mainly depends on hole accumulation layer model [186,187], bulk resistance regulation theory [188] and gas diffusion control theory [189]. So essentially the gas-sensing performance can be enhanced by improving the carrier transport between the multiple materials in heterostructures. The group of Xu et al. constructed the grain size effect model, which indicated that gas sensitivity increased remarkably as the diameter of the crystal (D) equivalent to or smaller than 2L (L refers to the depth of surface space charge layer) [190]. However, the undesired increment of resistance aggravates the complexities of signal processing, suggesting an under-functioning gas sensor, which is known as receptor-transducer mismatch. The phenomenon limits the full use of semiconductor nanocrystals in practical gas sensors [191]. Elemental doping, functionalization of noble metals, construction of heterojunctions and tuning of synthesis parameters can all effectively modulate the efficiency and mode of electron transportation, resulting in substantial changes in the resistance of sensing materials and avoiding the mismatch between receptor and transducer. Researchers are currently using a combination of these approaches to create synergistic effects to enhance sensing performance.

### 4.1. The enhanced sensing strategies for pure $MCo_2O_4$ gas sensors

The sensing mechanism of $MCo_2O_4$ gas sensor is on the basis of the variation of resistance on the material's surface. In detail, the primary carriers of p-type semiconductor are holes. Massive ionized oxygen species ($O^{2-}$, $O_2^-$ and $O^-$) will be generated through trapping electrons from the surface when the air comes in, which creates the insulation core with high resistance and generates hole accumulation phenomenon with high electrical conductivity. Assuming that the reducing gas injected into the chamber, the hole accumulation layer will assimilate electrons and the resistance will increase. After the stable resistance is acquired, pure air can be injected again for making the resistance back to baseline level [192–195]. Above all, one of the most widely recognized models of gas-sensing mechanisms, the adsorption and desorption model is obtained. It should be emphasized that the types of free oxygen species ($O^{2-}$, $O_2^-$ and $O^-$) are highly correlated with the working temperature and the specific relationship is shown in Eqs. (4)–(7) [196–198].

$$O_2\ (\text{free}) \rightarrow O_2\ (\text{adsorp}) \tag{4}$$

$$O_2\ (\text{adsorp}) + e^- \rightarrow O_2^-\ (< 150^oC) \tag{5}$$

$$O_2\ (\text{adsorp}) + 2e^- \rightarrow 2O^-\ (150^oC\text{-}400^oC) \tag{6}$$

$$O^-\ (\text{adsorp}) + e^- \rightarrow O^{2-}\ (> 400^oC) \tag{7}$$

For pure $MCo_2O_4$ gas sensors, numerous strategies were adopted to strengthen the gas sensing properties, including adjusting annealing temperature [109] or heating rate [126] and the pH of the precursor solution [113], changing the stoichiometric ratio [103], altering the amount of structure-directing agent [125] or surfactant agent [199], applying the novel template [94], etc.

For instance, Zhao et al. synthesized $NiCo_2O_4$ nanoplates by adjusting calcination temperature (300 °C, 500 °C, 700 °C). When the thermal treated temperature increases from 300 °C to 500 °C, the crystallinity of $NiCo_2O_4$ reaches maximum and the optimal sensitivity can be obtained. As the temperature rises further to 700 °C, a new phase NiO will appear, resulting in the impurity [109,200]. Furthermore, by changing the heating rate (5, 7, and 10 °C $min^{-1}$) in the synthesis of $NiCo_2O_4$ nanostructures, different $NiCo_2O_4$ morphology including the porous spheres, single-shelled and double-shelled hollow spheres can be obtained, respectively [126].

Adjusting the pH of the precursor is an effective way to changing the properties of sensing materials. By adding different amount of citric acid from 2.5 to 7.5 mmol, the grain size of $CuCo_2O_4$ samples prepared by Zhao et al. first decreased and increased later while the porosity is positively correlated with the amount of citric, which may attribute to the gas evolution and heat release in an acidic environment. In addition, too much citric acid added (7.5 mmol) will tend to form a secondary phase, resulting in impurity of sample [113]. Stoichiometric ratio regulation is determined to be a highly facile route to construct heterojunction and induce more oxygen vacancies. Gawande et al. regulated zinc and cobalt composition varying from 1 : 1 to 1 : 3 to obtain $ZnCo_2O_4$ nanoparticles, as the results demonstrated that certain sample (Zn: Co = 1 : 2.5) possessed the highest reducibility by temperature programmed reduction $H_2$ (TPR-$H_2$) spectra, indicating more available active sites, which benefited gas sensing properties a lot [103]. Adequate structure-directing agent will exert specific influence on the morphology of materials. By adding exactly-measured xylose which ownes the agglomeration effect on nanomaterials, the $NiCo_2O_4$, $MnCo_2O_4$ and $ZnCo_2O_4$ multi-shelled twin nanospheres were obtained while the enhanced sensing mechnism was finely illustrated as shown in Fig. 7a-d [36]. Furthermore, Zhang et al. modified the morphology and composition of $NiCo_2O_4$ by changing the content of the 2-methylimidomide, which is an effective ligand and structure-directing agent. As shown in Fig. 7e-f, too less 2-methylimidazole (12 mmol) used in synthesis process tends to form irregular hexagonal fragments which are scattered randomly while too much 2-methylimidazole (24, 36 mmol) will impede the growth of crystal and destroy the 3D flower-like structure. Only adding a certain amount of 2-methylimidazole (18 mmol) can lead to the appropriate degree of polymerization reaction driven by M − N bond (M = $Ni^{2+}$, $Co^{2+}$) (Fig. 7b) [125].

Through the research of Morán-Lázaro et al., the concentration of dodecylamine (5.4 mmol, 10.8 mmol, 16.2 mmol) exerts a significant effect on the nanostructure and particle diameter of $ZnCo_2O_4$ [201]. With the concentration of dodecylamine rose, the number of $ZnCo_2O_4$ nanoparticles gradually increased, while the size became smaller, indicating that dodecylamine inhibited the growth of $ZnCo_2O_4$ nanoparticles. The main functions of dodecylamine in synthesis are surfactant and agent reduction. As a reducing agent, the electrons of nitrogen can participate as a reducing agent to reduce cationic $Co^{2+}$ to metal nanoparticles $Co^0$ while the action of surfactants is mainly worked by electrostatic interaction [199,202].

### 4.2. Elemental doping (noble metal or other elements)

Noble metal doping generally contains the decoration of Ag [132,135] and Pd [91,138] on $MCo_2O_4$ semiconductor surfaces, which provides an efficient approach to improving sensitivity and lowering the operation temperature [203]. The superior sensing properties for gas sensors are ascribed to electronic and catalytic impact [204,205]. The functionalization of noble metal doping facilitating the sensing performance is primarily embodied in two ways: (1) modification of Ag and Pd effectively reduces the surface resistance of the material, therefore the lower working temperature detection can be achieved; (2) the load of Ag and Pd nanoparticles enlarges the specific surface area and improves the surface activity, therefore target gas has more contact area and faster reaction speed with the adsorbed oxygen energy onto the $MCo_2O_4$ semiconductor.

Except for doping precious metals, another effective strategy to improve gas sensitivity is to add heteroatomic doping of another metal. In detail, the grain sizes, porosity and specific surface area of the SMOX will change after metal heteroatoms are doped into the sensing material, the adsorption site and diffusion path of gas molecule can be optimized [206]. Furthermore, the facilitating of gas sensing properties by element

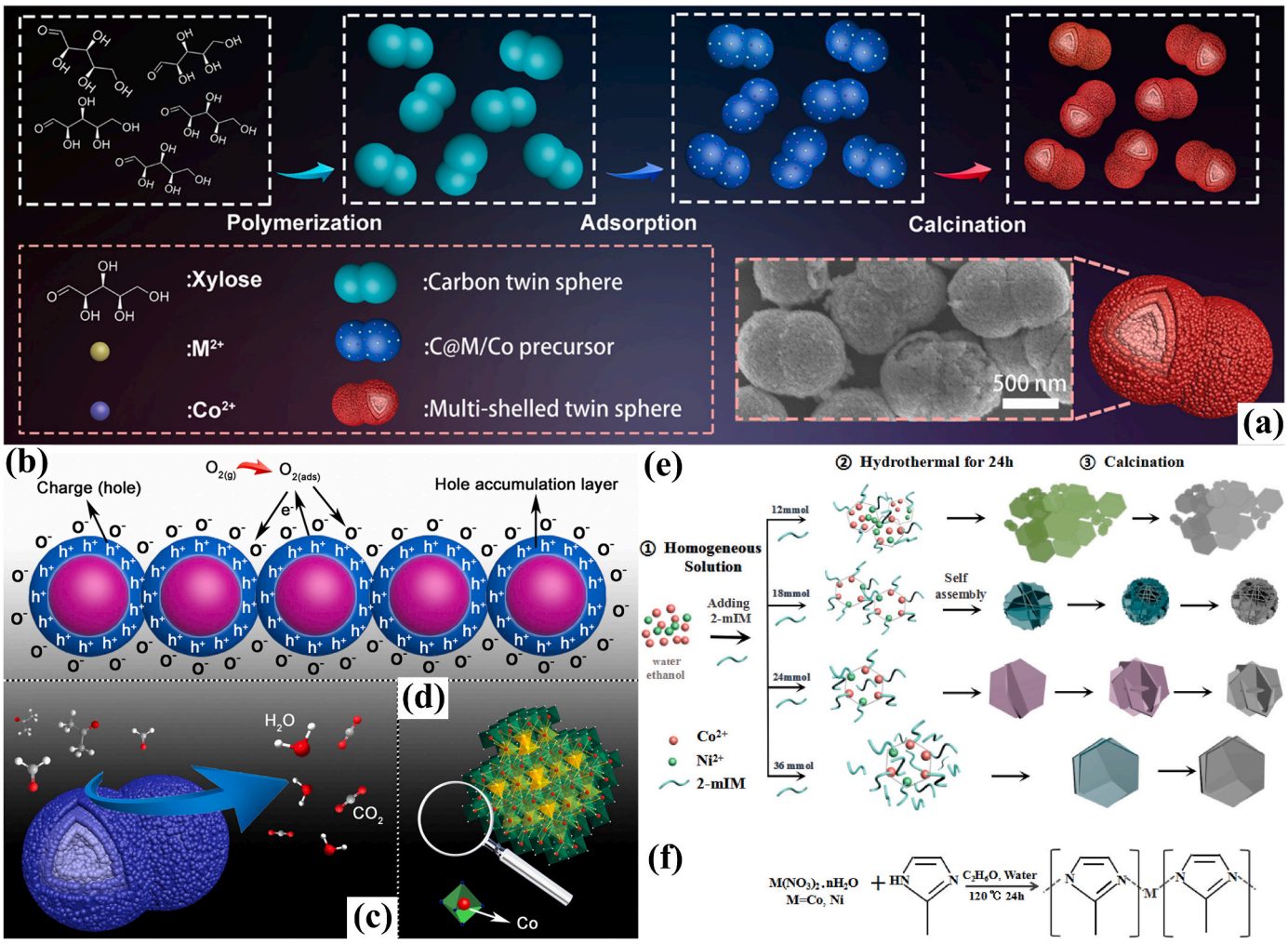


**Fig. 7.** (a) Synthetic process of $MCo_2O_4$ multi-shelled hollow twin spheres. (b–d) Schematic illustration of the sensing mechanism for sensors based on $ZnCo_2O_4$ materials. (Reproduced with permission from Ref. [36] Copyright© 2019, ACS Publications). (e) Synthetic mechanisms of samples with various amount of 2-methylimidomide and (f) Diagram of the formation process of M − N bond. (Reproduced with permission from Ref. [125], Copyright© 2020, Elsevier).

dopant other than noble metals is mainly reflected in increasing oxygen vacancy concentration and BET surface area, reducing the width of band gap, optimizing the electronic structure and maximizing band bending at the heterojunction interface. After doping 20 mol% of zinc to form $Ni_{0.8}Zn_{0.2}Co_2O_4$ nanorods, of which the sensing performance to $NO_x$ became better while the higher BET surface area and lower band gap are primary factors [96].

### 4.3. Developing heterojunctions

Heterojunction is a kind of physical and electronic junction between two or more disparate solid-state materials in nature. Fermi levels of the diverse materials connect to each other while different or same type of charge carriers will vigorously participate during sensing process. Specifically, silicon p-n heterojunctions are widely used in basic elements of diodes, LEDs, transistors and gas sensors [171]. For binary or trinary semiconductor gas sensors, the improved sensing properties and mechanism will change according to the types of constructed heterojunctions.

Based on the type of heterojunction, since $MCo_2O_4$ refers to a p-type semiconductor, there are many reports that p-n [37,85–87,95,98,101,102,105,106,110,123,129,137,139,141,207,208] and p-p [76,97,118,119,121,122,131] heterojunctions are constructed while other types of heterojunctions, including graphene [84], reduced graphene oxide [92,112], multi-walled carbon nanotubes [107], carbon cloth [115], g-$C_3N_4$ [81], polyaniline [127] and polypyrrole [77] are explored as well.

As shown in Fig. 8a, the carriers in the p-n heterojunction include free electrons and holes, which will both flow resulting from the differences in Fermi energy levels of two semiconductors, resulting in a faster carrier transport rate than p-p or n-n heterojunctions. Negative electrons will move from the conduction band of higher Fermi level to another which owns the lower one and the positive holes will transfer in the opposite direction. Finally, an electron depletion layer and a hole accumulation layer will construct at the interface of two materials.

Liu et al. established ZnO/$ZnCo_2O_4$ p-n heterostructure for ethylene glycol sensing enhancement. In detail, the electrons transferred from ZnO to $ZnCo_2O_4$ and the holes moved in an opposite direction as ZnO possessed the higher Fermi energy level. After the movement of carriers, the Fermi energy levels of two materials tend to coincide, while hole and electron depletion layers are formed. Meanwhile, inner self-established electric field was formed at the contact interface between $ZnCo_2O_4$ and ZnO, while the boundary barrier was established at the p-n interface and band bending in the semiconductor can be discerned [95]. Gas molecules will generate electrons to the p-n heterostructures when the sensing layer exposed to ethylene glycol, and rapid changes in electron concentration can greatly alter the thickness of the electron depletion layer, further enhancing the sensing performance as shown in Fig. 8c-f [87].

For p-p heterojunction according to Fig. 8b, holes act as charge carriers. As two p-type semiconductors contact with each other, holes will transfer out of the valence band until their Fermi levels are equal

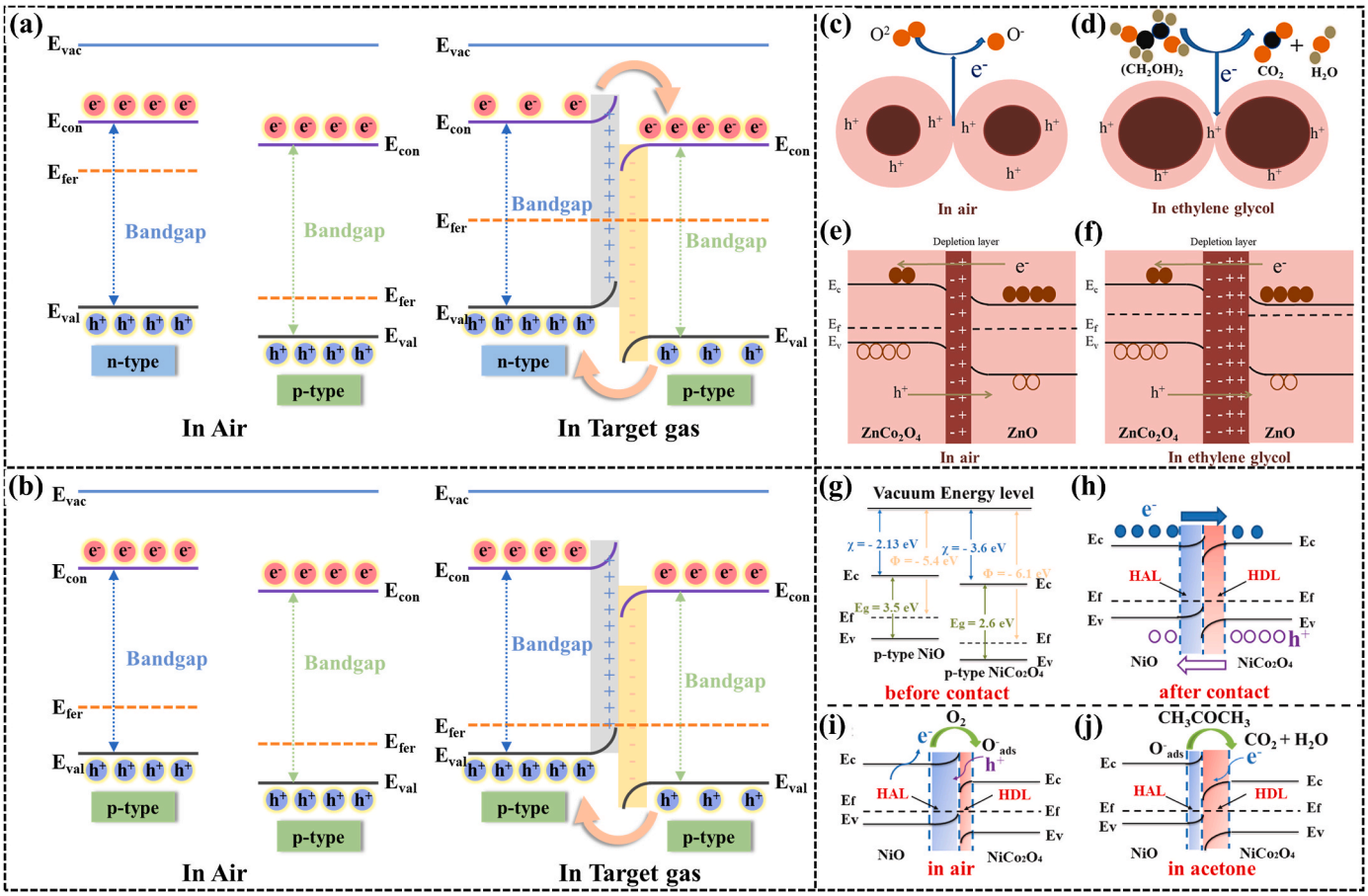


**Fig. 8.** Schematic diagrams of the energy bands based on (a) p-n heterojunction and (b) p-p heterojunction of $MCo_2O_4$ based SMOX. (c–f) The schematic illustration of possible gas-sensing mechanism for $ZnCo_2O_4$ and $ZnO/ZnCo_2O_4$. (Reproduced with permission from Ref. [87], Copyright© 2022, Elsevier). Schematic illustration of proposed gas sensing mechanism: (g, h) the energy band diagram of the NiO and $NiCo_2O_4$ before and after contact, respectively; (i, j) the energy band diagram of $NiO/NiCo_2O_4$ heterojunction expose to air and acetone, respectively. (Reproduced with permission from Ref. [76], Copyright© 2021, Elsevier).

due to their differences of Fermi energy level. Eventually, the absorbed holes will construct a layer of positively charged hole accumulation at the interface of two semiconductors. Meanwhile, a semiconductor that loses its holes will form a negatively charged hole depletion layer. Eventually, the constructed heterojunctions will efficaciously facilitate the accumulation of free electrons at the sensing surface layer, elevate the adsorption of oxygen molecules and increase the height of the energy barrier (Fig. 8g–j).

A novel $NiO/NiCo_2O_4$ p-p heterojunctions were prepared by Wang et al. for xylene detection. As the band gap width and work function of NiO are 3.5 eV and 5.4 eV while the corresponding value for $NiCo_2O_4$ is 2.6 eV and 6.1 eV, respectively [121], the free electrons will move from NiO to $NiCo_2O_4$ until the equal Fermi level is formed. Meanwhile, the hole accumulation layer and depletion layer will generate. Once the $NiO/NiCo_2O_4$ exposed to xylene, oxygen species will react with xylene molecules and motivate electrons back to the $NiO/NiCo_2O_4$, therefore tipping the dynamic carrier equilibrium between NiO and $NiCo_2O_4$, resulting in the decrease of hole accumulation layer [119].

Moreover, classification can be made based on whether $MCo_2O_4$ was material main body or appendages. As the $MCo_2O_4$ was served as a load recipient,In particular, graphene, as a representative 2D nanomaterial, has been extensively utilized in fabricating SMOX gas sensors for its excellent electronic properties (mobility of 15000 $cm^2\ V^{-1}\ s^{-1}$ under normal temperature and pressure), superior heat conductivity, high stability and ease of chemical functionalization [209]. Rathinavel et al. constructed $FeCo_2O_4$/graphene heterojunction, which owns the large BET surface area of 93.2 $m^2/g$, boosting the transportation of gas molecules, thus enhancing the efficiency of detection. Furthermore, the transitory retention of wave generated at the converted envelope-air interface when the target gas molecules interact with the graphene also plays a crucial role in promoting ethanol and acetone sensitivity [84]. Marimuthu et al. constructed a $FeCo_2O_4$/rGO nanostructures for $NH_3$ detection [92]. The hybridizing rGO triggering the active electrons migration between the sensing elements and the electrodes is a key to enhance sensing performance [210].

## 5. Issues and challenges

At present, based on the spinel type and special chemical structure of $MCo_2O_4$, it is widely used in gas detection which were listed in Tables 3 and 4. Beyond that, diverse types of $MCo_2O_4$ nanomaterials are also used in catalysis, energy storage and other fields as shown in Fig. 1a. Meanwhile, the $MCo_2O_4$ characteristics of low synthesis cost, strong structural stability, vibrant electrochemical performance and relative lower resistance, further ensure the effective detection of diverse toxic and explosive gases. Therefore, we intensively reviewed the morphology regulation and gas-sensitive enhancement of $MCo_2O_4$ in this paper. Although considerable progress has been achieved in the current development of $MCo_2O_4$ based gas sensors, numerous problems and challenges still need to be addressed to achieve high sensitivity, swift respond and recover process, outstanding selectivity and stability, especially in the future. In order to solve the current technical difficulties in this field, the following issues need to be further studied.

(1) Towards $MCo_2O_4$ sensors, they remain a huge challenge to detect target gas effectively in complicated gas environment due to the

intrinsic sensing mechanism of $MCo_2O_4$. For reasons of overcoming the disadvantage of poor selectivity in complex atmospheric environments, disparate $MCo_2O_4$ sensors can be integrated into a single array. Combing with the principal component analysis, linear discriminant analysis and other pattern recognition algorithms, the intelligent $MCo_2O_4$ sensor arrays can be utilized to deal with the experimental data to differentiate diverse gases [135].

(2) At present, another difficulty is that the power consumption of $MCo_2O_4$ gas sensors is too high (Table 4), mainly reflected in long recovery time and exorbitant working temperature. The construction of multiple composite materials is an effective approach to reducing the working temperature of the $MCo_2O_4$ sensor and improving the gas response value [84,107]. By further surmounting the limitations of elevated operating temperature on the fabrication and application of conventional devices, room temperature $MCo_2O_4$ sensor will implement satisfying strategies with lower power consumption, higher integrated density and superior precision.

(3) In general, a major challenge for $MCo_2O_4$ sensor research is the practical application. When using $MCo_2O_4$ sensor for agricultural product quality detection ($H_2S$, $NH_3$) [90,102], environmental monitoring (HCHO) [98], nondestructive disease detection (acetone) [77], the relative low sensitivity, insufficient stability and high operating temperature restrict the wearability, small size and low power consumption of $MCo_2O_4$ sensors in actual manufacturing. Therefore, in the future, efforts should be devoted to the development of more tolerant and environmentally recognizable components and nano-transducers of $MCo_2O_4$.

## 6. Conclusion and perspectives

Obviously, spinel type $MCo_2O_4$ based materials played a crucial role in the development of resistance-type and current-type sensors for inflammable and poisonous gases detection. The dimension and morphology regulation strategies of as-prepared material and coating technology were adopted to strengthen the sensing properties, especially the sensitivity and respond speed. In detail, researchers applied selecting elemental dopants, noble metal functionalization and heterojunction construction to promote the overall performance of $MCo_2O_4$ gas sensors. Wet chemical method, co-precipitation and self-templating methods are three common ways to prepare diverse $MCo_2O_4$ nanostructures. Different $MCo_2O_4$ nanostructures often represent diverse sensing properties while the sensing functional material which researchers desired should possess relatively large BET specific surface area, sufficient active adsorption sites and excellent physicochemical stability. $MCo_2O_4$ hollow nanospheres, nanoflowers and hierarchical structures are obtained by some research fellows which can supply high specific surface area and thus enhancing the gas sensors' stability.

With the low fabrication cost, automated manufacturing capabilities and an extensive range of the detected gases, we believe the room-temperature and subzero-temperature $MCo_2O_4$ sensors will dig up all-time chances for wafer-level fabrication and high-density integration of on-chip $MCo_2O_4$ sensor arrays. This will enable ubiquitous and credible machine olfaction capabilities beyond the human olfactory powers and further increase the practical application ability of $MCo_2O_4$ sensor. In addition, for reducing the operating temperature, diverse progressive materials including transition metal dichalcogenides, covalent organic framework and MXenes can be used to prepare $MCo_2O_4$ sensor. Based on the existing reports, the synthesis of $MCo_2O_4$ gas sensors by microwave hydrothermal method, combination of traditional hydrothermal and other deposition strategies should be further studied. Furthermore, on the basis of the unique advantage of high scalable and fast response rate, $MCo_2O_4$ based sensors provide a superb promise for promoting them with the flexible, wearable, self-powered, large-scale and low-cost feature, which will also be the focus of future research.

## CRediT authorship contribution statement

**Zichen Zheng:** Writing – review & editing, Writing – original draft, Methodology, Investigation, Data curation, Conceptualization. **Kewei Liu:** Writing – review & editing, Investigation. **Yiwen Zhou:** Writing – review & editing. **Zicong Zhang:** Writing – review & editing. **Hongyuan Su:** Writing – review & editing. **Xudong Nie:** Writing – review & editing. **Marc Debliquy:** Writing – review & editing, Supervision. **Zexin Yu:** Writing – review & editing. **Chao Zhang:** Writing – review & editing, Visualization, Validation, Supervision, Resources, Funding acquisition.

## Declaration of competing interest

The authors declare that they have no known competing financial interests or personal relationships that could have appeared to influence the work reported in this paper.

## Data availability

Data will be made available on request.

## Acknowledgments

This work was supported by the Outstanding Youth Foundation of Jiangsu Province of China (No. BK20211548), the Qinglan Project of Yangzhou University. and Graduate Research Innovation Program of Jiangsu Province of China (No. KYCX23_3551).

## References

[1] H. Wang, W.P. Lustig, J. Li, Sensing and capture of toxic and hazardous gases and vapors by metal-organic frameworks, Chem. Soc. Rev. 47 (2018) 4729–4756, https://doi.org/10.1039/C7CS00885F.

[2] Z. Li, H. Li, Z. Wu, M. Wang, J. Luo, H. Torun, P. Hu, C. Yang, M. Grundmann, X. Liu, Y. Fu, Advances in designs and mechanisms of semiconducting metal oxide nanostructures for high-precision gas sensors operated at room temperature, Mater. Horiz. 6 (2019) 470–506, https://doi.org/10.1039/C8MH01365A.

[3] Z. Xiao, L.B. Kong, S. Ruan, X. Li, S. Yu, X. Li, Y. Jiang, Z. Yao, S. Ye, C. Wang, T. Zhang, K. Zhou, S. Li, Recent development in nanocarbon materials for gas sensor applications, Sens. Actuators, B 274 (2018) 235–267, https://doi.org/10.1016/j.snb.2018.07.040.

[4] C. Dong, R. Zhao, L. Yao, Y. Ran, X. Zhang, Y. Wang, A review on $WO_3$ based gas sensors: morphology control and enhanced sensing properties, J. Alloys Compd. 820 (2020) 153194, https://doi.org/10.1016/j.jallcom.2019.153194.

[5] Z. Zheng, C. Zhang, K. Liu, Q. Liu, Volatile organic compounds, evaluation methods and processing properties for cooked rice flavor, Rice 15 (2022) 53, https://doi.org/10.1186/s12284-022-00602-3.

[6] K. Liu, Z. Zheng, J. Xu, C. Zhang, Enhanced visible light-excited $ZnSnO_3$ for room temperature ppm-level $CO_2$ detection, J. Alloys Compd. 907 (2022) 164440, https://doi.org/10.1016/j.jallcom.2022.164440.

[7] H.P. Li, J. Wen, S.M. Ding, J.B. Ding, Z.H. Song, C. Zhang, Z. Ge, X. Liu, R.Z. Zhao, F.C. Li, Synergistic coupling of 0D–2D heterostructure from ZnO and $Ti_3C_2T_x$ MXene-derived $TiO_2$ for boosted $NO_2$ detection at room temperature, Nano Mater. Sci. (2023), https://doi.org/10.1016/j.nanoms.2023.02.001.

[8] J.X. Lin, H.W. Hu, J. Luo, L. Miao, Z.H. Yang, M. Chen, M. Zhang, J.Z. Ou, Micro/nanoarrays and their applications in flexible sensors: a review, Mater, Today Nano 19 (2022) 100224, https://doi.org/10.1016/j.mtnano.2022.100224.

[9] N. Pradeep, T.s. Gopal, U. Venkatraman, T.A. Alrebdi, S. Pandiaraj, A. Alodhayb, M. Muthuramamoorthy, S.Y. Kim, Q.V. Le, S.H. Khan, A.C.J. Malathi, V. Raghavan, A.N. Grace, Effect of substrate bending towards chemiresistive based hydrogen gas sensor using ZnO-decorated MgO nanocubes, Mater. Today Chem. 26 (2022) 101200, https://doi.org/10.1016/j.mtchem.2022.101200.

[10] S. Cui, H. Pu, S.A. Wells, Z. Wen, S. Mao, J. Chang, M.C. Hersam, J. Chen, Ultrahigh sensitivity and layer-dependent sensing performance of phosphorene-based gas sensors, Nat. Commun. 6 (2015) 8632, https://doi.org/10.1038/ncomms9632.

[11] S. Li, Z. Ma, Z. Cao, L. Pan, Y. Shi, Advanced wearable microfluidic sensors for healthcare monitoring, Small 16 (2020) 1903822, https://doi.org/10.1002/smll.201903822.

[12] H. Nazemi, A. Joseph, J. Park, A. Emadi, Advanced micro- and nano-gas sensor technology: a review, Sensors 19 (2019) 1285, https://doi.org/10.3390/s19061285.

[13] W. Xuan, H. Shan, D. Hu, L. Zhu, T. Guan, Y. Zhao, Y. Qiang, J. Song, J. Zhang, M. Sui, X. Gu, S. Huang, In-situ synthesis of stable ZnO-coated $CsPbBr_3$ nanocrystals for room-temperature heptanal sensors, Mater. Today Chem. 26 (2022) 101155, https://doi.org/10.1016/j.mtchem.2022.101155.

[14] K. Liu, Z. Zheng, M. Debliquy, C. Zhang, Highly-sensitive volatile organic compounds evaluation by three-dimensional $ZnFe_2O_4$/$ZnSnO_3$ heterostructures and their predictive grain quality monitoring, Chem. Eng. J. 453 (2023) 139824, https://doi.org/10.1016/j.cej.2022.139824.

[15] Y. Qiu, Y. Wang, Morphology-controlled synthesis of $Co_9S_8$ nanotubes for ethanol gas sensors, Appl. Surf. Sci. 585 (2022) 152764, https://doi.org/10.1016/j.apsusc.2022.152764.

[16] Y.K. Moon, S.-Y. Jeong, Y.-M. Jo, Y.K. Jo, Y.C. Kang, J.-H. Lee, Highly selective detection of benzene and discrimination of volatile aromatic compounds using oxide chemiresistors with tunable Rh-$TiO_2$ catalytic overlayers, Adv. Sci. 8 (2021) 2004078, https://doi.org/10.1002/advs.202004078.

[17] Z. Zheng, K. Liu, K. Xu, C. Zhang, Investigation on microstructure and nonanal sensing properties of hierarchical $Sb_2WO_6$ microspheres, Ceram. Int. 48 (2022) 30249–30259, https://doi.org/10.1016/j.ceramint.2022.06.298.

[18] D. Wang, D. Zhang, Q. Pan, T. Wang, F. Chen, Gas sensing performance of carbon monoxide sensor based on rod-shaped tin diselenide/MOFs derived zinc oxide polyhedron at room temperature, Sens. Actuators, B 371 (2022) 132481, https://doi.org/10.1016/j.snb.2022.132481.

[19] N. Zhang, S. Ruan, F. Qu, Y. Yin, X. Li, S. Wen, S. Adimi, J. Yin, Metal–organic framework-derived $Co_3O_4$/$CoFe_2O_4$ double-shelled nanocubes for selective detection of sub-ppm-level formaldehyde, Sens. Actuators, B 298 (2019) 126887, https://doi.org/10.1016/j.snb.2019.126887.

[20] S. Bai, Y. Tian, Y. Zhao, H. Fu, P. Tang, R. Luo, D. Li, A. Chen, C.C. Liu, Construction of NiO@$ZnSnO_3$ hierarchical microspheres decorated with NiO nanosheets for formaldehyde sensing, Sens. Actuators, B 259 (2018) 908–916, https://doi.org/10.1016/j.snb.2017.10.176.

[21] H. Li, S. Chu, Q. Ma, J. Wang, Q. Che, G. Wang, P. Yang, Hierarchical $WO_3$/$ZnWO_4$ 1D fibrous heterostructures with tunable in-situ growth of $WO_3$ nanoparticles on surface for efficient low concentration HCHO detection, Sens. Actuators, B 286 (2019) 564–574, https://doi.org/10.1016/j.snb.2019.02.028.

[22] Y. Xu, X. Tian, Y. Fan, Y. Sun, A formaldehyde gas sensor with improved gas response and sub-ppm level detection limit based on NiO/$NiFe_2O_4$ composite nanotetrahedrons, Sens. Actuators, B 309 (2020) 127719, https://doi.org/10.1016/j.snb.2020.127719.

[23] M.P. Chen, Y.M. Zhang, J. Zhang, K.J. Li, T.P. Lv, K.Y. Shen, Z.Q. Zhu, Q.J. Liu, Facile lotus-leaf-templated synthesis and enhanced xylene gas sensing properties of Ag-$LaFeO_3$ nanoparticles, J. Mater. Chem. C 6 (2018) 6138–6145, https://doi.org/10.1039/c8tc01402g.

[24] H.E. Lee, Z.J.A. Mercer, S.M. Ng, M. Shafiei, H.S. Chua, Geo-tracing of black pepper using metal oxide semiconductor (MOS) gas sensors array, IEEE Sensor. J. 20 (2020) 8039–8045, https://doi.org/10.1109/JSEN.2020.2981602.

[25] C.M. Lou, G.L. Lei, X.H. Liu, J.Y. Xie, Z.S. Li, W. Zheng, N. Goel, M. Kumar, J. Zhang, Design and optimization strategies of metal oxide semiconductor nanostructures for advanced formaldehyde sensors, Coord. Chem. Rev. 452 (2022) 214280, https://doi.org/10.1016/j.ccr.2021.214280.

[26] M.S. Yao, L.A. Cao, Y.X. Tang, G.E. Wang, R.H. Liu, P.N. Kumar, G.D. Wu, W. H. Deng, W.J. Hong, G. Xu, Gas transport regulation in a MO/MOF interface for enhanced selective gas detection, J. Mater. Chem. A 7 (2019) 18397–18403, https://doi.org/10.1039/c9ta05226g.

[27] X.Y. Li, G.T. Sun, F. Fan, Y.Y. Li, Q.C. Liu, H.C. Yao, Z.J. Li, Au-25 nanoclusters incorporating three-dimensionally ordered macroporous $In_2O_3$ for highly sensitive and selective formaldehyde sensing, ACS Appl. Mater. Interfaces 14 (2022) 564–573, https://doi.org/10.1021/acsami.1c16552.

[28] X. He, H. Chai, Y. Luo, L. Min, M. Debliquy, C. Zhang, Metal oxide semiconductor gas sensing materials for early lung cancer diagnosis, J. Adv. Ceram. 12 (2023) 207–227, https://doi.org/10.26599/JAC.2023.9220694.

[29] J.Q. Gu, B. Zhang, Y.W. Li, X.T. Xu, G. Sun, J.L. Cao, Y. Wang, Synthesis of spindle-like Co-doped $LaFeO_3$ porous microstructure for high performance n-butanol sensor, Sens. Actuators, B 343 (2021) 130125, https://doi.org/10.1016/j.snb.2021.130125.

[30] H.G. Yakubu, Z. Kovacs, T. Toth, G. Bazar, Trends in artificial aroma sensing by means of electronic nose technologies to advance dairy production - a review, Crit. Rev. Food Sci. Nutr. 63 (2022) 234–248, https://doi.org/10.1080/10408398.2021.1945533.

[31] Z. Zheng, C. Zhang, Electronic noses based on metal oxide semiconductor sensors for detecting crop diseases and insect pests, Comput. Electron. Agric. 197 (2022) 106988, https://doi.org/10.1016/j.compag.2022.106988.

[32] H. Kang, S.Y. Cho, J. Ryu, J. Choi, H. Ahn, H. Joo, H.T. Jung, Multiarray nanopattern electronic nose (E-Nose) by high-resolution top-down nanolithography, Adv. Funct. Mater. 30 (2020) 2002486, https://doi.org/10.1002/adfm.202002486.

[33] A. Šutka, K.A. Gross, Spinel ferrite oxide semiconductor gas sensors, Sens. Actuators, B 222 (2016) 95–105, https://doi.org/10.1016/j.snb.2015.08.027.

[34] D.S. Mathew, R.-S. Juang, An overview of the structure and magnetism of spinel ferrite nanoparticles and their synthesis in microemulsions, Chem. Eng. J. 129 (2007) 51–65, https://doi.org/10.1016/j.cej.2006.11.001.

[35] J.S. Kim, B. Kim, H. Kim, K. Kang, Recent progress on multimetal oxide catalysts for the oxygen evolution reaction, Adv. Energy Mater. 8 (2018) 1702774, https://doi.org/10.1002/aenm.201702774.

[36] T. Zhou, S. Cao, R. Zhang, J. Tu, T. Fei, T. Zhang, Effect of cation substitution on the gas-sensing performances of ternary spinel $MCo_2O_4$ (M = Mn, Ni, and Zn) multishelled hollow twin spheres, ACS Appl. Mater. Interfaces 11 (2019) 28023–28032, https://doi.org/10.1021/acsami.9b07546.

[37] A. Akhtar, W. Di, J. Liu, C. Fu, J. Wang, X. Chu, The detection of ethanol vapors based on a p-type gas sensor fabricated from heterojunction $MoS_2$–$NiCo_2O_4$, Mater. Chem. Phys. 282 (2022) 125964, https://doi.org/10.1016/j.matchemphys.2022.125964.

[38] X. Hou, S. Bai, S. Xue, X. Shang, Y. Fu, D. He, Wrinkled-paper-like $ZnCo_2O_4$ nanoflakes as a superior anode material for ultrahigh-rate lithium-ion batteries, J. Alloys Compd. 711 (2017) 592–597, https://doi.org/10.1016/j.jallcom.2017.04.062.

[39] Q. Wang, X. Wang, B. Liu, G. Yu, X. Hou, D. Chen, G. Shen, $NiCo_2O_4$ nanowire arrays supported on Ni foam for high-performance flexible all-solid-state supercapacitors, J. Mater. Chem. A 1 (2013) 2468–2473, https://doi.org/10.1039/C2TA01283A.

[40] H. Gao, Y. Cao, Y. Chen, Z. Liu, M. Guo, S. Ding, J. Tu, J. Qi, Ultrathin NiFe-layered double hydroxide decorated $NiCo_2O_4$ arrays with enhanced performance for supercapacitors, Appl. Surf. Sci. 465 (2019) 929–936, https://doi.org/10.1016/j.apsusc.2018.09.180.

[41] J.P. Cheng, W.D. Wang, X.C. Wang, F. Liu, Recent research of core–shell structured composites with $NiCo_2O_4$ as scaffolds for electrochemical capacitors, Chem. Eng. J. 393 (2020) 124747, https://doi.org/10.1016/j.cej.2020.124747.

[42] J.M. Gonçalves, M.N.T. Silva, K.K. Naik, P.R. Martins, D.P. Rocha, E. Nossol, R.A. A. Munoz, L. Angnes, C.S. Rout, Multifunctional spinel $MnCo_2O_4$ based materials for energy storage and conversion: a review on emerging trends, recent developments and future perspectives, J. Mater. Chem. A 9 (2021) 3095–3124, https://doi.org/10.1039/D0TA11129E.

[43] C. Lu, R. Deng, R. Xu, Y. Zhao, X. Zhu, Y. Wei, K. Li, Design of hybrid oxygen carriers with $CeO_2$ particles on $MnCo_2O_4$ microspheres for chemical looping combustion, Chem. Eng. J. 404 (2021) 126554, https://doi.org/10.1016/j.cej.2020.126554.

[44] C. Koventhan, V. Vinothkumar, S.-M. Chen, P. Veerakumar, K.-C. Lin, Polyol-assisted synthesis of spinel-type magnesium cobalt oxide nanochains for voltammetric determination of the antipsychotic drug thioridazine, J. Electroanal. Chem. 898 (2021) 115600, https://doi.org/10.1016/j.jelechem.2021.115600.

[45] J. Niu, H. Liu, Y. Zhang, X. Wang, J. Han, Z. Yue, E. Duan, $NiCo_2O_4$ spinel for efficient toluene oxidation: the effect of crystal plane and solvent, Chemosphere 259 (2020) 127427, https://doi.org/10.1016/j.chemosphere.2020.127427.

[46] R. Yang, X. Bai, X. Guo, K. Song, L. Jia, X. Chen, J. Wang, Hierarchical $NiCo_2O_4$ nanostructured arrays decorated over the porous Ni/C as battery-type electrodes for supercapacitors, Appl. Surf. Sci. 586 (2022) 152574, https://doi.org/10.1016/j.apsusc.2022.152574.

[47] Y. Zhang, D. Sun, Y. Wang, X. Liu, H. Sun, T. Cai, X. Li, H. Hu, X. Zhang, W. Xing, Z. Yan, Facile electrochemically induced vacancy modulation of $NiCo_2O_4$ cathode toward high-performance aqueous Zn-based battery, Chem. Eng. J. 453 (2023) 139736, https://doi.org/10.1016/j.cej.2022.139736.

[48] Z. Zhang, X. Liu, D. Wang, H. Wan, Y. Zhang, G. Chen, N. Zhang, R. Ma, Ruthenium composited $NiCo_2O_4$ spinel nanocones with oxygen vacancies as a high-efficient bifunctional catalyst for overall water splitting, Chem. Eng. J. 446 (2022) 137037, https://doi.org/10.1016/j.cej.2022.137037.

[49] X. Luo, Q. Zhou, M. Guo, X. Peng, D. Wu, Y. Ito, Y. Liu, Multiple structural defects in poor-crystalline In-doped $NiCo_2O_4$ nanoneedles synergistically and remarkably enhance supercapacitive performance, Chem. Eng. J. 431 (2022) 134220, https://doi.org/10.1016/j.cej.2021.134220.

[50] Q. Wu, Y. Zhao, J. Yu, D. Song, R. Chen, Q. Liu, R. Li, M. Fan, Controlled growth of hierarchical $FeCo_2O_4$ ultrathin nanosheets and $Co_3O_4$ nanowires on nickle foam for supercapacitors, Int. J. Hydrogen Energy 44 (2019) 31780–31789, https://doi.org/10.1016/j.ijhydene.2019.10.119.

[51] F. Dong, X. Liu, M. Irfan, L. Yang, S. Li, J. Ding, Y. Li, I.U. Khan, P. Zhang, Macaroon-like $FeCo_2O_4$ modified activated carbon anode for enhancing power generation in direct glucose fuel cell, Int. J. Hydrogen Energy 44 (2019) 8178–8187, https://doi.org/10.1016/j.ijhydene.2019.02.031.

[52] D. Yin, H. Yang, S. Wang, Z. Yang, Q. Liu, X. Zhang, X. Zhang, Ce-doped $ZnCo_2O_4$ nanospheres: synthesis, double enzyme-like performances, catalytic mechanism and fast colorimetric determination for glutathione, Colloids Surf., A 607 (2020) 125466, https://doi.org/10.1016/j.colsurfa.2020.125466.

[53] J. Wang, B. Wang, A. Feng, Z. Jia, G. Wu, Design of morphology-controlled and excellent electromagnetic wave absorption performance of sheet-shaped $ZnCo_2O_4$ with a special arrangement, J. Alloys Compd. 834 (2020) 155092, https://doi.org/10.1016/j.jallcom.2020.155092.

[54] Y. Zhang, Z. Tan, X. Wang, Y. Zhan, Y. Xiao, C. Au, L. Jiang, Facile fabrication of Ce-decorated composition-tunable Ce@$ZnCo_2O_4$ core–shell microspheres for enhanced catalytic propane combustion, Nanoscale 11 (2019) 4794–4802, https://doi.org/10.1039/c8nr10523e.

[55] M. Amiri, H. Mahmoudi-Moghaddam, Green synthesis of ZnO/$ZnCo_2O_4$ and its application for electrochemical determination of bisphenol A, Microchem. J. 160 (2021) 105663, https://doi.org/10.1016/j.microc.2020.105663.

[56] D.S. Kim, I.K. Moon, J.H. Yang, K. Choi, J. Oh, S.W. Kim, Mesoporous $ZnCo_2O_4$ nanowire arrays with oxygen vacancies and N-dopants for significant improvement of non-enzymatic glucose detection, J. Electroanal. Chem. 878 (2020) 114585, https://doi.org/10.1016/j.jelechem.2020.114585.

[57] C. Ding, W. Xu, M. Wang, X. Zeng, W. Wang, Microstructure controlled $ZnCo_2O_4$/C microhydrangea nanocomposites as highly reliable anodes for lithium-ion batteries, Int. J. Energy Res. 44 (2019) 977–987, https://doi.org/10.1002/er.4956.

[58] T. Li, K. Xi, P.Y. Jiang, Q.R. Pan, Y. Feng, H. Wu, Mixed Co-Mn spinel oxides based electrocatalysts for amperometric determination of hydrogen peroxide, ChemistrySelect 7 (2022) e202200631, https://doi.org/10.1002/slct.202200631.

[59] A.J. Jesu Amalraj, U. N, S.-F. Wang, Rational design of platinum assimilated 3-D zinc cobalt oxide flowers for the electrochemical detection of caffeine in beverage

and energy drink, J. Ind. Eng. Chem. 106 (2022) 205–213, https://doi.org/10.1016/j.jiec.2021.10.026.
[60] J. Dong, L. Wen, H. Liu, H. Yang, J. Zhao, X. Luo, C. Hou, D. Huo, Simultaneous detection of dihydroxybenzene isomers in the environment by a free-standing flexible $ZnCo_2O_4$ nanoplate arrays/carbon fiber cloth electrode, Sci. Total Environ. 855 (2023) 158878, https://doi.org/10.1016/j.scitotenv.2022.158878.
[61] L. Merabet, K. Rida, N. Boukmouche, Sol-gel synthesis, characterization, and supercapacitor applications of $MCo_2O_4$ (M = Ni, Mn, Cu, Zn) cobaltite spinels, Ceram. Int. 44 (2018) 11265–11273, https://doi.org/10.1016/j.ceramint.2018.03.171.
[62] J. Wang, B. Wang, Z. Wang, L. Chen, C. Gao, B. Xu, Z. Jia, G. Wu, Synthesis of 3D flower-like $ZnO/ZnCo_2O_4$ composites with the heterogeneous interface for excellent electromagnetic wave absorption properties, J. Colloid Interface Sci. 586 (2021) 479–490, https://doi.org/10.1016/j.jcis.2020.10.111.
[63] R. Malik, V.K. Tomer, Y.K. Mishra, L. Lin, Functional gas sensing nanomaterials: a panoramic view, Appl. Phys. Rev. 7 (2020) 021301, https://doi.org/10.1063/1.5123479.
[64] J. Zhang, S. Cui, Y. Ding, X. Yang, K. Guo, J.-T. Zhao, Two-dimensional mesoporous $ZnCo_2O_4$ nanosheets as a novel electrocatalyst for detection of o-nitrophenol and p-nitrophenol, Biosens. Bioelectron. 112 (2018) 177–185, https://doi.org/10.1016/j.bios.2018.03.021.
[65] H. Ji, W. Zeng, Y. Li, Gas sensing mechanisms of metal oxide semiconductors: a focus review, Nanoscale 11 (2019) 22664–22684, https://doi.org/10.1039/c9nr07699a.
[66] H. Hou, G. Shao, W. Yang, W.-Y. Wong, One-dimensional mesoporous inorganic nanostructures and their applications in energy, sensor, catalysis and adsorption, Prog. Mater. Sci. 113 (2020) 100671, https://doi.org/10.1016/j.pmatsci.2020.100671.
[67] H. Wang, J. Ma, J. Zhang, Y. Feng, M.T. Vijjapu, S. Yuvaraja, S.G. Surya, K. N. Salama, C. Dong, Y. Wang, Q. Kuang, Z.P. Tshabalala, D.E. Motaung, X. Liu, J. Yang, H. Fu, X. Yang, X. An, S. Zhou, B. Zi, Q. Liu, M. Urso, B. Zhang, A. A. Akande, A.K. Prasad, C.M. Hung, N. Van Duy, N.D. Hoa, K. Wu, C. Zhang, R. Kumar, M. Kumar, Y. Kim, J. Wu, Z. Wu, X. Yang, S.A. Vanalakar, J. Luo, H. Kan, M. Li, H.W. Jang, M.O. Orlandi, A. Mirzaei, H.W. Kim, S.S. Kim, A.S.M. I. Uddin, J. Wang, Y. Xia, C. Wongchoosuk, A. Nag, S. Mukhopadhyay, N. Saxena, P. Kumar, J.-S. Do, J.-H. Lee, S. Hong, Y. Jeong, G. Jung, W. Shin, J. Park, M. Bruzzi, C. Zhu, R.E. Gerald, J. Huang, Gas sensing materials roadmap, J. Phys.-Condens Mat. 33 (2021), https://doi.org/10.1088/1361-648X/abf477.
[68] A.V. Nikam, B.L.V. Prasad, A.A. Kulkarni, Wet chemical synthesis of metal oxide nanoparticles: a review, CrystEngComm 20 (2018) 5091–5107, https://doi.org/10.1039/C8CE00487K.
[69] J. Chen, Q. Ma, X.-J. Wu, L. Li, J. Liu, H. Zhang, Wet-chemical synthesis and applications of semiconductor nanomaterial-based epitaxial heterostructures, Nano-Micro Lett. 11 (2019) 86, https://doi.org/10.1007/s40820-019-0317-6.
[70] W. Shi, S. Song, H. Zhang, Hydrothermal synthetic strategies of inorganic semiconducting nanostructures, Chem. Soc. Rev. 42 (2013) 5714–5743, https://doi.org/10.1039/C3CS60012B.
[71] I. Constantinoiu, C. Viespe, Synthesis methods of obtaining materials for hydrogen sensors, Sensors 21 (2021) 5758, https://doi.org/10.3390/s21175758.
[72] K. Ravichandran, P.K. Praseetha, T. Arun, S. Gobalakrishnan, Chapter 6 - synthesis of nanocomposites, in: S. Mohan Bhagyaraj, O.S. Oluwafemi, N. Kalarikkal, S. Thomas (Eds.), Synthesis of Inorganic Nanomaterials, Woodhead Publishing, 2018, pp. 141–168.
[73] A.V. Rane, K. Kanny, V.K. Abitha, S. Thomas, Chapter 5 - methods for synthesis of nanoparticles and fabrication of nanocomposites, in: S. Mohan Bhagyaraj, O. S. Oluwafemi, N. Kalarikkal, S. Thomas (Eds.), Synthesis of Inorganic Nanomaterials, Woodhead Publishing, 2018, pp. 121–139.
[74] C. Hu, L. Yu, S. Li, M. Yin, H. Du, H. Li, Sacrificial template triggered to synthesize hollow nanosheet-assembled $Co_3O_4$ microtubes for fast triethylamine detection, Sens. Actuators, B 355 (2022) 131246, https://doi.org/10.1016/j.snb.2021.131246.
[75] B. Feng, Y. Feng, Y. Li, Y. Su, Y. Deng, J. Wei, Synthesis of mesoporous $Ag_2O/SnO_2$ nanospheres for selective sensing of formaldehyde at a low working temperature, ACS Sens. 7 (2022) 3963–3972, https://doi.org/10.1021/acssensors.2c02232.
[76] Q. Chen, Y. Zhang, S. Ma, Y. Wang, P. Wang, G. Zhang, D. Gengzang, H. Jiao, M. Wang, W. Chen, Multishelled $NiO/NiCo_2O_4$ hollow microspheres derived from bimetal-organic frameworks as high-performance sensing material for acetone detection, J. Hazard Mater. 415 (2021) 125662, https://doi.org/10.1016/j.jhazmat.2021.125662.
[77] S.R. Ananda, L. Kumari, M.V. Murugendrappa, Studies on room-temperature acetone sensing properties of $ZnCo_2O_4$/PPy and $MnCo_2O_4$/PPy nanocomposites for diabetes diagnosis, Appl. Phys. A: Mater. Sci. Process. 128 (2022) 669, https://doi.org/10.1007/s00339-022-05792-7.
[78] S. Vadivel, G. Balaji, S. Rathinavel, High performance ethanol and acetone gas sensor based nanocrystalline $MnCo_2O_4$ using clad-modified fiber optic gas sensor, Opt. Mater. 85 (2018) 267–274, https://doi.org/10.1016/j.optmat.2018.08.067.
[79] J.P. Morán-Lázaro, F. López-Urías, E. Muñoz-Sandoval, M. Courel-Piedrahita, A. Carreon-Alvarez, V.M. Rodríguez-Betancourtt, I. Zamudio-Torres, E.S. Guillén-López, A. Palafox-Corona, Evaluation of $MgCo_2O_4$ nanoparticles as a gas sensor for the detection of acetone in the diabetic and non-diabetic range, Electron. Mater. Lett. 19 (2022) 66–75, https://doi.org/10.1007/s13391-022-00371-7.
[80] S.A. Vladimirova, K.Y. Prikhodko, M.N. Rumyantseva, E.A. Konstantinova, A. S. Chizhov, N.O. Khmelevsky, A.M. Gaskov, Nanocrystalline complex oxides $Ni_xCo_{3-x}O_4$: cations distribution impact on electrical and gas sensor behaviour, J. Alloys Compd. 828 (2020) 154420, https://doi.org/10.1016/j.jallcom.2020.154420.
[81] A. Akhtar, S. Sadaf, J. Liu, Y. Wang, H. Wei, Q. Zhang, C. Fu, J. Wang, Hydrothermally synthesized spherical $g\text{-}C_3N_4\text{-}NiCo_2O_4$ nanocomposites for ppb level ethanol detection, J. Alloys Compd. 911 (2022) 165048, https://doi.org/10.1016/j.jallcom.2022.165048.
[82] L. Yang, C. Wu, Y. Zhang, B. Xiao, A. Jiao, K. Li, T. Chen, R. Zhan, H. Lin, Enhancement of ammonia sensors using $In_2O_3$ sensing electrode by adjusting particle size and $NiCo_2O_4$ reference electrode, J. Electrochem. Soc. 169 (2022) 087505, https://doi.org/10.1149/1945-7111/ac83f4.
[83] G. Balaji, S. Rathinavel, S. Vadivel, Design and fabrication of clad removed fiber optic based $NiCo_2O_4$ sensor for detection of ethanol and acetone gases, Optik 228 (2021) 166216, https://doi.org/10.1016/j.ijleo.2020.166216.
[84] S. Rathinavel, G. Balaji, S. Vadivel, High performance ethanol and acetone gas sensing behavior of $FeCo_2O_4$/graphene hybrid sensors prepared by facile hydrothermal route, Optik 223 (2020) 165571, https://doi.org/10.1016/j.ijleo.2020.165571.
[85] Z. Yuan, Y. Lei, X. Li, F. Meng, H. Gao, $WO_3$ nanosheets/$FeCo_2O_4$ nanoparticles heterostructures for highly sensitive and selective ammonia sensors, IEEE Sensor. J. 21 (2021) 26515–26525, https://doi.org/10.1109/jsen.2021.3121688.
[86] H. Qin, T. Liu, J. Liu, Q. Liu, R. Li, H. Zhang, J. Wang, Fabrication of uniform 1-D $ZnO/ZnCo_2O_4$ nano-composite and enhanced properties in gas sensing detection, Mater. Chem. Phys. 228 (2019) 66–74, https://doi.org/10.1016/j.matchemphys.2019.02.051.
[87] M.M. Liu, S.Y. Ma, Y.H. Cai, N.N. Ma, L. Wang, H. Sheng, $ZnO/ZnCo_2O_4$ composite prepared by one-step hydrothermal method for high-performance ethylene glycol sensor, Ceram. Int. 48 (2022) 22305–22312, https://doi.org/10.1016/j.ceramint.2022.04.235.
[88] S. Vijayanand, P.A. Joy, H.S. Potdar, D. Patil, P. Patil, Nanostructured spinet $ZnCo_2O_4$ for the detection of LPG, Sens. Actuators, B 152 (2011) 121–129, https://doi.org/10.1016/j.snb.2010.09.001.
[89] Y. Tao, W. Zeng, ZIF-67 MOF-derived $Co_3O_4/NiCo_2O_4$/CC unique layered structure with excellent gas performances, Ceram. Int. 47 (2021) 8441–8446, https://doi.org/10.1016/j.ceramint.2020.11.209.
[90] J. Wu, Y. Yang, H. Yu, X. Dong, T. Wang, Ultra-efficient room-temperature $H_2S$ gas sensor based on $NiCo_2O_4$/r-GO nanocomposites, New J. Chem. 43 (2019) 10501–10508, https://doi.org/10.1039/c9nj01094g.
[91] S.-H. Kim, K.-S. Yun, Room-temperature hydrogen gas sensor composed of palladium thin film deposited on $NiCo_2O_4$ nanoneedle forest, Sens. Actuators, B 376 (2023) 132958, https://doi.org/10.1016/j.snb.2022.132958.
[92] G. Marimuthu, G. Palanisamy, T. Pazhanivel, G. Bharathi, K.P. Tiruppathi, D. Nataraj, $NiCo_2O_4$ functionalized with rGO catalyst as an active layer for ammonia sensing, Ionics 26 (2020) 5233–5240, https://doi.org/10.1007/s11581-020-03598-2.
[93] G. Marimuthu, G. Palanisamy, T. Pazhanivel, G. Bharathi, M.M. Cristopher, K. Jeyadheepan, Nanorod like $NiCo_2O_4$ nanostructure for high sensitive and selective ammonia gas sensor, J. Mater. Sci. Mater. Electron. 31 (2019) 1951–1959, https://doi.org/10.1007/s10854-019-02714-x.
[94] L. Du, X. Song, X. Liang, Y. Liu, M. Zhang, Formation of $NiCo_2O_4$ hierarchical tubular nanostructures for enhanced xylene sensing properties, Appl. Surf. Sci. 526 (2020) 146706, https://doi.org/10.1016/j.apsusc.2020.146706.
[95] Q. Wang, J. Bai, B. Huang, Q. Hu, X. Cheng, J. Li, E. Xie, Y. Wang, X. Pan, Design of $NiCo_2O_4$@$SnO_2$ heterostructure nanofiber and their low temperature ethanol sensing properties, J. Alloys Compd. 791 (2019) 1025–1032, https://doi.org/10.1016/j.jallcom.2019.03.364.
[96] V. Kumar, C.R. Mariappan, Characterization of mesoporous Zn doped $NiCo_2O_4$ rods produced by hydrothermal method for $NO_x$ gas sensing application, J. Alloys Compd. 773 (2019) 158–167, https://doi.org/10.1016/j.jallcom.2018.09.264.
[97] K.T. Alali, Z. Lu, H. Zhang, J. Liu, Q. Liu, R. Li, K. Aljebawi, J. Wang, P–p heterojunction $CuO/CuCo_2O_4$ nanotubes synthesized via electrospinning technology for detecting n-propanol gas at room temperature, Inorg. Chem. Front. 4 (2017) 1219–1230, https://doi.org/10.1039/c7qi00192d.
[98] B. Zhang, Y. Li, N. Luo, X. Xu, G. Sun, Y. Wang, J. Cao, $TiO_2/ZnCo_2O_4$ porous nanorods: synthesis and temperature-dependent dual selectivity for sensing HCHO and TEA, Sens. Actuators, B 321 (2020) 128461, https://doi.org/10.1016/j.snb.2020.128461.
[99] N. Luo, G. Sun, B. Zhang, Y. Li, H. Jin, L. Lin, H. Bala, J. Cao, Z. Zhang, Y. Wang, Improved TEA sensing performance of $ZnCo_2O_4$ by structure evolution from porous nanorod to single-layer nanochain, Sens. Actuators, B 277 (2018) 544–554, https://doi.org/10.1016/j.snb.2018.09.061.
[100] T. Xu, M. Zhang, F. Zhao, J. Zhao, W. Cong, C. Xie, Z. Yang, G. Wang, J. Li, Highly sensitive detection of $H_2S$ gas at low temperature based on $ZnCo_2O_4$microtube sensors, J. Hazard Mater. 440 (2022) 129753, https://doi.org/10.1016/j.jhazmat.2022.129753.
[101] K.T. Alali, J. Liu, Q. Liu, R. Li, H. Zhang, K. Aljebawi, P. Liu, J. Wang, Enhanced acetone gas sensing response of $ZnO/ZnCo_2O_4$ nanotubes synthesized by single capillary electrospinning technology, Sens. Actuators, B 252 (2017) 511–522, https://doi.org/10.1016/j.snb.2017.06.034.
[102] K.T. Alali, J. Liu, Q. Liu, R. Li, Z. Li, P. Liu, K. Aljebawi, J. Wang, Tube in tube $ZnO/ZnCo_2O_4$ nanostructure synthesized by facile single capillary electrospinning with enhanced ethanol gas-sensing properties, RSC Adv. 7 (2017) 11428–11438, https://doi.org/10.1039/c6ra28585f.
[103] K.B. Gawande, S.B. Gawande, S.R. Thakare, V.R. Mate, S.R. Kadam, B.B. Kale, M. V. Kulkarni, Effect of zinc : cobalt composition in $ZnCo_2O_4$ spinels for highly selective liquefied petroleum gas sensing at low and high temperatures, RSC Adv. 5 (2015) 40429–40436, https://doi.org/10.1039/c5ra03960f.

[104] S. Rathinavel, S. Vadivel, G. Balaji, Development of ethanol and acetone gas sensing performance of $MgCo_2O_4$ nanosensors by clad modified fiber optical method, Opt. Fiber Technol. 48 (2019) 218–224, https://doi.org/10.1016/j.yofte.2019.01.016.

[105] K. Xu, Y. Yang, T. Yu, C. Yuan, $WO_3$ nanofibers anchored by porous $NiCo_2O_4$ nanosheets for xylene detection, Ceram. Int. 44 (2018) 21717–21724, https://doi.org/10.1016/j.ceramint.2018.08.261.

[106] Y. Liang, W. Liu, W. Hu, Q. Zhou, K. He, K. Xu, Y. Yang, T. Yu, C. Yuan, Synthesis and gas-sensing properties of ZnO@$NiCo_2O_4$ core@shell nanofibers, Mater. Res. Bull. 114 (2019) 1–9, https://doi.org/10.1016/j.materresbull.2019.01.020.

[107] G. Marimuthu, B.-S. Nguyen, V.-T. Pham, V.-H. Nguyen, V.-M. Tran, K. Sivashanmugan, T. Pazhanivel, Novel $NiCo_2O_4$/MWCNTs nanocomposite with flake-like architecture as room temperature capacitive-type $NH_3$ gas sensor, Mater. Lett. 283 (2021) 128814, https://doi.org/10.1016/j.matlet.2020.128814.

[108] A. Sharma, P. Bhojane, A.K. Rana, Y. Kumar, P.M. Shirage, Mesoporous nickel cobalt hydroxide/oxide as an excellent room temperature ammonia sensor, Scripta Mater. 128 (2017) 65–68, https://doi.org/10.1016/j.scriptamat.2016.10.003.

[109] Y. Zhao, X. Yuan, Y. Sun, Q. Wang, X.-Y. Xia, B. Tang, Facile synthesis of tortoise shell-like porous $NiCo_2O_4$ nanoplate with promising triethylamine gas sensing properties, Sens. Actuators, B 323 (2020) 128663, https://doi.org/10.1016/j.snb.2020.128663.

[110] K. Xu, W. Wei, Y. Sun, W. Lu, T. Yu, Y. Yang, C. Yuan, Design of $NiCo_2O_4$ porous nanosheets/α-$MoO_3$ nanorods heterostructures for ppb-level ethanol detection, Powder Technol. 345 (2019) 633–642, https://doi.org/10.1016/j.powtec.2019.01.051.

[111] H.H. Zhang, N. Ullah, M. Abbas, S. Naeem, M.N. Ahmad, S. Hussain, N. Akhtar, A. Ahmad, M.S. Javed, O. Riaz, $NiCo_2O_4$ nanosheets for high performances formaldehyde gas sensing performances, J. Nanoelectron. Optoelectron. 16 (2021) 288–292, https://doi.org/10.1166/jno.2021.2950.

[112] H.N. Zhang, Y.J. Chen, rGO loaded porous $NiCo_2O_4$ nanoplates as alcohol gas sensors, Nanosci. Nano.Tech. Let. 9 (2017) 374–379, https://doi.org/10.1166/nnl.2017.2341.

[113] Z. Zhao, Z. Deng, R. Zhang, A. Klamchuen, Y. He, M. Horprathum, J. Chang, L. Mi, M. Li, S. Wang, X. Fang, G. Meng, Sensitive and selective ozone sensor based on $CuCo_2O_4$ synthesized by a facile solution combustion method, Sens. Actuators, B 375 (2023) 132912, https://doi.org/10.1016/j.snb.2022.132912.

[114] S. Jain, A. Patrike, S.S. Badadhe, M. Bhardwaj, S. Ogale, Room-temperature ammonia gas sensing using mixed-valent $CuCo_2O_4$ nanoplatelets: performance enhancement through stoichiometry control, ACS Omega 3 (2018) 1977–1982, https://doi.org/10.1021/acsomega.7b01958.

[115] V. Mani, S. Selvaraj, N. Jeromiyas, S.T. Huang, H. Ikeda, Y. Hayakawa, S. Ponnusamy, C. Muthamizhchelvan, K.N. Salama, Growth of large-scale $MoS_2$ nanosheets on double layered $ZnCo_2O_4$ for real-time in situ $H_2S$ monitoring in live cells, J. Mater. Chem. B 8 (2020) 7453–7465, https://doi.org/10.1039/d0tb01162b.

[116] X. Gao, C. Li, C. Zhu, Q. Ouyang, X. Zhang, Y. Chen, Synthesis and low-temperature sensing property of the porous $ZnCo_2O_4$ nanosheets, J. Mater. Sci. Mater. Electron. 30 (2019) 5357–5365, https://doi.org/10.1007/s10854-019-00789-0.

[117] Z. Yin, Z. Sun, J. Wu, R. Liu, S. Zhang, Y. Qian, Y. Min, Facile synthesis of hexagonal single-crystalline $ZnCo_2O_4$ nanosheet arrays assembled by mesoporous nanosheets as electrodes for high-performance electrochemical capacitors and gas sensors, Appl. Surf. Sci. 457 (2018) 1103–1109, https://doi.org/10.1016/j.apsusc.2018.06.297.

[118] J. Tan, S. Hussain, C. Ge, M. Wang, S. Shah, G. Liu, G. Qiao, ZIF-67 MOF-derived unique double-shelled $Co_3O_4$/$NiCo_2O_4$ nanocages for superior Gas-sensing performances, Sens. Actuators, B 303 (2020) 127251, https://doi.org/10.1016/j.snb.2019.127251.

[119] D. Wang, Q. Mi, H. Zhang, G. Li, D. Zhang, Sensitive xylene gas sensor based on NiO-$NiCo_2O_4$ hierarchical spherical structure constructed with nanorods, IEEE Sensor. J. 22 (2022) 10346–10352, https://doi.org/10.1109/jsen.2022.3168803.

[120] B. Zhang, F. Qu, X. Zhou, S. Zhang, T. Thomas, M. Yang, Porous coral-like $NiCo_2O_4$ nanospheres with promising xylene gas sensing properties, Sens. Actuators, B 261 (2018) 203–209, https://doi.org/10.1016/j.snb.2018.01.125.

[121] T. Zhou, X. Liu, R. Zhang, Y. Wang, T. Zhang, NiO/$NiCo_{(2)}O_{(4)}$ truncated nanocages with PdO catalyst functionalization as sensing layers for acetone detection, ACS Appl. Mater. Interfaces 10 (2018) 37242–37250, https://doi.org/10.1021/acsami.8b12981.

[122] F. Qu, H. Jiang, M. Yang, MOF-derived $Co_3O_4$/$NiCo_2O_4$ double-shelled nanocages with excellent gas sensing properties, Mater. Lett. 190 (2017) 75–78, https://doi.org/10.1016/j.matlet.2016.12.139.

[123] Y. Hu, T. Li, J. Zhang, J. Guo, W. Wang, D. Zhang, High-sensitive $NO_2$ sensor based on p-$NiCo_2O_4$/n-$WO_3$ heterojunctions, Sens. Actuators, B 352 (2022) 130912, https://doi.org/10.1016/j.snb.2021.130912.

[124] C. Yang, Y. Xu, L. Zheng, Y. Zhao, W. Zheng, X. Liu, J. Zhang, Hierarchical $NiCo_2O_4$ microspheres assembled by nanorods with p-type response for detection of triethylamine, Chin. Chem. Lett. 31 (2020) 2077–2082, https://doi.org/10.1016/j.cclet.2020.01.011.

[125] F. Dang, Y. Wang, J. Gao, L. Xu, P. Cheng, L. Lv, B. Zhang, X. Li, C. Wang, Hierarchical flower-like $NiCo_2O_4$ applied in n-butanol detection at low temperature, Sens. Actuators, B 320 (2020) 128577, https://doi.org/10.1016/j.snb.2020.128577.

[126] Y. Zheng, L. Wang, H. Tian, L. Qiao, Y. Zeng, C. Liu, Bimetal carbonaceous templates for multi-shelled $NiCo_2O_4$ hollow sphere with enhanced xylene detection, Sens. Actuators, B 339 (2021) 129862, https://doi.org/10.1016/j.snb.2021.129862.

[127] D. Zhang, Y. Yang, Z. Xu, D. Wang, C. Du, An eco-friendly gelatin based triboelectric nanogenerator for a self-powered PANI nanorod/$NiCo_2O_4$ nanosphere ammonia gas sensor, J. Mater. Chem. A 10 (2022) 10935–10949, https://doi.org/10.1039/d2ta01788a.

[128] L. Tian, Q. Liu, J.-l. Wu, Y.-t. Yi, Template-free hydrothermal synthesis and gas-sensitivity of hollow-structured $Cu_{0.3}Co_{2.7}O_4$ microspheres, J. Cent. South. Univ. 28 (2021) 1946–1954, https://doi.org/10.1007/s11771-021-4743-5.

[129] X. Ma, Z. Ying, F. Wen, L. Li, X. Zheng, P. Zheng, G. Wang, Gas-sensitive properties of ZnO/$ZnCo_2O_4$ made from sodium citrate against formaldehyde, J. Electron. Mater. 51 (2022) 7009–7019, https://doi.org/10.1007/s11664-022-09930-y.

[130] M. Li, W. Xu, R. Jiang, M. Du, L. Zhang, S. Yang, S. Wang, J. Cao, Constructing $ZnCo_2O_4$ hierarchical porous architectures for enhanced xylene gas detection, Colloids Surf., A 649 (2022) 129522, https://doi.org/10.1016/j.colsurfa.2022.129522.

[131] F. Qu, T. Thomas, B. Zhang, X. Zhou, S. Zhang, S. Ruan, M. Yang, Self-sacrificing templated formation of $Co_3O_4$/$ZnCo_2O_4$ composite hollow nanostructures for highly sensitive detecting acetone vapor, Sens. Actuators, B 273 (2018) 1202–1210, https://doi.org/10.1016/j.snb.2018.07.005.

[132] Q. Qin, Y. Li, W. Bu, L. Meng, X. Chuai, Z. Zhou, C. Hu, Self-template-derived $ZnCo_2O_4$ porous microspheres decorated by Ag nanoparticles and their selective detection of formaldehyde, Inorg. Chem. Front. 8 (2021) 811–820, https://doi.org/10.1039/d0qi01144d.

[133] X. Li, Y. Zhang, Y. Cheng, X. Chen, W. Tan, MOF-derived porous hierarchical $ZnCo_2O_4$ microflowers for enhanced performance gas sensor, Ceram. Int. 47 (2021) 9214–9224, https://doi.org/10.1016/j.ceramint.2020.12.047.

[134] Y. Xiong, Z. Zhu, D. Ding, W. Lu, Q. Xue, Multi-shelled $ZnCo_2O_4$ yolk-shell spheres for high-performance acetone gas sensor, Appl. Surf. Sci. 443 (2018) 114–121, https://doi.org/10.1016/j.apsusc.2018.02.189.

[135] D. Zhang, Y. Jin, H. Chen, Y. Luo, Y. Zhang, Carbon microsphere-templated synthesis of $ZnCo_2O_4$ hollow spheres functionalized with Ag nanoparticles for sub-ppm-level acetone gas detection, Ceram. Int. 46 (2020) 15176–15182, https://doi.org/10.1016/j.ceramint.2020.03.054.

[136] N. Joshi, L.F. da Silva, H.S. Jadhav, F.M. Shimizu, P.H. Suman, J.-C. M'Peko, M. O. Orlandi, J.G. Seo, V.R. Mastelaro, O.N. Oliveira Jr., Yolk-shelled $ZnCo_2O_4$ microspheres: surface properties and gas sensing application, Sens. Actuators, B 257 (2018) 906–915, https://doi.org/10.1016/j.snb.2017.11.041.

[137] Y. Li, N. Luo, G. Sun, B. Zhang, H. Jin, L. Lin, H. Bala, J. Cao, Z. Zhang, Y. Wang, Synthesis of porous nanosheets-assembled ZnO/$ZnCo_2O_4$ hierarchical structure for TEA detection, Sens. Actuators, B 287 (2019) 199–208, https://doi.org/10.1016/j.snb.2019.02.055.

[138] W.-T. Koo, S.-J. Choi, J.-S. Jang, I.-D. Kim, Metal-organic framework templated synthesis of ultrasmall catalyst loaded ZnO/$ZnCo_2O_4$ hollow spheres for enhanced gas sensing properties, Sci. Rep. 7 (2017) 45074, https://doi.org/10.1038/srep45074.

[139] N. Zhang, Y. Lu, Y. Fan, J. Zhou, X. Li, S. Adimi, C. Liu, S. Ruan, Metal-organic framework-derived ZnO/$ZnCo_2O_4$ microspheres modi fied by catalytic PdO nanoparticles for sub-ppm-level formaldehyde detection, Sens. Actuators, B 315 (2020) 128118, https://doi.org/10.1016/j.snb.2020.128118.

[140] G. Yuan, H. Zhang, Y. Cheng, Y. Zhong, Q. Zhuo, X. Sun, Hollow polyhedral $ZnCo_2O_4$ superstructure as an ethanol gas sensor and sensing mechanism study using near ambient pressure XPS, J. Mater. Chem. C 9 (2021) 14278–14285, https://doi.org/10.1039/d1tc03450b.

[141] Y.V. Kaneti, N.L.W. Septiani, I. Saptiama, X. Jiang, B. Yuliarto, M.J.A. Shiddiky, N. Fukumitsu, Y.-M. Kang, D. Golberg, Y. Yamauchi, Self-sacrificial templated synthesis of a three-dimensional hierarchical macroporous honeycomb-like ZnO/$ZnCo_2O_4$ hybrid for carbon monoxide sensing, J. Mater. Chem. A 7 (2019) 3415–3425, https://doi.org/10.1039/c8ta11380g.

[142] T. Zhou, S. Cao, R. Zhang, T. Fei, T. Zhang, $Zn_xCo_{3-x}O_4$ bimetallic oxides derived from metal-organic frameworks for enhanced acetone sensing performances, Inorg. Chem. Front. 6 (2019) 3177–3183, https://doi.org/10.1039/c9qi01057b.

[143] T. Zhou, N. Sui, R. Zhang, T. Zhang, Cabbage-shaped zinc-cobalt oxide ($ZnCo_2O_4$) sensing materials: effects of zinc ion substitution and enhanced formaldehyde sensing properties, J. Colloid Interface Sci. 537 (2019) 520–527, https://doi.org/10.1016/j.jcis.2018.11.030.

[144] J. Liu, L. Zhang, B. Cheng, J. Fan, J. Yu, A high-response formaldehyde sensor based on fibrous Ag-ZnO/$In_2O_3$ with multi-level heterojunctions, J. Hazard Mater. 413 (2021) 125352, https://doi.org/10.1016/j.jhazmat.2021.125352.

[145] L.X. Ou, M.Y. Liu, L.Y. Zhu, D.W. Zhang, H.L. Lu, Recent progress on flexible room-temperature gas sensors based on metal oxide semiconductor, Nano-Micro Lett. 14 (2022) 206, https://doi.org/10.1007/s40820-022-00956-9.

[146] F. Hossein-Babaei, S. Rahbarpour, Separate assessment of chemoresistivity and Schottky-type gas sensitivity in M–metal oxide–M′ structures, Sens. Actuators, B 160 (2011) 174–180, https://doi.org/10.1016/j.snb.2011.07.029.

[147] W. Pi, X. Chen, M. Humayun, Y. Yuan, W. Dong, G. Zhang, B. Chen, Q. Fu, Z. Lu, H. Li, Z. Tang, W. Luo, Highly sensitive chemiresistive $H_2S$ detection at subzero temperature over the Sb-doped $SnO_2$@g-$C_3N_4$ heterojunctions under UV illumination, ACS Appl. Mater. Interfaces 15 (2023) 14979–14989, https://doi.org/10.1021/acsami.3c00213.

[148] Y. Yang, S.J. Yu, J.Y. Guo, D.Z. Zhang, UV-enhanced highly sensitive ammonia sensing properties based on 2DPI/$In_2O_3$ heterostructure at room temperature, J. Alloys Compd. 920 (2022) 165878, https://doi.org/10.1016/j.jallcom.2022.165878.

[149] M. Manjula, B. Karthikeyan, D. Sastikumar, Sensing characteristics of nanocrystalline bismuth oxide clad-modified fiber optic gas sensor, Opt Laser. Eng. 95 (2017) 78–82, https://doi.org/10.1016/j.optlaseng.2017.04.003.

[150] C. Zhang, Y. Huan, Y. Li, Y. Luo, M. Debliquy, Low concentration isopropanol gas sensing properties of Ag nanoparticles decorated $In_2O_3$ hollow spheres, J. Adv. Ceram. 11 (2022) 379–391, https://doi.org/10.1007/s40145-021-0530-x.

[151] R. Shaik, R.K. Kampara, A. Kumar, C.S. Sharma, M. Kumar, Metal oxide nanofibers based chemiresistive $H_2S$ gas sensors, Coord. Chem. Rev. 471 (2022) 214752, https://doi.org/10.1016/j.ccr.2022.214752.

[152] B. Zhang, J.-Y. Sun, P.-X. Gao, Low-concentration $NO_x$ gas analysis using single bimodular ZnO nanorod sensor, ACS Sens. 6 (2021) 2979–2987, https://doi.org/10.1021/acssensors.1c00834.

[153] J. Xu, C. Zhang, Oxygen vacancy engineering on cerium oxide nanowires for room-temperature linalool detection in rice aging, J. Adv. Ceram. 11 (2022) 1559–1570, https://doi.org/10.1007/s40145-022-0629-8.

[154] S. Acharyya, S. Nag, S. Kimbahune, A. Ghose, A. Pal, P.K. Guha, Selective discrimination of VOCs applying gas sensing kinetic analysis over a metal oxide-based chemiresistive gas sensor, ACS Sens. 6 (2021) 2218–2224, https://doi.org/10.1021/acssensors.1c00115.

[155] Z. Zheng, K. Liu, Y. Zhou, M. Debliquy, C. Zhang, Ultrasensitive room-temperature geranyl acetone detection based on Fe@$WO_{3-x}$ nanoparticles in cooked rice flavor analysis, J. Adv. Ceram. (2023), https://doi.org/10.26599/JAC.2023.9220771.

[156] H. He, C. Zhao, J. Xu, K. Qu, Z. Jiang, Z. Gao, Y.Y. Song, Exploiting free-standing p-CuO/n-$TiO_2$ nanochannels as a flexible gas sensor with high sensitivity for $H_2S$ at room temperature, ACS Sens. 6 (2021) 3387–3397, https://doi.org/10.1021/acssensors.1c01256.

[157] W. Li, K. Nagashima, T. Hosomi, C. Wang, Y. Hanai, A. Nakao, A. Shunori, J. Liu, G. Zhang, T. Takahashi, W. Tanaka, M. Kanai, T. Yanagida, Mechanistic approach for long-term stability of a polyethylene glycol–carbon black nanocomposite sensor, ACS Sens. 7 (2022) 151–158, https://doi.org/10.1021/acssensors.1c01875.

[158] H. Zhu, Q. Li, Y. Ren, Q. Gao, J. Chen, N. Wang, J. Deng, X. Xing, A new insight into cross-sensitivity to humidity of $SnO_2$ sensor, Small 14 (2018) 1703974, https://doi.org/10.1002/smll.201703974.

[159] H. Ji, H. Zhu, H. Wang, L. Kong, Z. Cheng, Z. Yuan, F. Meng, Gas detection strategy to suppress flow rate interference baesd on semiconductor sensor dynamic temperature modulation measurement, Sens. Actuators, B 393 (2023) 134232, https://doi.org/10.1016/j.snb.2023.134232.

[160] P.J. van der Put, Synthesis of inorganic materials, in: P.J. van der Put (Ed.), The Inorganic Chemistry of Materials: How to Make Things Out of Elements, Springer US, Boston, MA, 1998, pp. 273–317.

[161] B. Yang, N.V. Myung, T.-T. Tran, 1D metal oxide semiconductor materials for chemiresistive gas sensors: a review, Adv. Electron. Mater. 7 (2021) 2100271, https://doi.org/10.1002/aelm.202100271.

[162] S. Naz, S.K. Durrani, M. Mehmood, M. Nadeem, Hydrothermal synthesis, structural and impedance studies of nanocrystalline zinc chromite spinel oxide material, J. Saudi Chem. Soc. 20 (2016) 585–593, https://doi.org/10.1016/j.jscs.2014.12.007.

[163] M.J. Molaei, M. Younas, M. Rezakazemi, Van der Waals heterostructures in ultrathin 2D solar cells: state-of-the-art review, Mater. Sci. Eng., B 285 (2022) 115936, https://doi.org/10.1016/j.mseb.2022.115936.

[164] B. Choi, D. Shin, H.S. Lee, H. Song, Nanoparticle design and assembly for p-type metal oxide gas sensors, Nanoscale 14 (2022) 3387–3397, https://doi.org/10.1039/d1nr07561f.

[165] H.H. Liu, D.L. Chen, Z.Q. Wang, H.J. Jing, R. Zhang, Microwave-assisted molten-salt rapid synthesis of isotype triazine-/heptazine based g-$C_3N_4$ heterojunctions with highly enhanced photocatalytic hydrogen evolution performance, Appl. Catal. B Environ. 203 (2017) 300–313, https://doi.org/10.1016/j.apcatb.2016.10.014.

[166] R. Gangopadhyay, A. De, Conducting polymer nanocomposites: a brief overview, Chem. Mater. 12 (2000) 608–622, https://doi.org/10.1021/cm990537f.

[167] P.-G. Su, Y.-T. Peng, Fabrication of a room-temperature $H_2S$ gas sensor based on PPy/$WO_3$ nanocomposite films by in-situ photopolymerization, Sens. Actuators, B 193 (2014) 637–643, https://doi.org/10.1016/j.snb.2013.12.027.

[168] S.V. Bangale, Nanostructured ZncooThick film as an ethanol sensor, Int. J. Smart Sens. Int. 7 (2014) 178–195, https://doi.org/10.21307/ijssis-2017-651.

[169] K. Großmann, S. Wicker, U. Weimar, N. Barsan, Impact of Pt additives on the surface reactions between $SnO_2$, water vapour, CO and $H_2$; an operando investigation, Phys. Chem. Chem. Phys. 15 (2013) 19151–19158, https://doi.org/10.1039/C3CP52782D.

[170] S. Wicker, M. Guiltat, U. Weimar, A. Hémeryck, N. Barsan, Ambient humidity influence on CO detection with $SnO_2$ gas sensing materials. A combined DRIFTS/DFT investigation, J. Phys. Chem. C 121 (2017) 25064–25073, https://doi.org/10.1021/acs.jpcc.7b06253.

[171] D. Zappa, V. Galstyan, N. Kaur, H.M.M. Munasinghe Arachchige, O. Sisman, E. Comini, "Metal oxide -based heterostructures for gas sensors"- A review, Anal. Chim. Acta 1039 (2018) 1–23, https://doi.org/10.1016/j.aca.2018.09.020.

[172] T. Li, W. Yin, S. Gao, Y. Sun, P. Xu, S. Wu, H. Kong, G. Yang, G. Wei, The combination of two-dimensional nanomaterials with metal oxide nanoparticles for gas sensors: a review, Nanomaterials 12 (2022) 982, https://doi.org/10.3390/nano12060982.

[173] N. Sui, P. Zhang, T. Zhou, T. Zhang, Selective ppb-level ozone gas sensor based on hierarchical branch-like $In_2O_3$ nanostructure, Sens. Actuators, B 336 (2021) 129612, https://doi.org/10.1016/j.snb.2021.129612.

[174] G. Korotcenkov, I. Blinov, V. Brinzari, J.R. Stetter, Effect of air humidity on gas response of $SnO_2$ thin film ozone sensors, Sens. Actuators, B 122 (2007) 519–526, https://doi.org/10.1016/j.snb.2006.06.025.

[175] J.-H. Lee, Gas sensors using hierarchical and hollow oxide nanostructures: overview, Sens. Actuators, B 140 (2009) 319–336, https://doi.org/10.1016/j.snb.2009.04.026.

[176] H. Chun Zeng, Ostwald ripening: a synthetic approach for hollow nanomaterials, Curr. Nanosci. 3 (2007) 177–181, https://doi.org/10.2174/157341307780619279.

[177] L.F. Han, S.D. Wu, Z. Hu, M.Z. Chen, J.W. Ding, S.W. Wang, Y. Zhang, D.J. Guo, L. Zhang, S.K. Cao, S.L. Chou, Hierarchically porous $MoS_2$-carbon hollow rhomboids for superior performance of the anode of sodium-ion batteries, ACS Appl. Mater. Interfaces 12 (2020) 10402–10409, https://doi.org/10.1021/acsami.9b21365.

[178] M. Kosari, U. Anjum, S.B. Xi, A.M.H. Lim, A.M. Seayad, E.A.J. Raj, S.M. Kozlov, A. Borgna, H.C. Zeng, Revamping $SiO_2$ spheres by core-shell porosity endowment to construct a mazelike nanoreactor for enhanced catalysis in $CO_2$ hydrogenation to methanol, Adv. Funct. Mater. 31 (2021) 2102896, https://doi.org/10.1002/adfm.202102896.

[179] F. Li, T. Zhang, X. Gao, R. Wang, B. Li, Coaxial electrospinning heterojunction $SnO_2$/Au-doped $In_2O_3$ core-shell nanofibers for acetone gas sensor, Sens. Actuators, B 252 (2017) 822–830, https://doi.org/10.1016/j.snb.2017.06.077.

[180] J.M. Suh, W. Sohn, Y.S. Shim, J.S. Choi, Y.G. Song, T.L. Kim, J.M. Jeon, K. C. Kwon, K.S. Choi, C.Y. Kang, H.G. Byun, H.W. Jang, p-p heterojunction of nickel oxide-decorated cobalt oxide nanorods for enhanced sensitivity and selectivity toward volatile organic compounds, ACS Appl. Mater. Interfaces 10 (2018) 1050–1058, https://doi.org/10.1021/acsami.7b14545.

[181] Y.Y. Lu, W.W. Zhan, Y. He, Y.T. Wang, X.J. Kong, Q. Kuang, Z.X. Xie, L.S. Zheng, MOF-templated synthesis of porous $Co_3O_4$ concave nanocubes with high specific surface area and their gas sensing properties, ACS Appl. Mater. Interfaces 6 (2014) 4186–4195, https://doi.org/10.1021/am405858v.

[182] L. Chai, Z. Hu, X. Wang, Y. Xu, L. Zhang, T.-T. Li, Y. Hu, J. Qian, S. Huang, Stringing bimetallic metal–organic framework-derived cobalt phosphide composite for high-efficiency overall water splitting, Adv. Sci. 7 (2020) 1903195, https://doi.org/10.1002/advs.201903195.

[183] S. Zhang, W. Xia, Q. Yang, Y. Valentino Kaneti, X. Xu, S.M. Alshehri, T. Ahamad, M.S.A. Hossain, J. Na, J. Tang, Y. Yamauchi, Core-shell motif construction: highly graphitic nitrogen-doped porous carbon electrocatalysts using MOF-derived carbon@COF heterostructures as sacrificial templates, Chem. Eng. J. 396 (2020) 125154, https://doi.org/10.1016/j.cej.2020.125154.

[184] C. Kang, L. Ma, Y. Chen, L. Fu, Q. Hu, C. Zhou, Q. Liu, Metal-organic framework derived hollow rod-like NiCoMn ternary metal sulfide for high-performance asymmetric supercapacitors, Chem. Eng. J. 427 (2022) 131003, https://doi.org/10.1016/j.cej.2021.131003.

[185] S.L. Li, Q. Xu, Metal-organic frameworks as platforms for clean energy, Energy Environ. Sci. 6 (2013) 1656–1683, https://doi.org/10.1039/c3ee40507a.

[186] H. Ji, W. Zeng, Y. Li, Assembly of 2D nanosheets into flower-like $MoO_3$: new insight into the petal thickness affect on gas-sensing properties, Mater. Res. Bull. 118 (2019) 110476, https://doi.org/10.1016/j.materresbull.2019.05.001.

[187] E. Lee, Y.S. Yoon, D.-J. Kim, Two-dimensional transition metal dichalcogenides and metal oxide hybrids for gas sensing, ACS Sens. 3 (2018) 2045–2060, https://doi.org/10.1021/acssensors.8b01077.

[188] M. Wang, T. Hou, Z. Shen, X. Zhao, H. Ji, MOF-derived $Fe_2O_3$: phase control and effects of phase composition on gas sensing performance, Sens. Actuators, B 292 (2019) 171–179, https://doi.org/10.1016/j.snb.2019.04.124.

[189] X. Wang, Y. Wang, F. Tian, H. Liang, K. Wang, X. Zhao, Z. Lu, K. Jiang, L. Yang, X. Lou, From the surface reaction control to gas-diffusion control: the synthesis of hierarchical porous $SnO_2$ microspheres and their gas-sensing mechanism, J. Phys. Chem. C 119 (2015) 15963–15976, https://doi.org/10.1021/acs.jpcc.5b01397.

[190] C. Xu, J. Tamaki, N. Miura, N. Yamazoe, Grain size effects on gas sensitivity of porous $SnO_2$-based elements, Sens. Actuators, B 3 (1991) 147–155, https://doi.org/10.1016/0925-4005(91)80207-Z.

[191] Z. Song, S. Xu, J. Liu, Z. Hu, N. Gao, J. Zhang, F. Yi, G. Zhang, S. Jiang, H. Liu, Enhanced catalytic activity of $SnO_2$ quantum dot films employing atomic ligand-exchange strategy for fast response H2S gas sensors, Sens. Actuators, B 271 (2018) 147–156, https://doi.org/10.1016/j.snb.2018.05.122.

[192] F.-J. Meng, R.-F. Xin, S.-X. Li, Metal oxide heterostructures for improving gas sensing properties: a review, Materials 16 (2023) 263, https://doi.org/10.3390/ma16010263.

[193] S. Xue, S. Cao, Z. Huang, D. Yang, G. Zhang, Improving gas-sensing performance based on mos nanomaterials: a review, Materials 14 (2021) 4263, https://doi.org/10.3390/ma14154263.

[194] C.Y. Cheng, Q.H. Liang, M. Yan, Z.F. Liu, Q.Y. He, T. Wu, S.H. Luo, Y. Pan, C. H. Zhao, Y. Liu, Advances in preparation, mechanism and applications of graphene quantum dots/semiconductor composite photocatalysts: a review, J. Hazard Mater. 424 (2022) 127721, https://doi.org/10.1016/j.jhazmat.2021.127721.

[195] H.-J. Kim, J.-H. Lee, Highly sensitive and selective gas sensors using p-type oxide semiconductors: overview, Sens. Actuators, B 192 (2014) 607–627, https://doi.org/10.1016/j.snb.2013.11.005.

[196] N. Barsan, U. Weimar, Conduction model of metal oxide gas sensors, J. Electroceram. 7 (2001) 143–167, https://doi.org/10.1023/A:1014405811371.

[197] T. Zhao, P. Qiu, Y. Fan, J. Yang, W. Jiang, L. Wang, Y. Deng, W. Luo, Hierarchical branched mesoporous $TiO_2$-$SnO_2$ nanocomposites with well-defined n-n heterojunctions for highly efficient ethanol sensing, Adv. Sci. 6 (2019) 1902008, https://doi.org/10.1002/advs.201902008.

[198] Y. Ou, G. Zhu, P. Liu, Y. Jia, L. Zhu, J. Nie, S. Zhang, W. Zhang, J. Gao, H. Lu, Y. Huang, X. Shi, M. Hojamberdiev, Anchoring platinum clusters onto oxygen vacancy-modified $In_2O_3$ for ultraefficient, low-temperature, highly sensitive, and stable detection of formaldehyde, ACS Sens. 7 (2022) 1201–1212, https://doi.org/10.1021/acssensors.2c00334.

[199] J. Pablo Moran-Lazaro, F. Lopez-Urias, E. Munoz-Sandoval, O. Blanco-Alonso, M. Sanchez-Tizapa, A. Carreon-Alvarez, H. Guillen-Bonilla, M. de la Luz Olvera-Amador, A. Guillen-Bonilla, V. Maria Rodriguez-Betancourtt, Synthesis, characterization, and sensor applications of spinel $ZnCo_2O_4$ nanoparticles, Sensors 16 (2016) 2162, https://doi.org/10.3390/s16122162.

[200] X. Zhang, X. Li, R. Li, Y. Lu, S. Song, Y. Wang, Highly active core–shell carbon/$NiCo_2O_4$ double microtubes for efficient oxygen evolution reaction: ultralow overpotential and superior cycling stability, Small 15 (2019) 1903297, https://doi.org/10.1002/smll.201903297.

[201] W. Bekhti, M. Ghamnia, L. Guerbous, Effect of some amines, dodecylamine (DDA) and hexadecyldimethylamine (DMHA), on the formation of ZnO nanorods synthesized by hydrothermal route, Philos. Mag. A 94 (2014) 2886–2899, https://doi.org/10.1080/14786435.2014.937785.

[202] J. Yang, E. Sargent, S. Kelley, J.Y. Ying, A general phase-transfer protocol for metal ions and its application in nanocrystal synthesis, Nat. Mater. 8 (2009) 683–689, https://doi.org/10.1038/nmat2490.

[203] L.-X. Ou, M.-Y. Liu, L.-Y. Zhu, D.W. Zhang, H.-L. Lu, Recent progress on flexible room-temperature gas sensors based on metal oxide semiconductor, Nano-Micro Lett. 14 (2022) 206, https://doi.org/10.1007/s40820-022-00956-9.

[204] Y. Xia, B. Cheng, J. Fan, J. Yu, G. Liu, Unraveling photoexcited charge transfer pathway and process of CdS/graphene nanoribbon composites toward visible-light photocatalytic hydrogen evolution, Small 15 (2019) 1902459, https://doi.org/10.1002/smll.201902459.

[205] A. Meng, L. Zhang, B. Cheng, J. Yu, Dual cocatalysts in $TiO_2$ photocatalysis, Adv. Mater. 31 (2019) 1807660, https://doi.org/10.1002/adma.201807660.

[206] K.G. Krishna, G. Umadevi, S. Parne, N. Pothukanuri, Zinc oxide based gas sensors and their derivatives: a critical review, J. Mater. Chem. C 11 (2023) 3906–3925, https://doi.org/10.1039/D2TC04690C.

[207] F. Qu, H. Jiang, M. Yang, Designed formation through a metal organic framework route of $ZnO/ZnCo_2O_4$ hollow core-shell nanocages with enhanced gas sensing properties, Nanoscale 8 (2016) 16349–16356, https://doi.org/10.1039/c6nr05187a.

[208] X. Zhou, W. Feng, C. Wang, X. Hu, X. Li, P. Sun, K. Shimanoe, N. Yamazoe, G. Lu, Porous $ZnO/ZnCo_2O_4$ hollow spheres: synthesis, characterization, and applications in gas sensing, J. Mater. Chem. A 2 (2014) 17683–17690, https://doi.org/10.1039/c4ta04386c.

[209] A.K. Geim, K.S. Novoselov, The rise of graphene, Nat. Mater. 6 (2007) 183–191, https://doi.org/10.1038/nmat1849.

[210] M.A. Basyooni, S.E. Zaki, S. Ertugrul, M. Yilmaz, Y.R. Eker, Fast response of $CO_2$ room temperature gas sensor based on Mixed-Valence Phases in Molybdenum and Tungsten Oxide nanostructured thin films, Ceram. Int. 46 (2020) 9839–9853, https://doi.org/10.1016/j.ceramint.2019.12.259.